UNIVERSITY OF CYPRUS

Department of Electrical and Computer Engineering

A Fluoroscopic Cancer Screening Capsule For The Small Intestine

Panayiota Demosthenous

A Dissertation

Submitted in Partial Fulfillment of the

Requirements for the Degree of

Doctor of Philosophy

at the University of Cyprus

December, 2014

APPROVAL PAGE

Panayiota Demosthenous

A Fluoroscopic Cancer Screening Capsule For The Small Intestine

The present Doctorate Dissertation was submitted in partial fulfillment of the requirements for the Degree of Doctor of Philosophy in the Department of Electrical and Computer Engineering, and was approved on 8 December, 2014 by the members of the Examination Committee.

Committee Chair ______________________
Dr. Constantinos Pitris

Research Supervisor ______________________
Dr. J. Georgiou

Committee Member ______________________
Prof. A. Othonos

Committee Member ______________________
Dr. T. Theocharides

Committee Member ______________________
Dr. Emmanuel M. Drakakis

To my little boy Angelos !

Abstract

Early detection of cancer is crucial to the success of treatment and the survival of patients. One of the organs that present a diagnostic challenge in regards to early cancer detection is the small intestine due to its inaccessibility and convoluted structure. Even though swallowable imaging capsules have been developed to address this issue, they are unsuitable for the detection of early-stage or flat cancers.

The goal of the presented research is to develop a screening capsule, designed specifically for fluorescence detection in the gastrointestinal tract. By using this capsule in conjunction with novel molecular contrast agents, which are selectively probed to cancerous cells, it is expected that cancers of the small intestine could be detected at a very early stage, with high sensitivity and at low cost.

The development of such a screening capsule is extremely challenging, both in terms of optical design and electronics design, in addition to its multidisciplinary nature. On the one hand the emitted light intensity of fluorescence is several orders of magnitude smaller than the excitation intensity, whilst on the other hand the power budget for the electronics is extremely low. The information storage requirements and the limited size of the capsule are additional factors that complicate the design further. This thesis presents an innovative, mixed-signal electronic capsule, which overcomes these challenges.

Περίληψη

Η πρόωρη ανίχνευση καρκίνου είναι σημαντική για την επιτυχή θεραπεία και επιβίωση του θεράποντα. Ένα όργανο του πεπτικού συστήματος που αποτελεί πρόκληση ως προς την ανίχνευση πρώιμων καρκινωμάτων, είναι το λεπτό έντερο, που λόγο της περιπεπλεγμένης δομής του είναι δύσκολα προσβάσιμο από διαγνωστικά εργαλεία. Το πρόβλημα της προσβασιμότητας του, έρχονται να επιλύσουν οι κάψουλες ενδοσκόπησης, οι οποίες όμως δεν είναι ιδανικές στο να ανιχνέυουν καρκίνο στα πρώτα στάδια της εξέλιξης του.

Ο στόχος της παρούσας έρευνας είναι κατασκευή μιας διαγνωστικής κάψουλας, που είναι ειδικά σχεδιασμένη για να ανιχνέυει φθορισμό στο γαστρεντερικό σύστημα. Η κάψουλα αυτή σε συνδυασμό με μια χρωστική ουσία η οποία επιλεκτικά προσκολλάται στα καρκινικά κύτταρα και τα καθιστά ανιχνέυσιμα μέσω του φθορισμού της, αναμένεται ότι θα χρησιμοποιηθεί για την αποδοτική ανίχνευση πρώιμων καρκινωμάτων στο λεπτό έντερο.

Η δημιουργία μιας τέτοιας κάψουλας αποτελεί ιδιαίτερη πρόκληση ως προς τη σχεδίαση των ηλεκτρονικών της, αφού πρέπει να είναι μικρή σε μέγεθος και να καταναλώνει ελάχιστη ισχύ. Επιπρόσθετα, η πολυπλοκότητα μιας τέτοιας έρευνας αποδίδεται στο γεγονός ότι· τα χαμηλά επίπεδα έντασης του φθορισμού, δύσκολα διαχωρίζονται από την υψηλή ένταση της ακτινοβολίας διέγερσης, αφού τα δύο φάσματα βρίσκονται συγκριτικά κοντά.

Acknowledgments

I would like to express my special appreciation and thanks to my advisor, Dr. Julius Georgiou, who believed in me in the first place, and invited me to join his research team and follow the adventurous world of research. I would like to thank him for the encouragement and for allowing me to grow as a research scientist. I would also like to thank him for his enthusiasm, motivation and for transferring his immense knowledge to me through my research.

I would also like to thank Prof. C. Pitris for the helpful discussions on issues related to optics and fluorescence and for pointing out the need for such a capsule. I would like also to thank Dr. Andreani Odysseos and her PhD student Louiza, who were willing to provide me with cryopreserved human tissues samples impregnated with ICG that were necessary for several of my experiments.

Special thanks go to my colleagues for their help at various points of my research. Your skills, experience and knowledge on different fields were very useful. In particular, I would like to thank my office-mate and friend Nicoletta Nicolaou, for her support and “patience”. Your expertise in Matlab saved me a lot of time during my PhD and your energetic and amusing personality added several relaxing hours between all those stressful times.

Furthermore, I would like to thank separately the Cyprus College and the Department of Chemistry, for giving access to equipment that was not available at the Electrical Engineer Department of UCY (a spectrometer and a precision scale). I would also like to thank the administrators Skevi C. and Despina, of KIOS Research Center, in addition to Vaso and Skevi I., of the ECE department, for their professionalism and helpfulness.

Finally, I would like to thank my family, my father Michalis, my mother Christalla and my sisters Elisavet, Zoe and Marianna. Your love and faith in me was a constant inspiration and acted as my main driving force.

Last, but not least, I would like to thank my husband Alexandros. This journey would not has been finished without your love and encouragement. I thank you for supporting me all this time with your advice and your care.

Publications

Peer Reviewed Journal

1. P. Demosthenous, C. Pitris and J. Georgiou, " Infrared fluorescence-based Cancer Screening Capsule for the Small Intestine ", *under review* for IEEE Transactions on Biomedical Circuits and Systems.

Peer Reviewed Conference Proceedings

1. P. Demosthenous and J. Georgiou, " A Fluorescence Based Endoscopic Microcancer Detection Capsule ", *under review* for the International Symposium on Circuits and Systems, 24-27 May 2015, Lisbon, Portugal.

2. P. Demosthenous and J. Georgiou, " Towards a Fluoroscopic Cancer Screening Capsule for the Small Intestine ", IEEE 2014 Engineering in Medicine and Biology Society Conference, 26-30 August 2014, Chicago, IL, USA.

3. P. Demosthenous and J. Georgiou, " Acceleration-dependent Sampling for Ingestible Endoscopic Imaging Capsule ", IEEE 2012 Biomedical Circuits and System Conference, pp. 1-4, 28-30 November, Hsinchu, Taiwan.

4. P. Demosthenous, N. Nicolaou and J. Georgiou, " A Hardware-efficient Low-pass Filter Design for Biomedical Applications ", IEEE 2010 Biomedical Circuits and System Conference, pp. 130-133, 3-5 November, Paphos, Cyprus.

Contents

List of Figures

List of Tables

Chapter 1

Introduction

1.1 Motivation

Carcinomas of the small intestine are considered to be relatively rare malignancies in comparison to other malignancies of the gastrointestinal (GI) tract. However, the prognosis of primary intestine-cancer patients remains poor with 5-year survival rates ranging from 20% to 30% [14]. The non-specific symptoms and infrequent occurrence of carcinomas in the small intestine lead to a delay in diagnosis. Screening procedures can provide early prognosis with the detection of cancer at an early stage, where treatment is more effective, resulting in higher probability of the patient survival [2]. The small intestine presents a diagnostic challenge with regards to screening procedure due to its inaccessibility and convoluted structure. A diagnostic method that is frequently used for detection of cancer in GI tract is classical endoscopy, which is quite invasive and expensive for screening purposes; however the nature of the endoscope itself limits its applicability for screening at the upper and lower ends of the small intestine only. Swallowable imaging capsules provide a non-invasive diagnostic method and have been developed to address the inaccessibility issue to other parts of the small intestine [64]. However, the number of images and image quality delivered by these capsules are not optimal for screening purposes and for the detection of very-early or flat cancers. On the other hand, infrared fluorescence imaging (IRFI) of molecular contrast agents, targeting specific receptors of the disease, has proved to be very useful for the detection of early gastric cancer, with greater accuracy and sensitivity than white light imaging technology. However, this technique has only been applied with the use of an IRF endoscope [73].

For the above reasons, an effective non-invasive IR fluoroscopic screening instrument is needed for micro cancer detection in the small intestine. The successful development of such an instrument will provide a number of benefits for patients. It will provide a non-invasive and accurate screening method for primary cancer detection with more effective treatment and early removal of the abnormal tissue, thus preventing metastasis to other vital organs. Consequently, such an instrument will have a significant impact on improving public health, as it largely increases the survival rate and improves patient quality of life.

1.2 Research Objectives

This research focuses on developing a novel screening capsule prototype which, unlike existing imaging capsules, will have the ability to detect early-stage cancer in the small intestine. It will do so by measuring infrared (IR) fluorescence intensity, delivered by a fluorescent molecular probe that is selectively uptaken by cancerous cells. Even though the small intestine has remarkably low incidence of primary carcinomas or other malignancies (2% of all GI malignancies [14]), it remains the main site for metastatic tumours in the gastrointestinal tract, since it is located between two organs with high cancer incidence, the stomach and colon. Studies have shown that only the 30% of the patients, with preoperative diagnosis of cancer in the small intestine, have five-year survival rate while the median survival was 3.3 years [14]. As such, it is expected that this new cancer-screening tool will have significant impact on public health by improving survival and decreasing mortality. The early diagnosis and surgical removal of malignant lesions will also lead to a reduction of treatment costs as chemotherapy and radiotherapy can be avoided. Patient recovery time, as well as rehabilitation costs, will also be reduced.

The main objective of the research presented in this thesis, is the development of a prototype system to demonstrate the technological feasibility of an IR fluoroscopic cancer screening capsule, and validation of the capsule's performance through some preliminary in-vitro and ex-vivo tests. The innovation presented is at the system level, implementing a unique prototype that requires extensive multidisciplinary skills to complete the following key tasks:

(1) The design and validation of the optical and phototransductive system;

(2) The design of a mixed-signal electronic system with minimised power con-

sumption, thus allowing continuous operation for almost 8 hour (the average time that the capsule needs to scan the gastrointestinal track);

(3) The design of a docking unit for the recovered capsule, which includes a contactless data recovery system and interface to a computer; and

(4) The development of a compact-size prototype, suitable to pass through the gastrointestinal tract of a medium size animal (i.e. swine) for future in-vivo testing (carrying out the in-vivo testing is outside of the scope of this project).

1.3 Existing Knowledge

The convoluted structure of the largest part of the small bowel prevents flexible endoscopes from accessing it. The medical community has long recognized the need for an alternative diagnostic/screening procedure that would overcome that limitation. This need has led to the development of various endoscopic capsules [8, 12, 15, 20, 42, 63, 87, 104] that offer visual access to parts of the small intestine in a less invasive way (Figure 1.1a). However, conventional white light imaging techniques rely on the examination of the physical appearance of the GI track for late diagnosis (such as areas with abnormal morphological or color appearance, as those seen in Figure 1.1b). Thus, this is not always sufficient for detecting cancer at an early stage, which frequently has unchanged color and morphology.

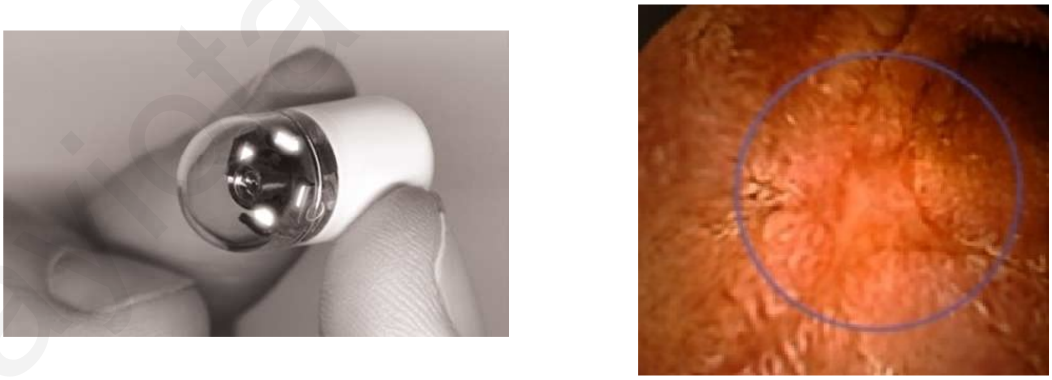
(a)

(b)

Figure 1.1: a) Currently available endoscopic capsule. b) White light image of a tumor, taken from an endoscopic capsule.

A well known technique used for efficient microcancer detection is infrared fluorescence endoscopy (IRFE) in conjunction with an infrared fluorescent-labeling contrast agent [50]. Specific antibodies tagged with Indocyanine Green (ICG) derivatives can label cancer cells by generating a strong enough infrared fluorescence (IRF) signal [47,49]. However, this technique has, so far, been limited to use with an IRF endoscope. Furthermore, statistics on fluorescence imaging for early cancer detection in the GI track show that very early-stage cancers are better visualised under fluorescence imaging than conventional white light examination [34, 103]. More specifically, the sensitivity of a fluorescence system was found to be 5.3 times greater than that of the white light imaging procedure in detection of carcinoma in situ of the lung [76]. Thus, current commercial capsules do not have sufficiently high sensitivity to detect fluorescence, as the pixel size is too small, and none of them has the narrowband optical filters incorporated to detect a weak fluorescence signal near the strong excitation wavelength. Finally, current capsules are designed to output images, rather than detect increased levels of fluorescence. Thus, they require real-time telemetry links to the outside of the body, as well as an external belt receiver to collect the data, which increases their cost and power requirements. Moreover, they are impractical for basic screening tests, due to the labour intensive video analysis.

A step in the right direction for primary cancer diagnosis was the development of an endoscopic imaging system that offers additional imaging modes, i.e. autofluorescence (AFI), Narrow Band (NBI, Figure 1.2a and 1.2b) and infrared (IRI) imaging, in addition to the conventional white light imaging [31, 90]. Nevertheless, this is still a classical endoscopic system and cannot access the small intestine effectively.

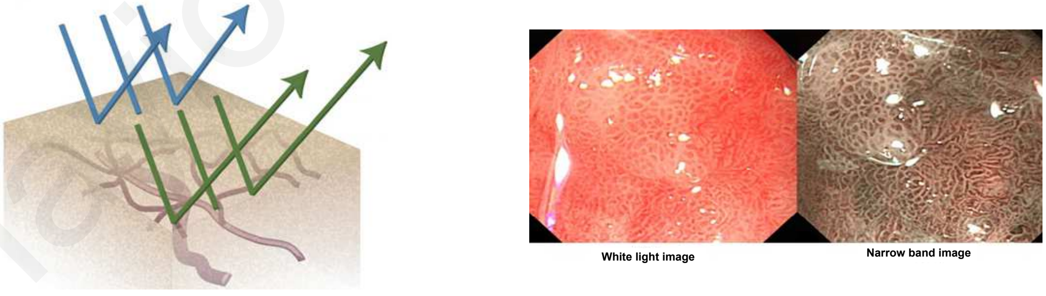

(a)

(b)

Figure 1.2: a) NBI technique illuminates tissues with different narrow band wavelengths and records their reflection. The longer the wavelength is, the deeper the tissue is penetrated resulting in a more contrast-enhanced image of the micro vessels structure. b) White light image compared with a narrow band image of a tissue.

One capsule that targets early cancer diagnosis [26] attempts to do so with narrow band and white light imaging. Narrow band images enable selective depth imaging of microvascular structures that can help a specialist to identify the existence of a carcinoma. However, external equipment is required for receiving the images that are transmitted from inside the body. Also much manpower is required to scan through the acquired footage. These make the capsule inefficient for basic cancer screening.

Another capsule that uses autofluorescence [48] is currently too big to be practical (2.64 cm x 8.26 cm) and the authors state that it cannot be miniaturised any further. Al-Rawhani et al. [6] have shown the feasibility of an autofluorescence based capsule prototype, which requires power hungry single photon avalanche diodes (SPADs). The presented prototype only scans a small portion of the intestine walls; to scan all 360°, the power budget will increase significantly. Also, autofluorescence screening of flavin adenine dinucleotide (FAD) lags of sensitivity compare to infrared fluorescence screening, due to the high background noise produced by the autofluorescence of other components in human tissues. Furthermore, autofluorescence in the intestine is diet dependent [44].

Further work has been done towards tissue fluorescence detection, via the development of an on-chip integrated optical sensor for autofluorescence [24], however this work did not materialise into a complete system, to include the excitation source, optical filters, electronics, memory and/or communication circuits. Also the photodiodes are small, at approximately 50x50 um^2, and are thus unable to provide the required sensitivity.

Therefore, there is a necessity for the development of an IR fluorescence based endoscopic capsule, capable to provide a general screening method for primary intestinal cancers. It will do so, by detecting fluorescence levels emitted from molecular agents that have increased density of fluorescence at cancerous sites compared to the background fluorescence of healthy cells. The fluorescence data will be collected internally, thus eliminating the need for a transmitter and an external data receiver. Such a method also eliminates image collection, thus trained experts are not required to analyse eight or more hours of video for each patient; they can quickly examine if the detected fluorescence levels exceeded a predefined threshold when plotted on a chart.

1.4 Overview

The research presented in this thesis involves the design and implementation of a novel IR fluoroscopic screening capsule for cancer detection in the small intestine. Remainder of the thesis is organized as follows:

Chapter 2 provides background information on fluorescence phenomena and fluorescence spectroscopy in conjunction with molecular biomarkers, and how these are related to the presented research. Information about endogenous and exogenous fluorophores, as well as near-IR fluorophores and their advantages for biomedical diagnoses, are also presented.

Chapter 3 deals with all the issues related to the optical and photo-transducer part of the capsule. Building a fluorescence detection system with severe power and space constraints is not trivial. This chapter includes an analysis of the parameters considered for the selection of the appropriate light source, optical filter, photodetector, housing material etc.

Chapter 4 presents all the steps and various design considerations for the hardware implementation of the fluoroscopic screening capsule. A complete, compact-size, mixed-signal electronic system is presented, which is able to detect and distinguish IR fluorescence intensity levels. Several advanced features are also presented, which are related to storage and power management, and the wireless data recovery of the capsule.

Chapter 5 concludes the thesis and highlights the contributions of the presented research. Finally recommendations are made for future work in this area.

Chapter 2

Fluorescence Spectroscopy and Fluorescent Biomarkers

This chapter first introduces the reader to background knowledge on fluorescence phenomena and spectroscopy. Next an introduction to diagnostic methods based on fluorescence biomarkers is presented. Finally, this chapter presents the instrumentation required to implement these methods and how all the above relate to the research targets.

2.1 Basic Principle of Fluorescence Spectroscopy

Fluorescence spectroscopy is an important tool for biomedical diagnostics [95]. It is used extensively for characterization of cardiac tissue, blood and vessels analysis, and aiding the screening and early detection of cancer. Fluorophores have a central role in fluorescence spectroscopy and fluorescence imaging. A fluorophore, otherwise known as a chromophore, is a substance composed of particular molecules with the ability to absorb light in a specific wavelength range, leading to excitation in higher energy levels and to an almost instant emission of light in a longer wavelength spectrum. The emitted light has lower energy than the excitation light. Sir George G. Stoke was the first who described this phenomenon in 1852 and named it fluorescence as he firstly observed this in Fluorite [93, 94].

Fluorescence can be understood better through a brief overview of the N.Bohr atomic model. Based on this model, electrons can only orbit the nucleus of the atom in particular orbits with fixed energy and angular momentum. When the atom absorbs energy from electromagnetic radiation, electrons move to higher fixed energy levels and then return to a lower available energy level by emitting back radiation in the form of photons. Photons have quantised energy equal to the difference of the two energy levels. The wavelength of the photon is equal to:

$$\lambda = \frac{c.h}{E_{ph}} \tag{2.1}$$

where h is Planck's constant ($6.63 \times 10^{-11} Js$), c is the velocity of light in vacuum ($2.998 \times 108 ms^{-1}$) and E_{ph} is the energy of the photon.

Accordingly, each molecule has its own characteristic quantum electronic energy levels, in which it can be excited with the absorption of energy. A portion of that energy maybe spent in vibrating and rotating the atoms, hence electronic energy levels are divided into vibrational and rotational energy levels. Figure 2.1a is an example of the schematic representation of the energy levels of a simple two-atom molecule. Therefore, fluorescence typically occurs at lower energies at longer wavelengths than that of the absorption light as some of that energy is internally utilized by the atom for vibrational and rotational relaxations. Figure 2.1b shows a typical Jablonski fluorescence energy diagram with the typical average lifetime of the different processes.

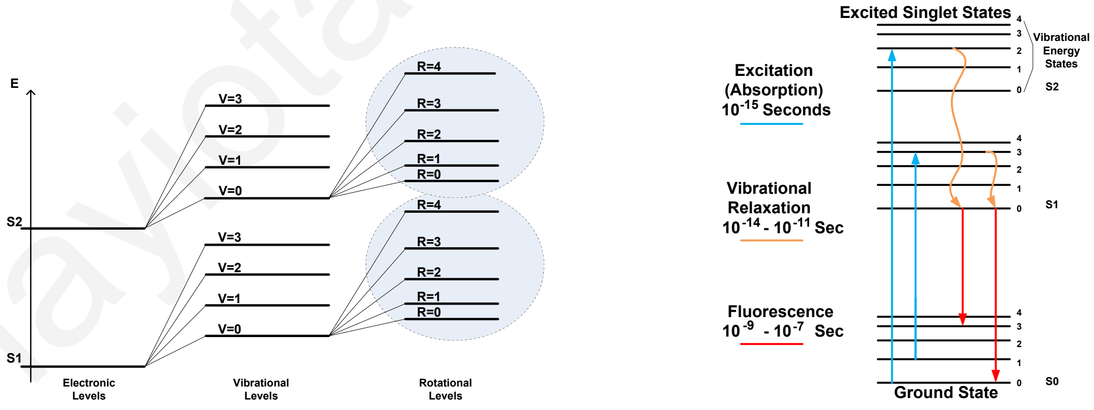

(a)

(b)

Figure 2.1: a) The electronic, Vibrational and Rotational energy levels of a two-atoms molecule, b) Jablonski Energy Diagram of fluorescence and the typical average lifetime of the different processes.

A fluorophore is characterised by the absorption (excitation) spectrum and the emission (fluorescence) spectrum, which is specific for different fluorophores. Fluorescence spectroscopy uses those spectra for the identification and detection of several biological fluorophores. The excitation and emission spectra of several chromophores are given in Figure 2.2 as an example. The wavelength at which a maximum excitation is observed corresponds to the wavelength with the highest probability of absorption, i.e. that can cause the most effective excitation to the molecules. Similarly, the emission maximum is the wavelength which is more likely to be emitted. The difference between these two wavelengths is called ”Stoke Shift” and is a key aspect in the detection of the emitted fluorescence in biological applications. The Stoke Shift is a distinct characteristic of each fluorophore arising from the structure of the molecule’s energy levels. A small Stoke Shift makes the detection of fluorescence more difficult as the excitation and emission spectra are overlapping. The bigger the Stoke Shift is, the easier it is to filter out the excitation light in an attempt to observe the fluorescence spectrum or measure its luminescence intensity.

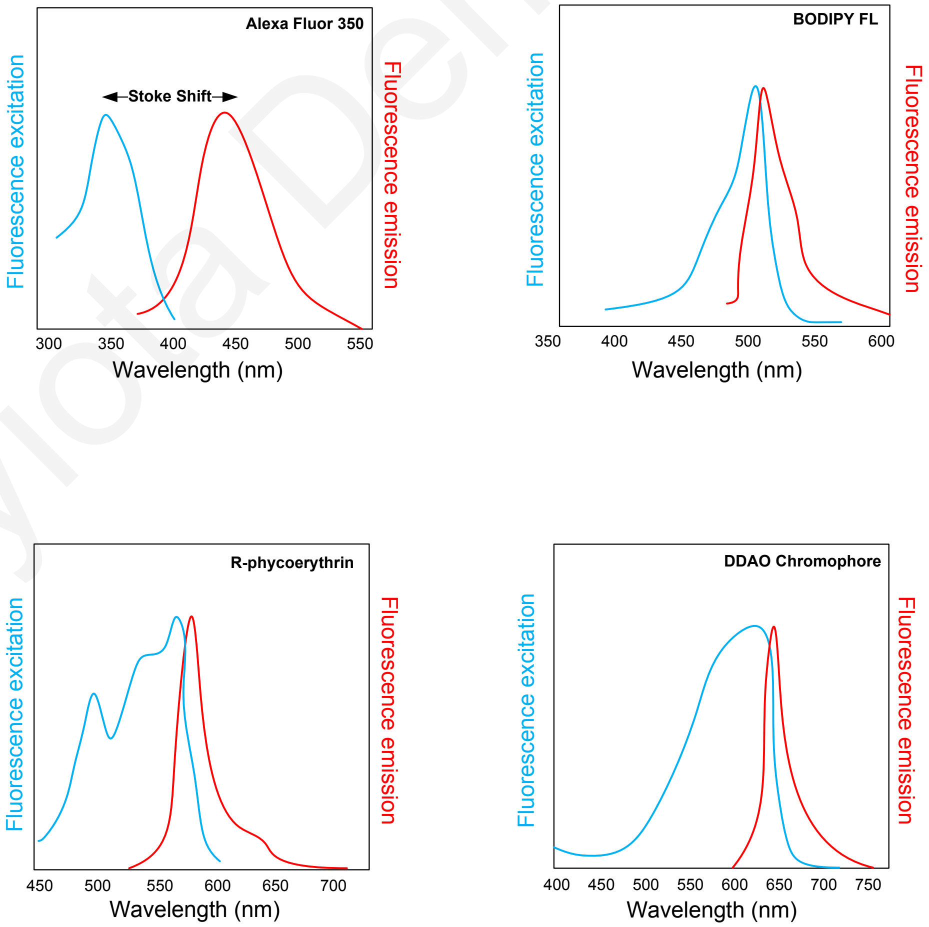

Figure 2.2: Excitation and Emission spectra of several dyes.

Another general property of fluorescence is that the emission spectrum intensity is dependent on the excitation wavelength. A decrease in fluorescence intensity is observed when the chromophore is excited with light whose wavelength is any other than the absorption maximum wavelength that gives fluorescence of highest intensity (Figure 2.3).

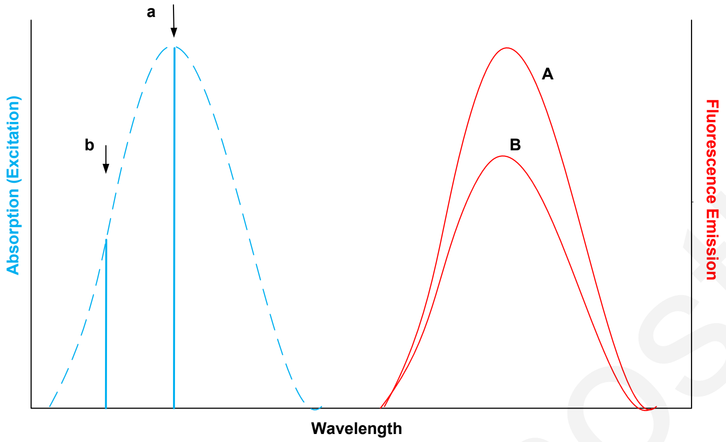

Figure 2.3: Excitation with the maximum wavelength *a* causes a fluorescence response with spectrum *A* (highest intensity). Similarly excitation *b* gives an emission spectrum *B*.

Fluorescence-based diagnostic methods can be classified into two groups:

1. Methods that detect endogenous fluorophores in tissues,
2. Methods that use/detect exogenous fluorophores.

The following sections provide more details for these two methods.

2.1.1 Endogenous Fluorophores

Biological tissues are inundated by a large number of endogenous (naturally occurring) fluorophores, which are extremely useful for medical imaging applications [65]. Those substances have the ability (when they are illuminated at a specific excitation spectrum) to produce autofluoresence, which makes them visible, distinguishable and detectable. They are generally associated with cellular structure and metabolism, hence they can provide significant information about differences in tissues. The majority of those biochemicals become excited and fluorescent in the UV and visible spectrum. Figure 2.4 shows the absorption and emission spectrum of several tissue fluorophores, including predominant ones, such as flavins (FAD), reduced nicotinamide adenine dinucleotide (NADH), elastin and collagen.

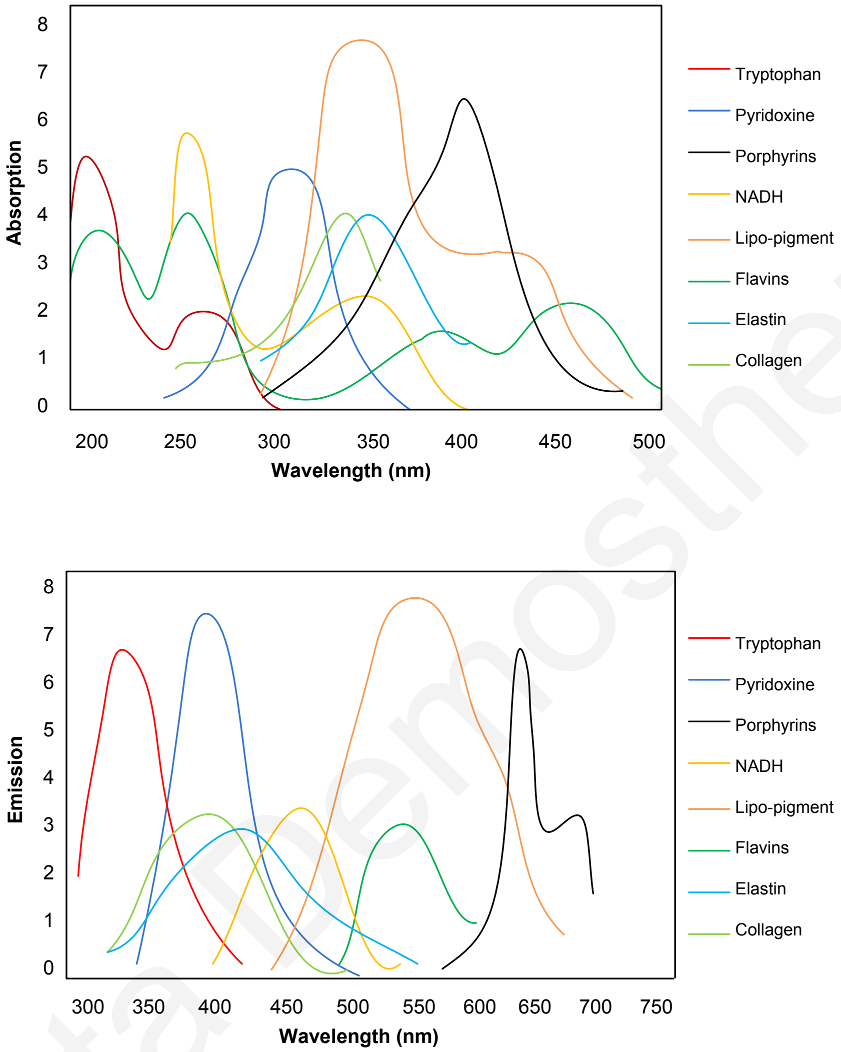

Figure 2.4: Absorption and Emission spectrum of several tissue fluorophores [96].

Autofluorescence spectroscopy has been used efficiently for primary gastric cancer diagnosis [34], [58], [62], [100], [61], since cancerous cells often undergo changes in their metabolism and structure leading to differences in their fluorescence emission spectrum. In particular, NADH and FAD levels in epithelial tissues change during neoplastic transformation. A decrease in the ratio of FAD over NADH is generally indicative of an increased metabolic activity. Similar, autofluorescence coming from protein collagen and elastin of submucosa has decreased intensity in cancerous compared to healthy tissues due to the increased blood flow and thickened mucosa layer (figure 2.5).

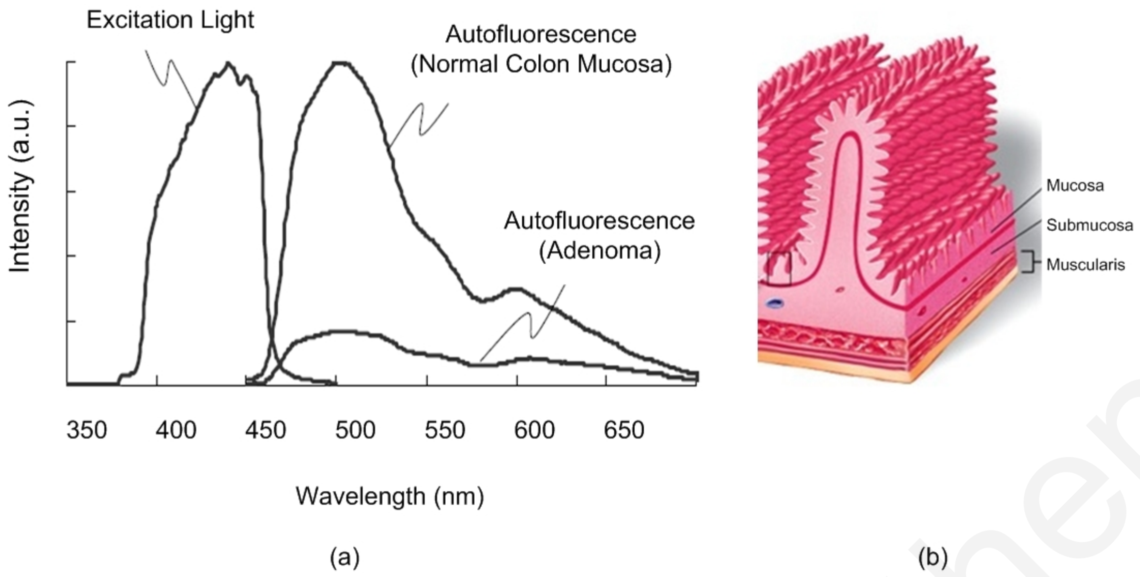

Figure 2.5: a) Decreased autofluorescence of collagen in cancerous tissues compare to healthy tissues [34], b) Intestine physical structure of tissue layers.

2.1.2 Exogenous Fluorophores

There are many biological tissues with no endogenous fluorophore, which cannot be observed through autofluorescence. For that reason, exogenous fluorophores are used for staining those biological tissues, so as to make them visible to fluorescence imagers [102]. Exogenous fluorophores are either target biological molecules without any prior coupling to another biomolecule, or they are conjugated with biomarkers (ex. proteins) for selective staining specific sites in cells (figure 2.6).

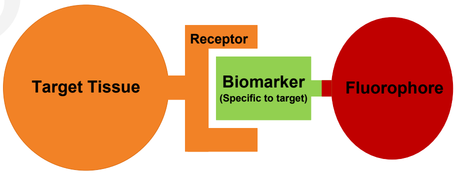

Figure 2.6: Exogenous Fluorescent-Molecular Probe Mechanism.

In order for a fluorophore to play the role of an exogenous contrast labelling agent, the fluorophore must:

- be soluble in the biological medium to be probed,
- have environmental stability,

- have specific association with the target molecule; otherwise, it must be chemically conjugated with the proper biomarker that will bond the fluorophore to the target receptor,
- not suffer from photobleaching, which is a chemical degration that leads to the disappearance of fluorescence,
- have high quantum efficiency of emission (defined as the number of photons emitted over the number of photons absorbed)

Moreover, exogenous fluorophores need to have an excitation spectrum that does not belong to the excitation spectrum of endogenous fluorophores. In particular, they should have an absorption spectrum at longer wavelengths, where no excitation and no autofluorescence of the endogenous fluorophores occurs, when the excitation of exogenous fluorophore takes place. In this project, an infra red exogenous fluorophore has been selected, so as to limit the existence of background autofluorescence, which reduce the signal-to-noise ratio and the overall sensitivity of the detection process.

2.2 Near-Infrared Fluorescence and NIR Fluorophore

The use of near-infrared fluorescence (NIRF) imaging techniques for sensitive early cancer detection is highly desirable for several reasons. Biological tissues exhibit good transparency in the NIR spectrum and also show low autofluorescence resulting in an increase of the signal-to-noise ratio. Photon penetration into living tissue is highly dependent on the absorption and scattering properties of the tissue components. Within the NIR spectrum, scattering is the most dominant light-tissue interaction and is increased for photons of lower wavelengths; the longer the wavelength of the light, the deeper it penetrates into the biological specimen. Moreover, the NIR window is primarily limited by the light absorption of blood at short wavelengths and water at long wavelengths. Water is considered to be one of the most important absorbers in biological tissues, dominating around 60 to 80 percent of the tissue. It has a relatively low absorption between 200 and 900 nm (Figure 2.7) and this allows NIR light to penetrate several centimetres into the tissue [16, 17, 60]. However, the lower limit of light transmission in tissue is defined up by the absorption of Haemoglobin, which constitutes approximately 40-45 percent of the blood composition. Figure 2.8 shows the absorption spectrum of the two different types of haemoglobin that present higher absorption below 700 nm [41,80,108].

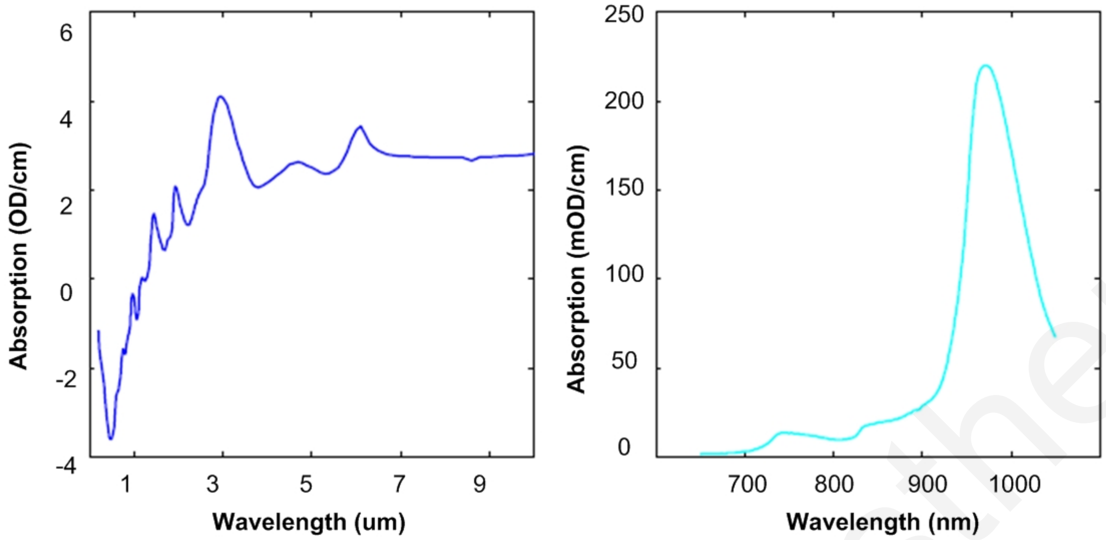

(a)

(b)

Figure 2.7: a) The absorption spectrum of pure water on a log scale from 0.2-10 um, b) The NIR region from 650-1050 nm.

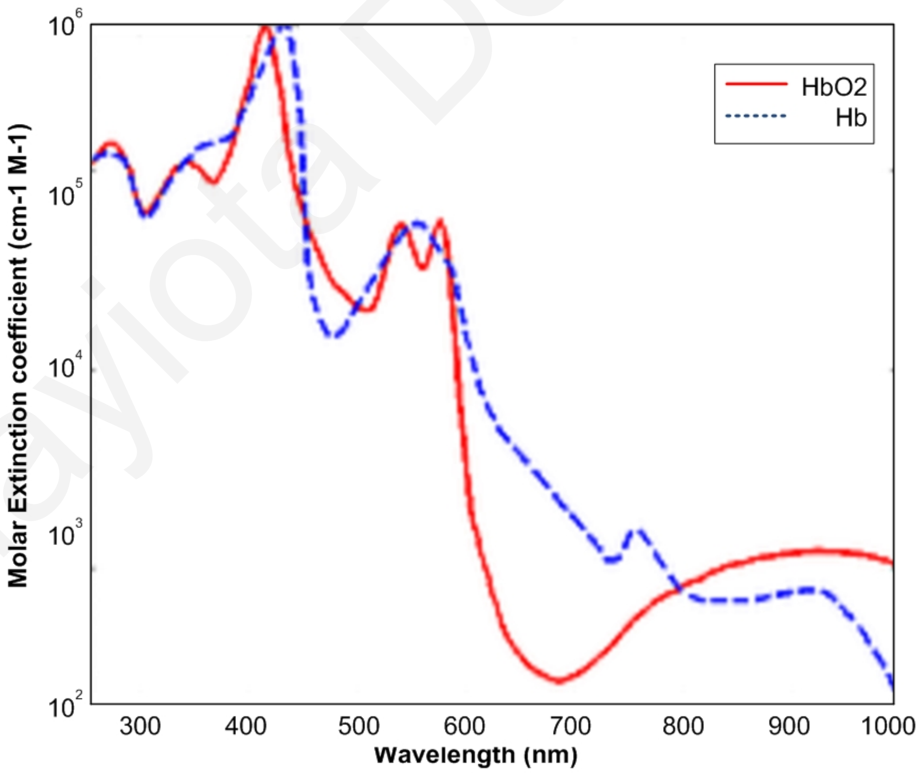

Figure 2.8: The absorption spectrum of Oxyhaemoglobin (HbO2) and Deoxy-haemoglobin (Hb).

Near Infrared Fluorescence Imaging requires exogenous NIR fluorophores to play the role of the contrast agent that will effectively stain the sites of interest in the biological tissues. NIR dyes have better performance than visible fluorophores and are able to enhance detection sensitivity and signal-to-noise ratios in applications where autofluorescence is limited [27,57,105]. The advantage of using such NIR dyes is that their excitation in near IR produces low autofluorescence from endogenous chromophore. Hence, the sensitivity of detection, which is often limited by the autofluorescence background, is significantly improved. In addition excitation with longer wavelength and fluorescence at near IR spectrum gives reduced scattering in the tissues and, thus increases both the penetration depth and the collection efficiency of emission as more fluorescence photons manage to reach the sensor.

In contrast to the above properties, NIR dyes sometimes present some limitations, such as low quantum efficiency, insufficient stability in biological systems that consist mainly of water, high probability of experiencing photobleaching, and poor hydrophilicity and photostability.

A well known, frequently used NIR fluorophore is Indocyanine Green (ICG) that has been used clinically for over 60 years for hepatic function, determining cardiac output, cardiovascular function testing, liver blood flow and retinal angiography [7, 11, 23, 59]. Several studies also use and develop biomarkers that are conjucated with ICG antibodies for micro cancer detection, including gastrointestinal cancer [9, 39, 43, 45, 46, 54, 67, 68, 73, 83, 89, 97]. Some of the important properties of ICG, which make it attractive for Near-IR fluorescence cancer diagnosis, are presented in the following section.

2.3 Indocyanine Green a Near-IR Exogenous Dye

Indocyanine Green (ICG) is a cyanine dye approved for medical use as a diagnostic for intravenous use. Its toxicity can be classified as low [56]. It has molar mass 774.96 g/mol and chemical structure is shown in figure 2.9. It is water soluble without changing the refractive index of the solvent. ICG presents high absorption in the NIR spectrum at a range of 600 to 850 nm and has almost no absorption in the visible spectrum (Figure 2.10). Its fluorescence has an emission spectrum around 780 to 880 nm with emission maximum at 820 nm and a lifetime around 1.5 ns as is calculated with time-resolved methods [30] (Figure 2.11).

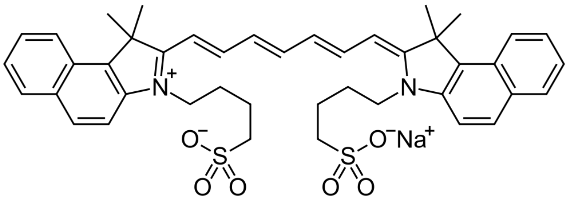

Figure 2.9: Chemical Structure of ICG.

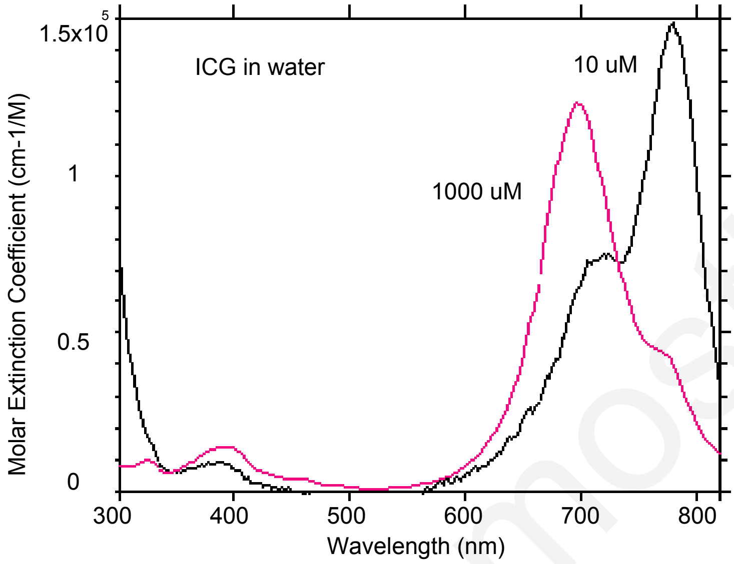

Figure 2.10: Absorption (Excitation) Spectrum of ICG [1].

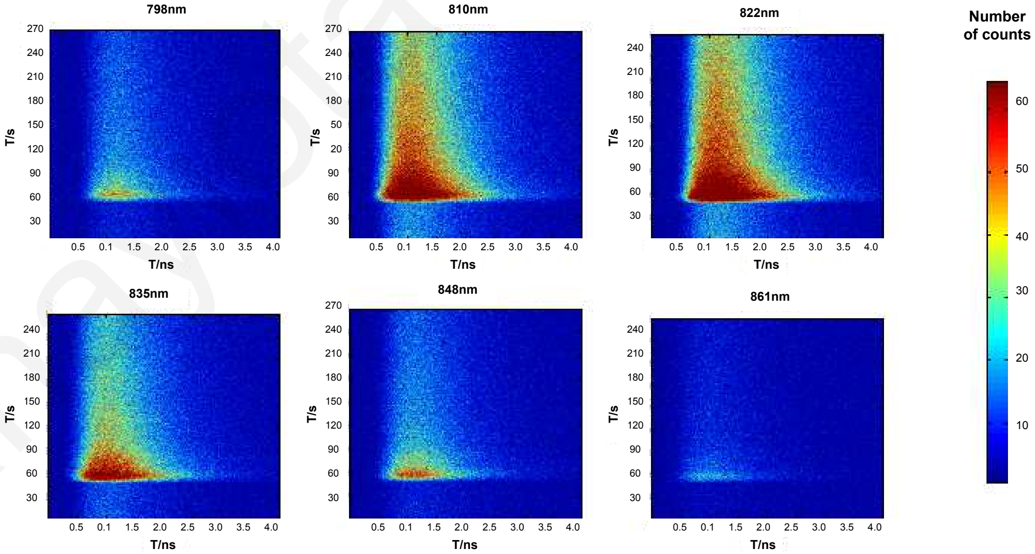

Figure 2.11: Fluorescence of ICG in time for different emission wavelengths [30].

The absorption properties of ICG follow to Beer law:

$$A = e * c * d \tag{2.2}$$

where A is absorbance of a solution, e (liters/moles.cm) is the molar extinction coefficient of the solution at the measured wavelength which represents the probability of absorption of incident radiation, c (moles/liter)is the molarity (concentration) of the solution and d(cm) is the optical path length. The molar extinction coefficient of ICG changes for different concentrations of the solution (Figure 2.12), thus absorbance is not linearly dependent of concentration. Furthermore, absorption of ICG is not only dependent on ICG concentration, but is also affected by the solvent. For example, in Figures 2.13 and 2.12 the absorption maximum of ICG in plasma is at 800 nm and in water is at 780 nm; a shift of almost 30 nm of the maximum in longer wavelength is observed.

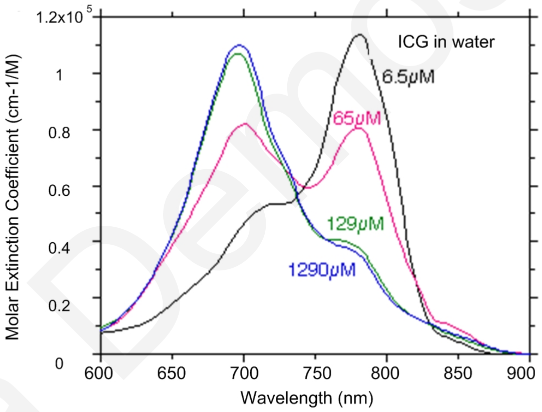

Figure 2.12: The absorption changes of ICG as the concentration of ICG changes. If ICG strictly followed Beer's law then the curves in this figure would coincide [1].

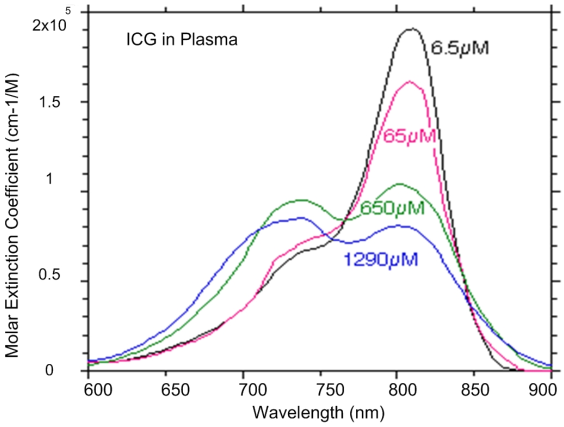

Figure 2.13: The absorption changes of ICG at different concentrations in plasma [1].

The ICG absorption spectrums consist of two main peaks, at 708 nm and at 780 nm (Figure 2.14). The two absorption maxima correspond to two forms of the dye: the monomeric form (780 nm) and the oligomeric form (708 nm). With increasing concentration of ICG, the content of monomers decreases and the absorption maximum is shifted to shorter wavelengths. This reflects an increase in the content of oligomers in the solution [92].

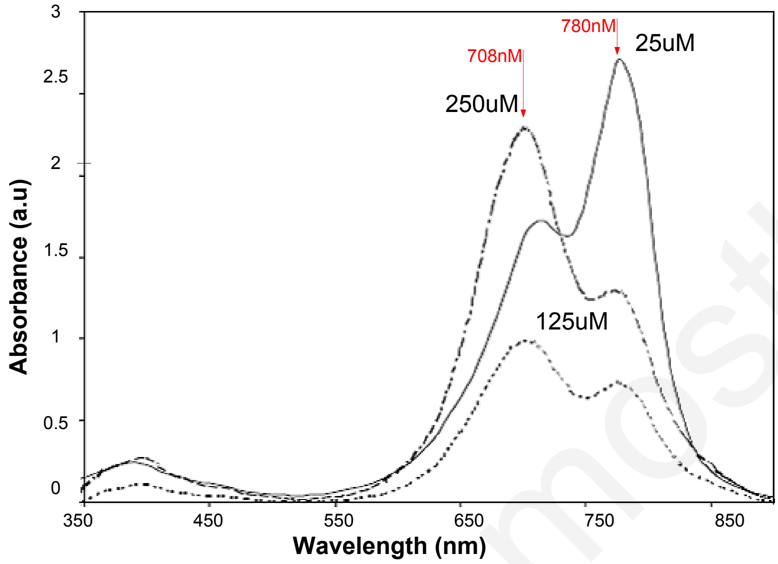

Figure 2.14: The absorption spectrum of ICG with two peaks at 708 nm corresponding to ICG monomeric form and at 780 nm corresponding to oligomeric form [92].

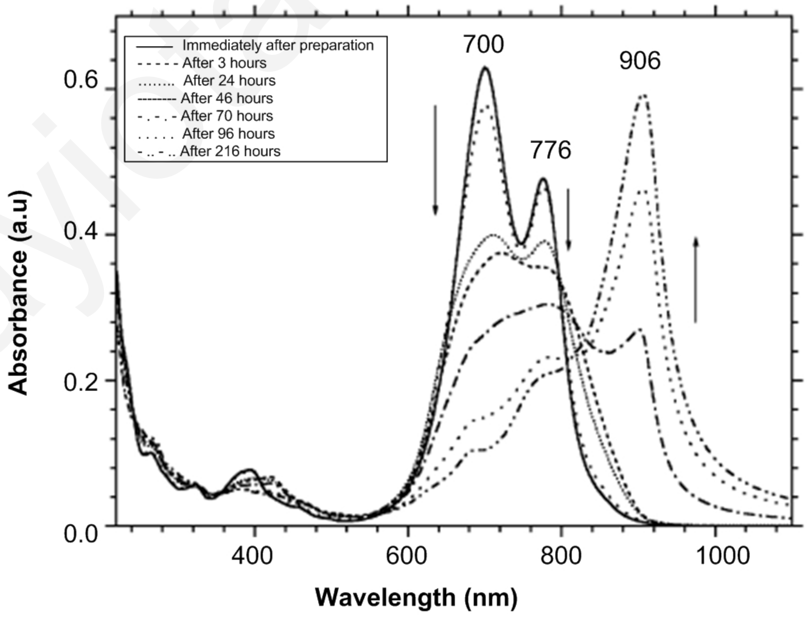

Figure 2.15: The degradation of ICG over time with the peak maximum at 906 nm after 96 hours [35].

ICG solutions of lower concentrations are characterised by lower stability, since their optical properties change over time. However, these changes occur after many hours beyond the time the capsule needs to pass through the GI tract. Figure 2.15 shows the behaviour of ICG over time (indication with down-going and then up-going arrows), the absorption spectrum of 30 umol/L ICG with maximum at 700 nm and 776 nm disappears and is replaced by a new absorption spectrum with maximum at 906 nm after 96 hours [35]. Another disadvantage is that ICG has a weak emission compared to the excitation intensity, by a factor of about hundred to thousand times, which makes the detection of fluorescence more challenging as the excitation spectrum is very close to the emission spectrum, at a stoke shift around 40 nm.

The decision of using ICG as the dye to be detected from the endoscopic capsule prototype was taken after considering the plethora of advantageous properties characterising this fluorophore. Concurrent research that took place at the University of Cyprus investigated the implementation of biomarkers conjugated with ICG targeting epidermal growth factor receptor (EGFR - at cells-surface), which is associated with cancerous cells [69,70,74,75,98]. Based on that research area, some preliminary calculations were made to find the critical concentrations of ICG related to abnormal and healthy tissues. According to reference [32], EGFR mole concentration per mg of tissue was found to be around 300 fmol/mg and 25fmol/mg for cancerous and control tissue respectively(Figure 2.16).

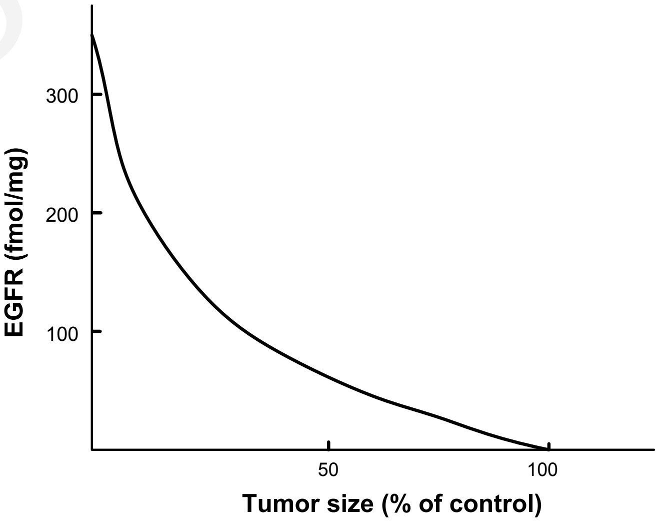

Figure 2.16: EGFR concentration in cancerous tissue [32].

This significant difference of EGFR concentration between cancerous and healthy tissue can be used for cancer detection. Thus, with an assumption that 75 percent of the EGF receptors are uptaken by ICG biomarkers, ICG mole concentration per mg of cancerous tissue is 225 fmol/mg , as opposed to 19 fmol/mg for healthy tissue. Considering that around 80 percent of tissue is dominated by water, the specific weight of human tissue can be considered as approximately equal to water density, i.e. 1 mg/mm^3 then the molarity of ICG for abnormal and healthy tissue is 225 nM (nmol/L) and 19 nM respectively. These ICG concentrations are the key factors for the implementation of the fluoroscopic cancer screening capsule, since the fluorescence-microscope-in-a-pill system should be able to detect these differences in ICG concentration, targeting a more sensitive detection of cancer in the small intestine.

Studies on emission properties of ICG of relatively low concentrations in an intralipid solution ranging between 0 to 20 uM [99] has shown that: At low-concentration regions the emission strength increases with ICG concentration, as opposed to high-concentration regions where the emission decreases with the concentration. In general, there is a maximum of emission strength as a function of concentration, whose position depends on the wavelength of the excitation light, the distance between the source and the detector, and the sample geometry and size. Two factors contribute to the decay of emission strength: the ”inner-cell effect” and re-absorption of emitted photons. The first is related to the decrease in penetration depth of the excitation light, as ICG concentration increases. This phenomenon, known as ”inner-cell effect”, results in the excitation of less sample volume and, thus, decreases the fluorescence intensity. Samples of relatively small size and cylindrical geometry present lower influence in ”inner-cell effect” compare to sample of infinite geometry; hence, the emission maximum appears at higher concentrations (Figure 2.17). In contrast, the re-absorption of emission photons dominates in samples of small size, resulting mainly in the decrease of detected fluorescence. Furthermore, as is shown in Figure 2.17a, emission properties differ for different source-detector separations (rsd) and different excitation wavelengths of 660 and 780 nm. At the excitation wavelength 780 nm, the maxima are located at concentrations of 0.3 uM and 0.4 uM for source-detector separation equal to 1.0 cm and 1.6 cm respectively, since the ”inner-cell effect” decreases at lower source-detector separations. At 660 nm, a relative flat region appears from 1.7 to 2.7 uM ICG. For the cylindrical geometry in

Figure 2.17b, the concentration values of maximum emission are located between 4 and 6 uM for both excitation wavelengths of 660 and 780 nm. These values are much higher than those of infinite geometry.

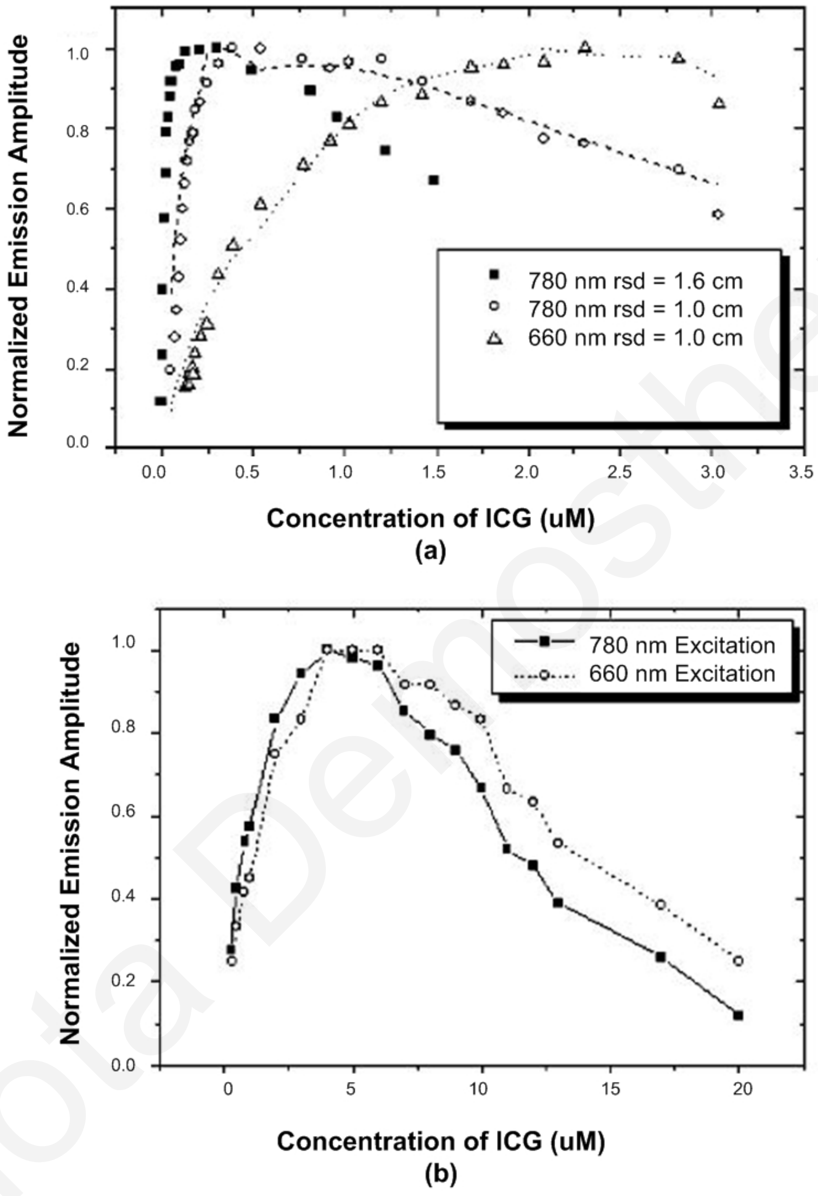

Figure 2.17: Normalized emission amplitude of ICG in Intralipid solution as a function of ICG concentration. a) Infinite sample geometry and b) Cylindrical small size geometry [99].

The above properties and results on the background knowledge of ICG, are provided by a plethora of references [10,29,36,40,53,55,79,81,82,86,99,107]. Nevertheless, most of these properties needed to be verified again and quantified by using existing equipment in the lab, before proceeding with the design of the capsule. The results are given in the following sections.

2.4 Fluorescence Spectroscopy Instrumentation

This section introduces the reader to the instrumentation used in fluorescence spectroscopy. A typical spectrofluorometer consists of an excitation source, a sample cuvette, fluorescence detector and monochromators to isolate the incident light and fluorescent light (Figure 2.18). The light from the light source passes through a monochromator and excites the fluorophore at different wavelengths. The emitted fluorescence, which propagates in all directions, is dispersed by another monochromator and detected by a photodetector which outputs the characteristic emission spectrum of the dye. Most spectrofluorometers can record both excitation and emission spectra. For measuring the excitation spectrum the wavelength passing though the emission monochromator is kept constant, preferably at the emission maximum wavelength, and fluorescence intensity is measured at the output, while the excitation monochromator is scanning at different wavelengths causing the excitation of the substance. The excitation spectrum is in general identical to the absorption spectrum, as the fluorescence intensity is proportional to the absorption. Similarly, when recording the fluorescence (emission) spectrum the wavelength of the excitation light stays constant, preferably at the absorption maximum wavelength, while the emission monochromator scans the emitted spectrum.

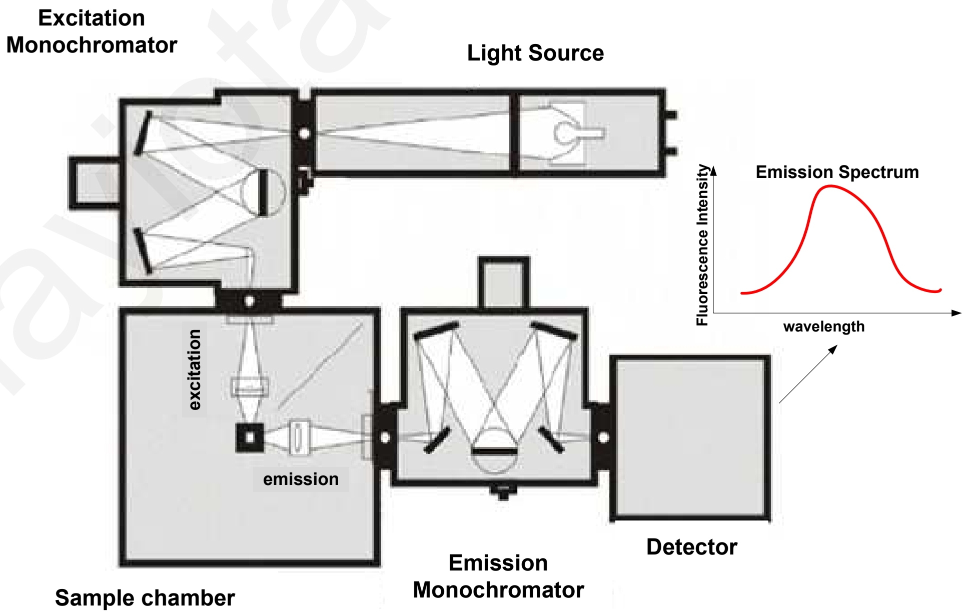

Figure 2.18: A typical set-up of a spectrofluorometer.

In a simple fluorometer the source monochromator can be replaced by a filter (or narrowband source, e.g. LED, LD), whilst the detection monochromator can be replaced by an optical filter and a photodiode as a detector. This set-up measures only the photodiode's induced photocurrent, which is proportional to the incident fluorescence intensity. Despite the presence of an emission filter to attenuate the intensity of the excitation wavelengths, it is usual to place the detector at 90 degrees to the sample so as to avoid direct exposure of the detector to the source. The intensity of reflections at the various interfaces is still lower than a direct path. (Figure 2.19).

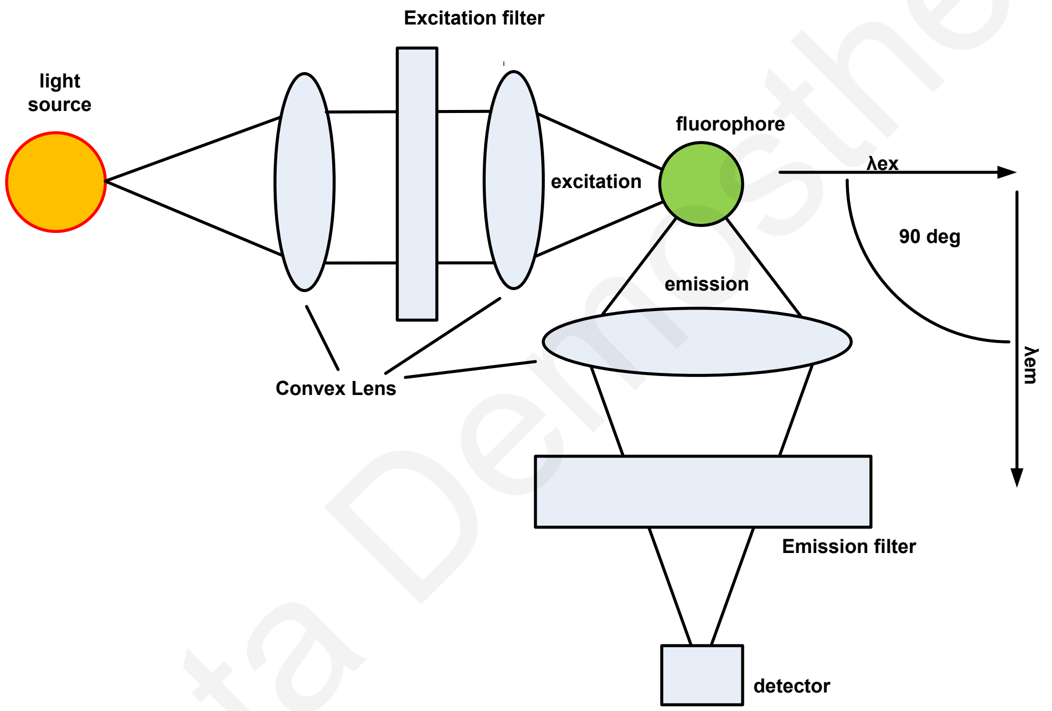

Figure 2.19: A simple fluorometer for measuring fluorescence intensity.

The presented capsule prototype system uses the general idea of a fluorometer in a more compact manner in order to fit in a pill-dimension case. In the following chapters a more descriptive overview of the screening system structure will be presented, as well as all the considerations that were taken into account based on the desirable specifications.

Chapter 3

Optics and Optoelectronic Aspect of the Capsule Fluorometer

The challenging nature of fluorescence detection is complicate accentuated by the requirement of fitting a fluorescence level detector in a pill. Fluorescence signals are usually of very low intensity, a crucial consideration when choosing the light source and detector. In addition, fluorescence intensity is several orders of magnitude smaller than the excitation light, thus the use of specialized filters is necessary to block the excitation source to allow detection of the emitted fluorescence signal. If only a small fraction of the laser emission is detected, then the more intense light will be detected at the photodetector, drastically reducing sensitivity to the lower-intensity fluorescence signals. The choice of filters is complicated even more if one considers that the excitation and emission wavelengths are only 30-40 nm apart, based on the Stoke Shift of indocynine green dye. In conclusion, a very intense, narrowband excitation signal irradiates the tissue, whilst an adjacent narrow band detector detects a weak fluorescence signal.

This chapter deals with the design of the optics and photo-transducer part of the capsule, such that the challenges related to fluorescence detection can be overcome. The search for various light sources/detectors/filters etc, in order to choose the components most appropriate for this specific application and experimental validation, is described. More specifically this chapter targets the following objectives:

1. the selection of the optimal light source, optical filters and detector,

2. the determination of the optimal position of the optical components to maximise sensitivity, and

3. the determination of the right material for the capsule and index-matching epoxy that will fill the inside of the capsule case, in order to limit light reflections back to the detector.

3.1 Excitation Light Source Selection

The selection of an appropriate excitation light source with the desirable radiation spectrum and emission maximum wavelength requires the knowledge of the absorption spectrum of ICG. Although the absorption spectrum of ICG is already known and was discussed extensively in chapter 2 (section 2.3), experimental investigations were also performed for validation purposes and the absorption spectrum of different ICG concentrations was measured.

The ICG samples were placed in an absorption spectrometer (210 VGP) and the results from several ICG concentrations are shown in Figure 3.2, including concentrations of interest near the critical concentrations of 250 nM and 25 nM, which represent cancerous and healthy tissues respectively (chapter 2, section 2.3). The main conclusion extracted from this investigations is that the excitation maximum wavelength of the light source should be around 780nm, since the absorption maximum of low concentrations of ICG was observed at this wavelength.

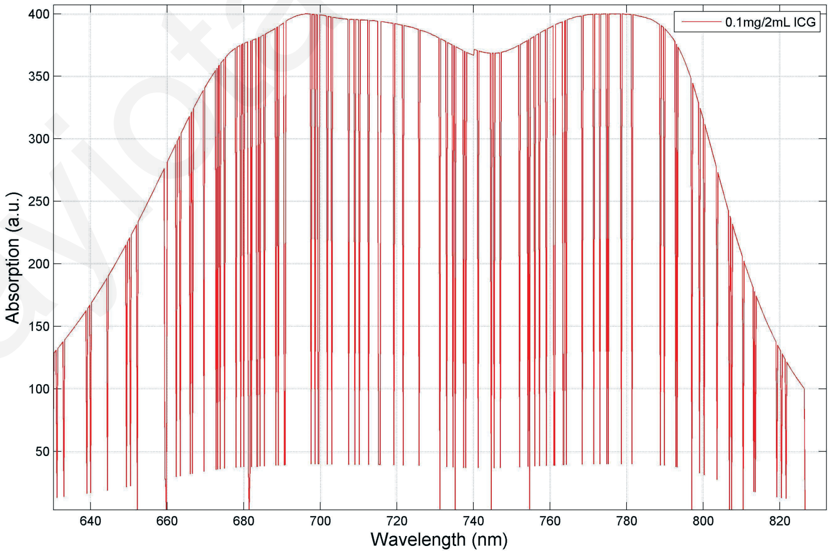

Figure 3.1: Experimental results of the absorption spectrums of ICG with concentrations at 64uM (0.1mg/2mL).

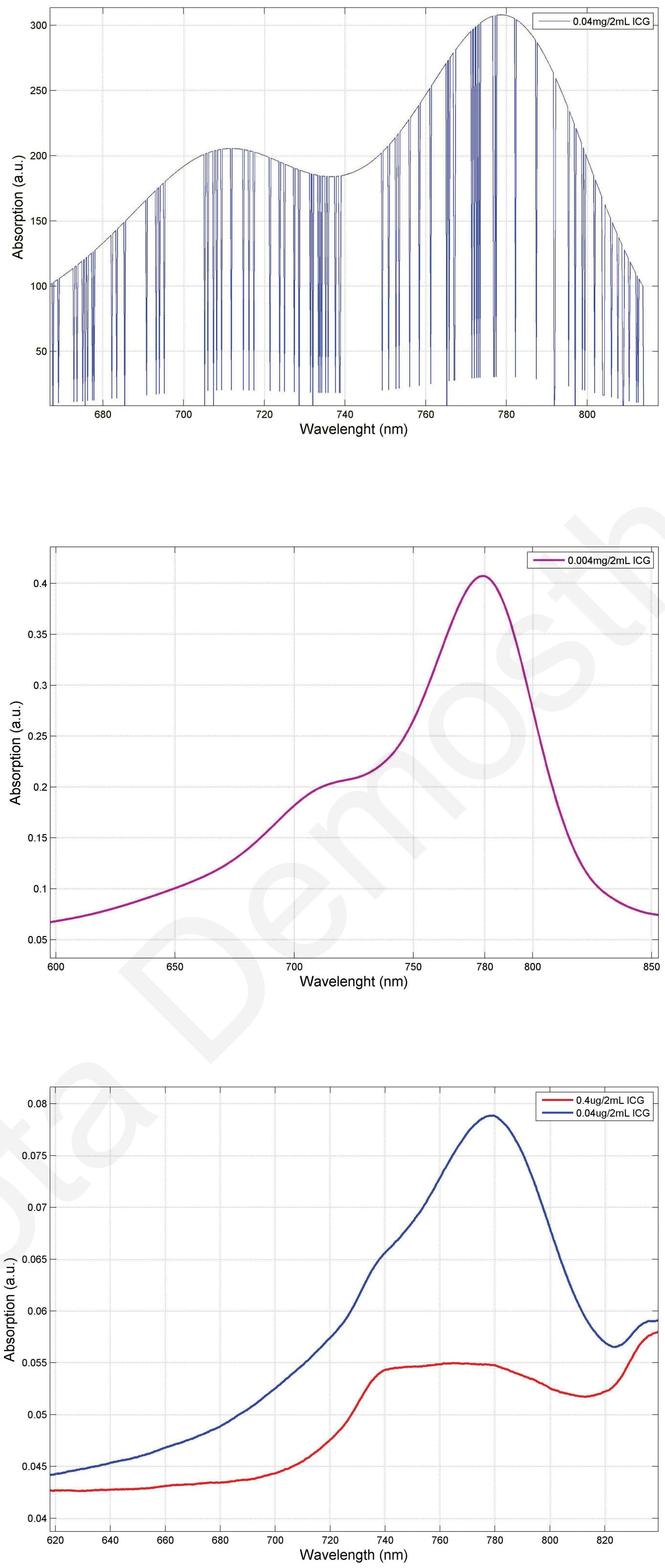

Figure 3.2: Experimental results of the absorption spectrums of ICG with concentrations at 25uM (0.04mg/2mL), 2.5uM (0.004mg/2mL), 250 nM (0.4ug/2mL) and 25nM (0.04ug/2mL) respectively.

The next thing that was investigated was the type of the excitation source. Specifically, an appropriate excitation light source for the screening capsule application should have:

1. Low bias current in order to reduce the total power consumption of the system; this is considering that the system would be powered by button cell batteries and would take approximately 8 hours for it to cover the entire G.I. tract.
2. High light output intensity; the higher the excitation light, the higher the emitted fluorescence and, thus, the measured photocurrent will be higher than the noise floor of the photodetector.
3. Narrow spectral bandwidth, which will make the task of filtering out the excitation light a little easier, whilst also avoiding the overlap of excitation wavelengths with emitted wavelengths, since the stoke shift of the ICG is very narrow at approximately 40nm.
4. Some tens of degrees beam divergence, in order to allow excitation of bigger areas of organic cells, resulting to a decrease of the number of light sources necessary for the system to screen cross sections of the intestine.
5. Fast rise/fall times to allow power cycling of the excitation source since the illumination source does not need to be on continually, as the capsule is not always on the move, reducing in that way its power consumption.

The choice of light source was narrowed down to Laser Emitting Diodes (LEDs) and Laser Diodes (LDs), for a number or reasons. They both have a narrowband spectrum, they are powerful enough to produce fluorescence signals with high intensity and are available in small sizes that are preferable for the capsule application where space is limited. Table 3.1 provide a brief comparison of LD and LED characteristics. Looking at Table 3.1, it can be seen that each source has it's pros and cons. LDs provide intense monochromatic light, which is ideal for fluorescence, as filtering of a narrow band excitation light from the emitted fluorescence is simpler. On the other hand, LEDs are not as intense and their light is not monochromatic. They can, however, operate at a much lower power, which is a very important consideration the fact that the capsule has to remain continuously operational for approximately 8 hours. In addition, LED light has higher beam divergence, which makes the design of the device easier since the distance from the laser to the tissue will be so small and will be difficult to cover a large area from each single light source. However, the beam divergence of the LD can easily be addressed with a microlense.

Table 3.1: Comparison of the characteristics of LEDs and LDs

Issue	LEDs	LDs
Bias Current	50-150 mA	100-500 mA
Intensity Output	Low	High
Spectral Bandwidth	25-40 nm	2-5 nm
Beam Divergence	High	Low (parallel beam)
Rise/Fall time	3-20 ns	0.5-2ns
Cost	Low	Medium

The next step was to test experimentally the excitation results that both light sources can provide. The goal of those experiments was to observe the fluorescence emission spectrum of ICG at different concentrations. For such an experiment an experimental set-up similar to fluorescence spectrometer was needed (Chapter 2, Section 2.4), with an excitation light source (LED or LD), several lenses, a long pass filter, a monochromator, ICG samples of different concentrations and an Si calibrated photodiode at the exit slit of the monocromaitor for the measurement of fluorescence intensity at different wavelengths. The experimental set-up is shown in figure 3.3. A LED (LED780-03AU) with emission maximum at 780 nm was used and placed perpendicular to the monochromaitor entrance slit. The perpendicular arrangement and the long pass filter with cut-off at 800 nm minimise the probability of any excitation light from directly reaching the photodiode.

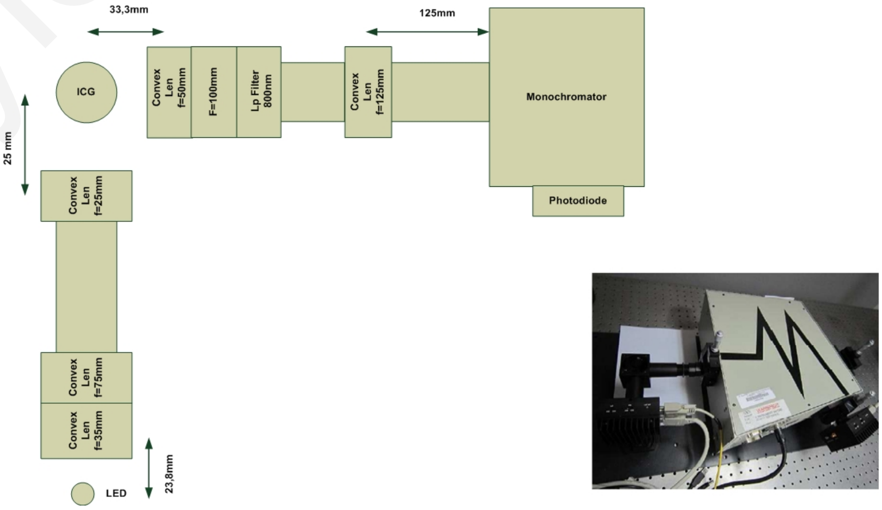

Figure 3.3: Experimental set-up for the observation of ICG emission spectrum

Based on the theoretical background, an emission fluorescence maximum at around 810-820 nm was expected, although the result in figure 3.4 shows the maximum at 800 nm. The observed spectrum is not actually the fluorescence spectrum, but the reflected high intensity excitation light, which still managed to get through the long pass filter and produce a photocurrent. That photocurrent has higher intensity than that produced by the fluorescence emission wavelengths, thus resulting in the masking of the ICG emission spectrum. The filter was unable to cut out the whole wide-range spectrum of the LED due to the overlap between the excitation spectrum and the selectivity of the filter, resulting in a spectrum maximum at the cut-off wavelength (figure 3.5). An interesting observation is that, at a higher ICG concentration (232 nM) an increased intensity at wavelengths greater than 800 nm is observed, corresponding to the fluorescence spectrum.

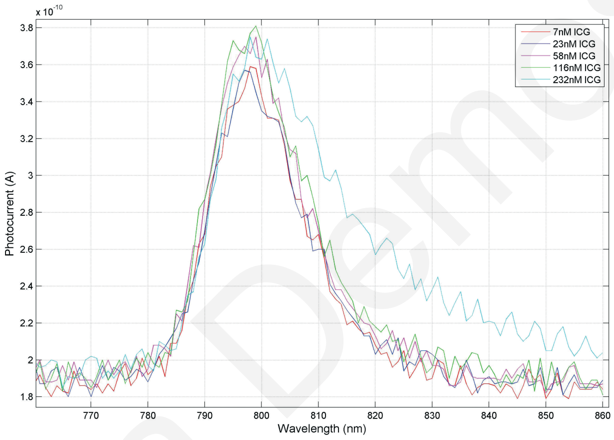

Figure 3.4: Emission results from the excitation of ICG with LED source of 780 nm.

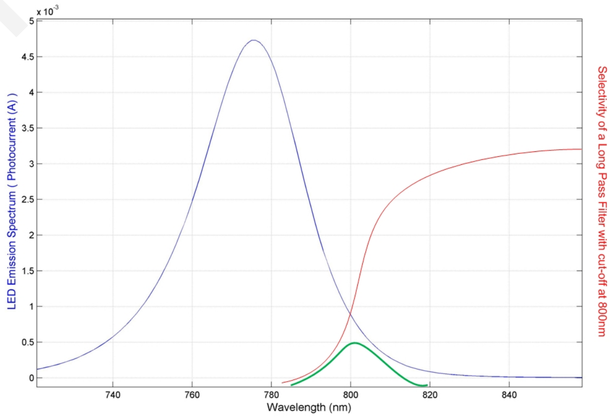

Figure 3.5: Overlap between the LED emission spectrum and the selectivity of the output long pass filter.

The experiment was repeated with a 780 nm LD (QL78J6SA) as the excitation source and without the peripherals confocal lenses, since light from a LD is already a parallel beam. The results are shown in figure 3.6. The peaks on the right hand side are the fluorescence spectra of ICG at different concentrations and the peaks in the left hand side are the reflected LD excitation spectrum after filtering. The LD has a very narrow spectral range that does not overlap with the selectivity of the filter. That characteristic makes the LD more suitable for the particular application, since the excitation light can be removed with filtering, resulting in more efficient detection of ICG fluorescence spectrum at different concentrations. Furthermore, the usage of a narrow band optical filter, needed in the case of a LED, is avoided.

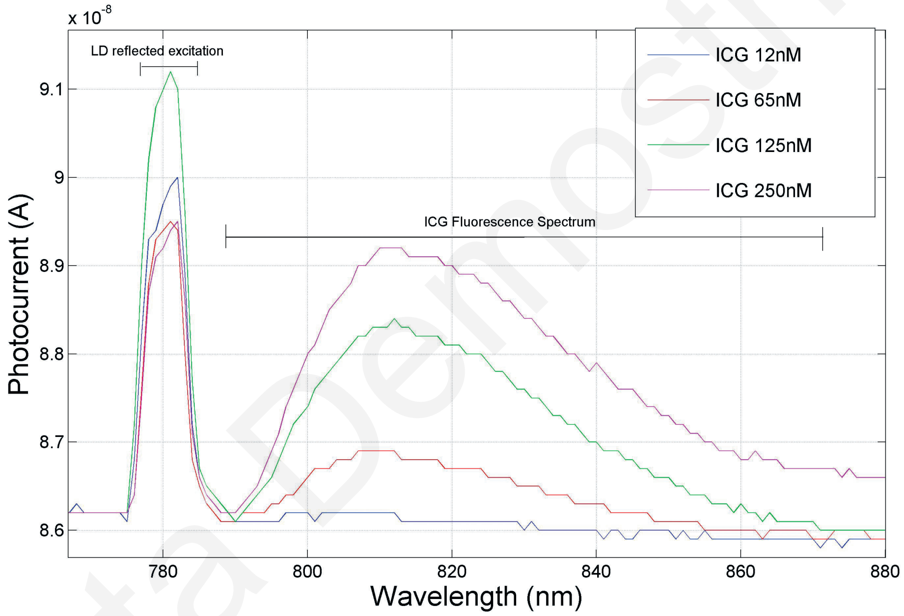

Figure 3.6: Emission results from the excitation of ICG dye with a monochromatic laser diode source of 780 nm wavelength. The ICG fluorescence spectra at different concentrations of the dye are clearly identifiable.

The experiment was repeated by replacing the ICG water-diluted samples with cryopreserved human tissues impregnated with ICG. The fluorescence spectrum of ICG was again observed, providing a clear discrimination of control tissue against ICG-occupied tissues. The results are shown in Figure 3.7.

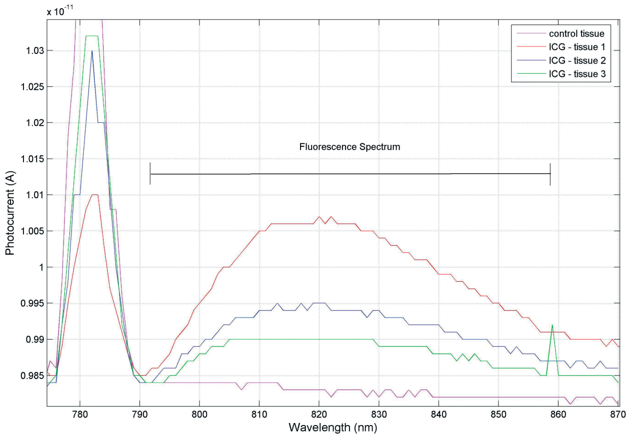

Figure 3.7: Fluorescence spectrum of cryopreserved tissues impregnated with ICG.

3.1.1 Constant Luminescence Excitation Source

As mentioned in section 2.3, the discrimination between two critical ICG concentrations at 19 nM and 225 nM, can provide information regarding the existence of cancer in the small intestine. However, the fluorescence intensity can easily change due to the variation of the optical power of the excitation source, thus it is necessary that the laser diode and its driver to provide constant luminescence during the excitation process. If the excitation source power is not constant, this may give rise to a false positive. Luminous intensity and emission wavelength of a LD depend on its forward current. Therefore, a LD system requires a constant current to maintain color integrity and to provide the desired luminosity. Furthermore, by using pulse width modulation (PWM), the average current in the LD can be regulated by creating changes to the light intensity without changing the real LD current, i.e. without affecting the emitted color (Figure 3.8). In other words, with changes in flashing duty cycle the brightness of the LD changes, but the peak current level remains constant preventing wavelength shifting.

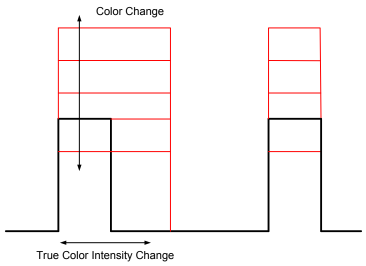

Figure 3.8: Luminous intensity changes of the laser diode with PWM without affecting emission wavelength.

In the presented application, the laser diode was driven with a constant current source in a flashing mode. A constant current driver was used to eliminate the effect of the power supply voltage variations, which can cause a change in the laser diode's luminous intensity and color. In addition, by power cycling the LD energy is saved and the LDs can safely output higher intensities. The drawback of the power cycling method is that, it may produce switching spikes at the beginning of the current pulses and, subsequently affect the luminous intensity of the LD. For that reason, measurements of fluorescence at the beginning of the excitation pulse should be avoided. Figure 3.9 represents the proposed constant current LD driver circuit in power cycling operation. A voltage reference IC (LM317M) was used to create a current reference topology through a constant voltage output at 1.2 V and a feedback resistor. A switching NMOS trench transistor driven by a field-programmable gate array (FPGA) or a complex programmable logic device (CPLD) controls the power cycling operation. Moreover, luminous intensity depends and is inversely proportional to LD-junction temperature that affects also the emitted color with a shift to higher wavelength as temperature increases. However, this is not as crucial for the specific application, since body's temperature variations throughout the day are not significant.

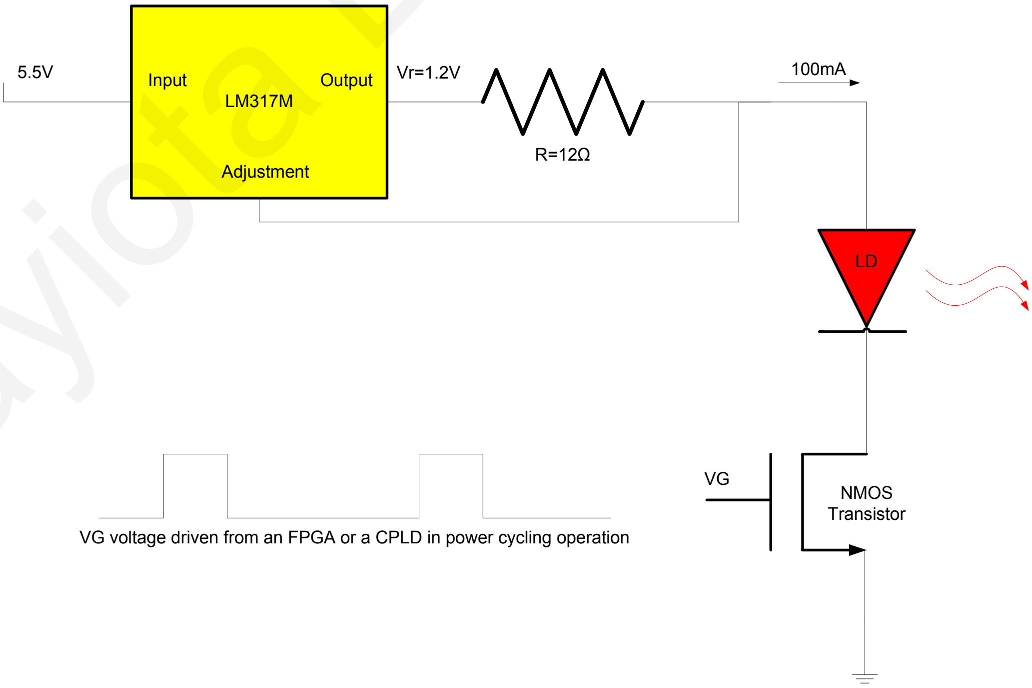

Figure 3.9: Constant current LD driver circuit, in power cycling operation, for constant luminescence.

The following mathematical analysis provides an estimation of the laser diode brightness variations due to variations in operating current, flashing duty cycle and ambient temperature. It was important to perform this analysis in order to gauge the viability of the capsule fluorometer, in view of the fact that the potentially low concentrations of the fluorophore lead to a relatively small dynamic signal range, and that any other sources of variation must be minimized and quantified. The optical power of a LD is given through the following expression (equation 3.1):

$$P_{optLD} = DC.n_s(I_{op} - I_{th}) \tag{3.1}$$

where n_s is the slope efficiency, I_{op} is the LD operating current, I_{th} is the minimum threshold current needed for the proper operation of the LD and DC is the flashing duty cycle [85]. Consequently, LD optical power can change after variations in the operating current, slope efficiency, threshold current and duty cycle. Therefore, optical power variations are estimated from the following differential equation (3.2):

$$dP_{optLD} = \frac{dP_{optLD}}{dI_{op}}.dI_{op} + \frac{dP_{optLD}}{dI_{th}}.dI_{th} + \frac{dP_{optLD}}{dn_s}.dn_s + \frac{dP_{optLD}}{dDC}.dDC \tag{3.2}$$

Otherwise:

$$dP_{optLD} = \frac{\partial P_{optLD}}{\partial I_{op}}_{DC,T_j}.dI_{op} + \frac{\partial P_{optLD}}{\partial T_j}_{I_{op},DC}.dT_j + \frac{\partial P_{optLD}}{\partial DC}_{I_{op},T_j}.dDC \tag{3.3}$$

n_s and I_{th} are dependent on temperature variations and can be obtained from equations 3.4 and 3.5 respectively. h is Planck's constant, c is the velocity of light in vacuum , e is electron's coulomb, n_d is the external differential quantum efficiency of LD, λ is the emitted wavelength (which depends on the LD junction temperature), I_{th} and I_0 are the threshold currents at absolute junction temperature T_j and at 0 K respectively and T_o is the characteristic temperature (which characterizes the temperature dependence of the threshold current of a laser diode).

$$n_s = \frac{h.c}{e.\lambda(T_j)}.n_d = 1.25\frac{n_d}{\lambda[um]} \tag{3.4}$$

$$I_{th} = I_o.e^{\frac{T_j[K]}{T_o[K]}} \tag{3.5}$$

Equations of the partial derivatives are given below :

$$\left.\frac{\partial P_{optLD}}{\partial I_{op}}\right._{DC,T_j} = DC.n_s = DC.\left(1.25\frac{n_d}{\lambda}\right) \tag{3.6}$$

$$\left.\frac{\partial P_{optLD}}{\partial DC}\right._{I_{op},T_j} = n_s.(I_{op} - I_{th}) = \left(1.25\frac{n_d}{\lambda}\right).(I_{op} - I_{th}) \tag{3.7}$$

$$\left.\frac{\partial P_{optLD}}{\partial T_j}\right._{I_{op},DC} = \left.\frac{\partial P_{optLD}}{\partial n_s}\right._{I_{op},I_{th},DC}.\frac{dn_s}{d\lambda}.\frac{d\lambda}{dT_j} + \left.\frac{\partial P_{optLD}}{\partial I_{th}}\right._{I_{op},n_s,DC}.\frac{dI_{th}}{dT_j} \tag{3.8}$$

$$= (DC.(I_{op} - I_{th})).\left(-1.25\frac{n_d}{\lambda^2}\right).\frac{d\lambda}{dT_j} + \left(-DC.\left(1.25\frac{n_d}{\lambda}\right)\right).\left(\frac{I_{th}}{T_o}\right) \tag{3.9}$$

In equation 3.9 the temperature coefficient of the peak wavelength of the laser can be obtained from the bandgap energy E_g of the laser medium [33]:

$$\frac{d\lambda}{dT_j} = -\left(\frac{h.c}{E_g^2}\right).\frac{dE_g}{dT_j} \tag{3.10}$$

The temperature dependence of the semiconductor bandgap energy is given through Varshni relation [72] (equation 3.11), where a and β are fitting parameters characteristic of a given material and $E_g(0)$ is the bandgap energy at a temperature of 0 K.

$$E_g(T_j) = E_g(0) - \frac{a.T_j^2}{T_j + \beta} \tag{3.11}$$

Thus, the equation 3.10 then becomes:

$$\frac{d\lambda}{dT_j} = \left(\frac{h.c}{E_g^2}\right).\left(\frac{2.a.T_j(T_j + \beta) - a.T_j^2}{(T_j + \beta)^2}\right) \tag{3.12}$$

Moreover, considering the current source topology in Figure 3.8, the LD operating current is equal to the reference voltage, V_r=1.2V, divided by the feedback resistor R (equation 3.13), thus any variations of the operating current are related to the variations of the reference voltage and the resistor value with ambient-body temperature changes. Equation 3.14 calculates the variations of the operating current, based on the assumption that reference voltage variations are negligible with temperature change anticipated inside the body.

$$I_{op} = \frac{1.2V}{R} \tag{3.13}$$

$$dI_{op} = \frac{dI_{op}}{dR} . \frac{dR}{dT_{amb}} .dT_{amb} = -\frac{1.2}{R^2} . \frac{dR}{dT_{amb}} .dT_{amb} \tag{3.14}$$

In addition, duty cycle in power cycling operation is a function of the switching frequency f_{sw} of the NMOS transistor, while switching frequency is a fraction of a crystal oscillator frequency f_{osc}, which further depends on ambient-body temperature T_{amb}. Equations 3.15 - 3.17 show these dependencies:

$$DC = t_p . f_{sw} \tag{3.15}$$

$$f_{sw} = \frac{f_{osc}(T_{amb})}{m} \tag{3.16}$$

$$f_{osc} = f_o(1 + b(T_{amb} - T_r)^2) \tag{3.17}$$

where t_p is LD pulse duration, m is the diviation number of crystal oscillation frequency, f_o is the crystal frequency at room temperature $T_r = 25\,^{\circ}\mathrm{C}$ and $b[\frac{ppm}{c^{o2}}]$ is the temperature coefficient of the crystal. Thus, small changes in duty cycle are given by equation 3.18:

$$dDC = \frac{dDC}{df_{sw}} . \frac{df_{sw}}{df_{osc}} . \frac{df_{osc}}{dT_{amb}} .dT_{amb} = t_p . \frac{1}{m} .2 f_o b(T_{amb} - T_r).dT_{amb} \tag{3.18}$$

The final step was to estimate LD optical power variations based on the above relations and actual values of the parameters. The excitation source used for the capsule fluorometer was an AlGaAs infrared laser diode with peak wavelength at 785 nm, output intensity around 100 mW and a relatively small package of 3.3 mm diameter. Table 3.2 shows all the parameters that are related to the AlGaAs infrared laser diode (ADL-78901SX), the crystal oscillator (ASDK 32.768 KHz) and the feedback resistor of the current source topology.

Table 3.2: Parameters values of several components of the capsule system

Parameter	Equation	Value
I_{op}	$I_{op}=\frac{1.2V}{12\Omega}$	100 mA
λ	-	0.785 um
I_{th}	-	25 mA
n_d	-	1.1 mW/mA
t_p	-	1 ms
f_{sw}	-	1 Hz
DC	DC=$t_p.f_{sw}$=1 ms.1 Hz	10^{-3}
T_o	-	55 K
$\frac{d\lambda}{dT_j}$	-	$2.5 * 10^{-4}$um/K
f_o	-	32.768 KHz
m	$f_{sw}=\frac{f_o}{m} \Rightarrow 1Hz = \frac{32.768KHz}{m}$	32768
b	-	-0.04 $ppm/°C^2$
$\frac{dR}{dT_{amb}}$	-	100 $ppm/°C$
T_{amb}	T_{amb}= body temperature	37.45 °C

The substitution of the parameters to the equations gives the following results:

$$\left.\frac{\partial P_{optLD}}{\partial I_{op}}\right|_{DC,T_j} .dI_{op} =1.75 * 10^{-3}[mW/mA] * (-10 * 10^{-3})[mA/K].dT_{amb} \\ = -0.0175 * 10^{-3}[mW/K].dT_{amb} \tag{3.19}$$

$$\left.\frac{\partial P_{optLD}}{\partial DC}\right|_{I_{op},T_j} .dDC =131.37[mW] * (-1 * 10^{-3})[1/K].dT_{amb} \\ = -131.37 * 10^{-3}[mW/K].dT_{amb} \tag{3.20}$$

$$\left.\frac{\partial P_{optLD}}{\partial T_j}\right|_{I_{op},DC} .dT_j = -0.84 * 10^{-3}[mW/K].dT_{amb} \\ for T_j = T_{amb} \tag{3.21}$$

Finally, assuming that the capsule is used for cancer screening between the hours of 11 a.m. and 9 p.m., where body temperature changes, dT_{amb}, are around ±0.11°C (Figure 3.10), then the LD optical power variation is approximately ±0.015mW (based on equation 3.22).

$$\begin{aligned} dP_{optLD} =& \frac{\partial P_{optLD}}{\partial I_{op}}_{DC,T_j}.dI_{op} + \frac{\partial P_{optLD}}{\partial T_j}_{I_{op},DC}.dT_j + \frac{\partial P_{optLD}}{\partial DC}_{I_{op},T_j}.dDC \\ &= (-0.0175 * 10^{-3}).dT_{amb} + (-131.37 * 10^{-3}).dT_{amb} + (-0.84 * 10^{-3}).dT_{amb} \\ &= \pm 0.015mW \end{aligned} \tag{3.22}$$

Considering that the photocurrent produced from LD radiation is around $10^{-3}A$ (see Figure 3.5) and ICG fluorescence is around $10^{-9}A$ (see Figure 3.6), then it can be assumed that excitation light intensity is 10^6 stronger than fluorescence. Therefore, LD intensity variation of $\pm 0.015mW$ can cause fluorescence variation of around $\pm 0.015nW$, thus ICG concentrations can still be detectable even after such variations in their fluorescence intensity.

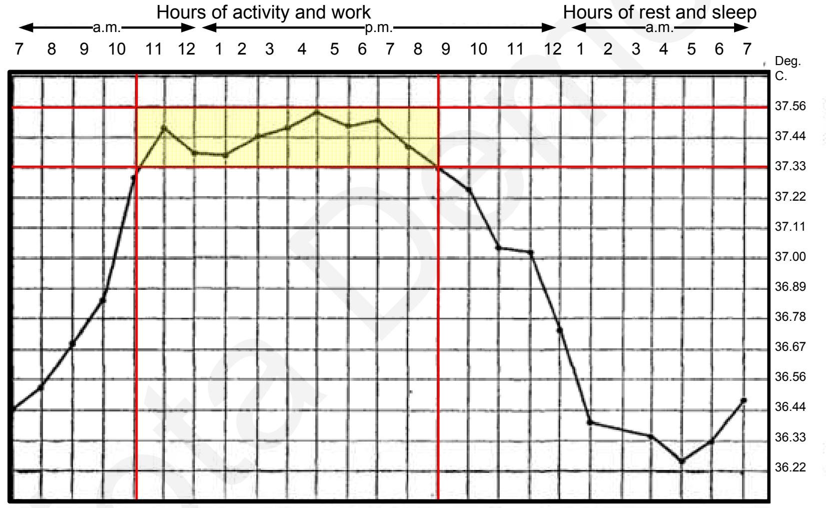

Figure 3.10: Humans body temperature variations during daily activity [5].

3.1.2 Intestine Tissue Maximum Permissible Laser-Exposure

The gastrointestinal track will be exposed to near infrared radiation during a cancer screening procedure, thus an investigation of the maximum permissible exposure (MPE) of intestine tissue to laser radiation is necessary. Optical radiation is usually absorbed in a thin layer of tissue, causing thermal heating and heating-related injuries to the cells. For that reason there is a threshold value, a maximum exposure level of radiation energy, below which no risk exists. In order to estimate the MPE for intestine tissue we need to consider, first, that intestine tissue falls between sensitive and hard tissue. Thus, the MPE of intestine tissue can be estimated as the average value of the MPE for eye (sensitive tissue) and skin (hard tissue); both these values can be obtained from the exposure limits of the ANSI Z-136.1 safety standard [71].

Eye and skin injury thresholds vary considerably with radiation wavelength. Figure 3.11 shows the exposure limits for direct ocular exposures and skin exposure from a laser beam in the visible and near infrared radiation range. Yellow boxes mark the MPE which is related to the presented application, since ICG-tissue excitation pulses have a duration of some milliseconds in a period of 1 second and a wavelength of 785 nm.

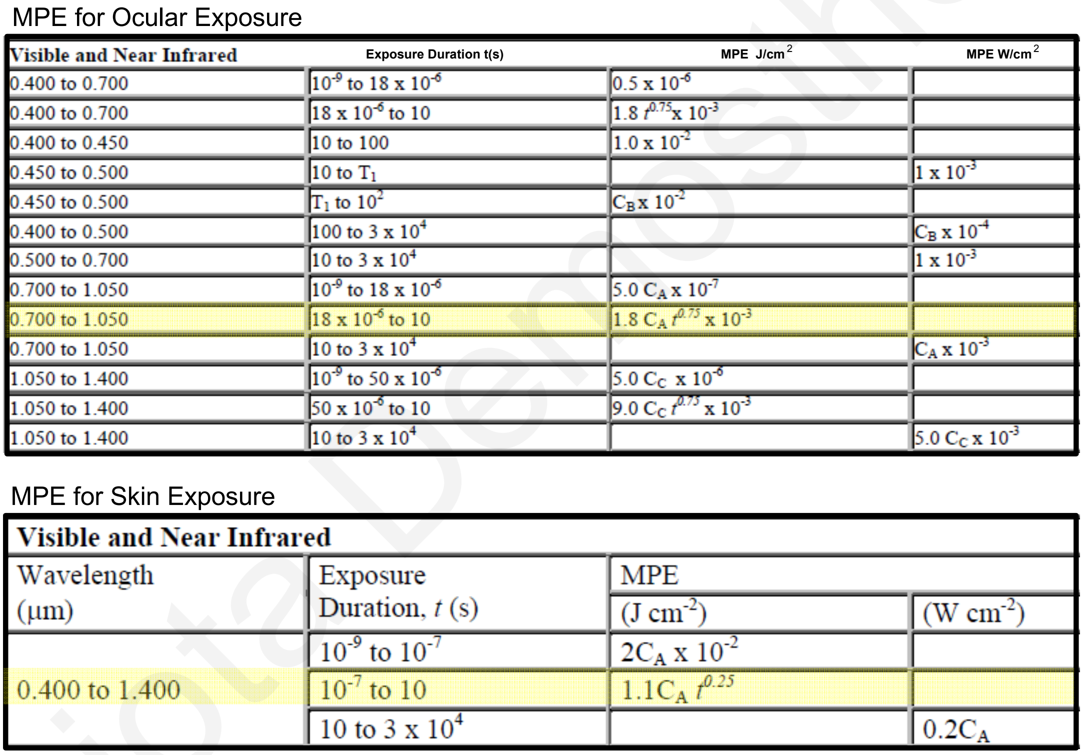

MPE for Ocular Exposure

Visible and Near Infrared	Exposure Duration t(s)	MPE J/cm^2	MPE W/cm^2
0.400 to 0.700	10^{-9} to 18×10^{-6}	0.5×10^{-6}	
0.400 to 0.700	18×10^{-6} to 10	$1.8\, t^{0.75} \times 10^{-3}$	
0.400 to 0.450	10 to 100	1.0×10^{-2}	
0.450 to 0.500	10 to T_1		1×10^{-3}
0.450 to 0.500	T_1 to 10^2	$C_B \times 10^{-2}$	
0.400 to 0.500	100 to 3×10^4		$C_B \times 10^{-4}$
0.500 to 0.700	10 to 3×10^4		1×10^{-3}
0.700 to 1.050	10^{-9} to 18×10^{-6}	$5.0\, C_A \times 10^{-7}$	
0.700 to 1.050	18×10^{-6} to 10	$1.8\, C_A\, t^{0.75} \times 10^{-3}$	
0.700 to 1.050	10 to 3×10^4		$C_A \times 10^{-3}$
1.050 to 1.400	10^{-9} to 50×10^{-6}	$5.0\, C_C \times 10^{-6}$	
1.050 to 1.400	50×10^{-6} to 10	$9.0\, C_C\, t^{0.75} \times 10^{-3}$	
1.050 to 1.400	10 to 3×10^4		$5.0\, C_C \times 10^{-3}$

MPE for Skin Exposure

Visible and Near Infrared			
Wavelength (µm)	Exposure Duration, *t* (s)	MPE	
		(J cm^{-2})	(W cm^{-2})
0.400 to 1.400	10^{-9} to 10^{-7}	$2C_A \times 10^{-2}$	
	10^{-7} to 10	$1.1C_A\, t^{0.25}$	
	10 to 3×10^4		$0.2C_A$

Figure 3.11: Maximum permissible laser exposure for direct ocular and skin exposure [71].

Therefore, the MPE for intestine tissue can be considered as the average of the two values:

$$MPE_{intestine-tissue} = \frac{1.8C_A.t^{0.75}.10^{-3} + 1.1C_A.t^{0.25}}{2} \tag{3.23}$$

where $C_A = 10^{(0.002(\lambda - 700nm))}$ is a correction factor for wavelengths between 700 nm and 1050 nm.

3.2 Fluorescence Detector Selection

As previously mentioned, fluorescence intensity is relatively weak compared to the excitation light intensity, thus for an efficient detection of different levels of ICG emitted light, a sensitive photodetector with low noise and low dark current is necessary. The choice of the detector type was between photoresistor, photodiode, phototransistor and avalanche photodiode [25], all of which have a small size appropriate for the limited-space capsule application. In the next section various options that were considered are described and evaluated in terms of suitability for this application.

3.2.1 Photoresistors

A photoresistor (or photocell) is basically a resistor whose resistive value changes depending on how much light shines onto its active area. Specifically, its resistance decreases with increasing incident light intensity. A typical structure for a photoresistor uses an active semiconductor layer that is deposited on an insulating substrate. The semiconductor is normally lightly doped to reach the required level of conductivity (Figure 3.12a). Contacts are then placed either side of the exposed area. In many instances the area between the contacts is in the form of a zig zag pattern to maximise the exposed area (Figure 3.12b). Photocells are very low cost, and come in many sizes and specifications; however, they have low accuracy and slow response, taking tens or hundreds of milliseconds to respond to sudden changes in the light level. Each photocell sensor will act a little differently than the other, even if they are from the same batch. The variations are of a magnitude of 50 per cent or higher. For these reasons, they should not be used for determining precise light levels.

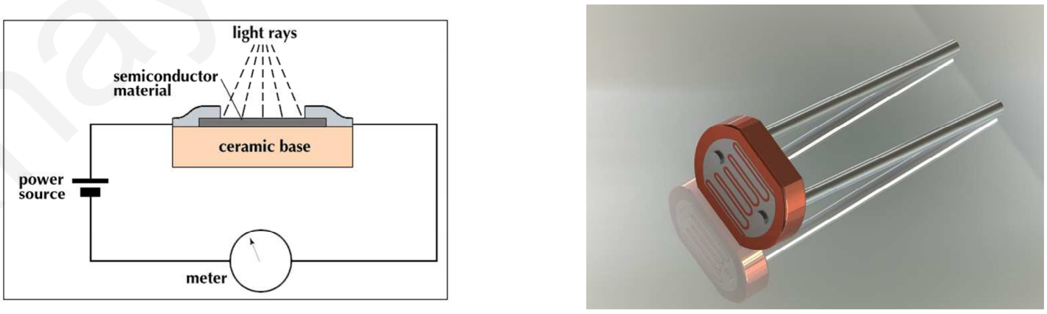

(a) (b)

Figure 3.12: a) Layer structure of a photoresistor , b) Photoresistor sensor.

3.2.2 Photodiodes and Avalanche Photodiodes

Photodiodes are semiconductor light sensors that generate a current or voltage when the active area of the semiconductor is illuminated by light. They are sensors used to detect the intensity of light. When a semiconductor is illuminated by light whose energy is greater than the semiconductor band-gap energy (E_g) the light is absorbed and electron-hole pairs are generated creating a photocurrent. Specifically, at absolute zero temperature the valence band is completely filled with electrons and the conduction band is empty. As the temperature increases, the electrons acquire thermal energy and move from the valence band to the conduction band, leaving holes in the valence band. The resulting electrons in the conduction band and holes in the valence band are free to conduct current. Therefore, a diffusion current is generated due to differences in electron and hole concentration at the P-type and N-type regions. Electrons from the N-type region diffuse to the P-type region and holes from the P-type to the N-type region creating a built-in voltage across the P-N junction and a region with no free carriers, called the depletion region. The built-in voltage across the depletion region results in an electric field , which only exists within the depletion region and is maximum at the junction. Any applied reverse bias at the anode and cathode of the photodiode is added to the built-in voltage, resulting in a wider depletion region and a stronger electric field. Thus, light-induced electron-hole pairs in depletion region are separated by the electrical field, contributing to a drift photocurrent, which is proportional to the incident light (Figure 3.13).

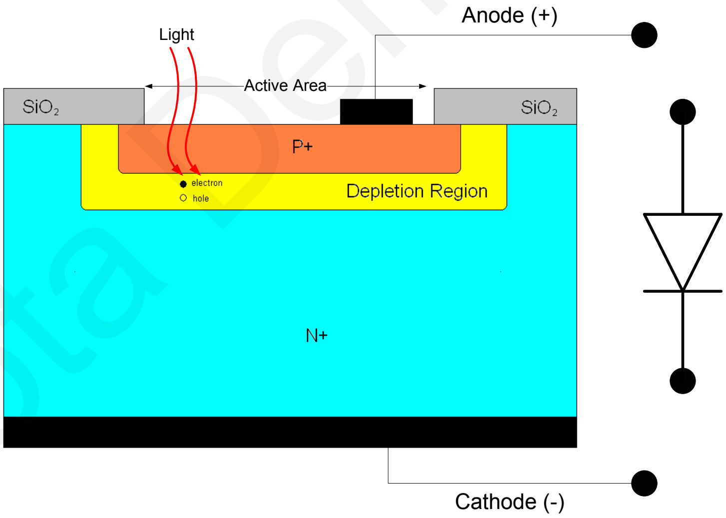

Figure 3.13: Layers structure of a photodiode.

With light absorption, the current-voltage characteristics of a photodiode change as shown in Figure 3.14, and the reverse current increases due to generation of the photocurrent I_{ph}. Depending on the reverse pn-junction bias voltage, the operation modes of a photodiode can be divided into photovoltaic (no reverse biased), photocontactive (reverse biased), and avalanche photodiode mode (reversed biased to breakdown voltage).

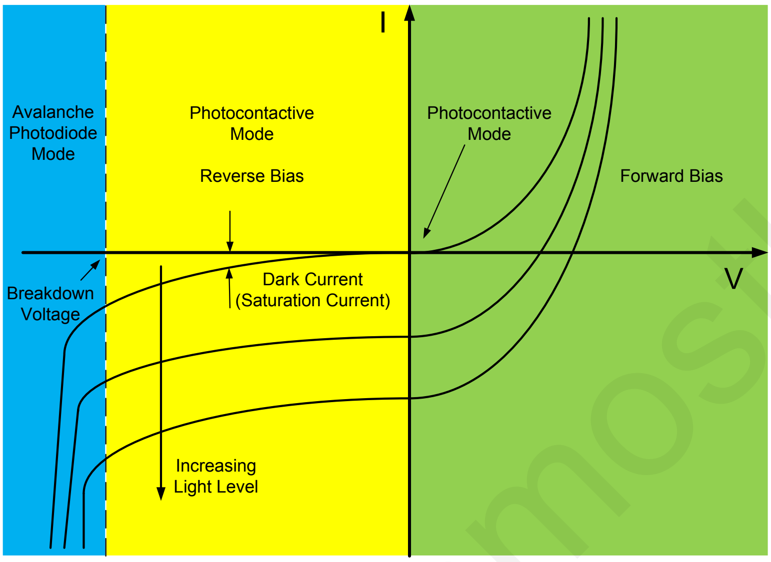

Figure 3.14: Current - Voltage characteristics of a photodiode with increasing level of incident light.

When a reverse bias is applied, a small reverse leakage current appears known as dark current, I_D, and flows even when the photodiode is in a dark environment. Dark current is temperature dependent and it approximately doubles its value for every 10°C increase in ambient temperature. Thus, the total measured current from a photodiode is equal to:

$$I_{total} = I_D + I_{ph} = I_{sat}.e^{\frac{e.V_A}{k.T}} + I_{ph} \tag{3.24}$$

where I_D is the dark current, I_{ph} is the induced photocurrent, I_{sat} is the reverse saturation current due to thermal generated carriers, V_A is the applied bias voltage, k is the Boltzmann Constant and T is the absolute temperature (273°K=0°C).

As the applied reverse bias increases, there is a sharp increase in the photodiode current. The applied reverse bias at this point is referred to as breakdown voltage (Figure 3.14). This is the maximum applied reverse bias, and the photodiode should operates below this voltage. On the other hand, the avalanche photodiode uses that functionality and operates in avalanche mode near the breakdown voltage. That makes the device more sensitive to very low intensity light, however the high reverse bias voltage, around 100 V - 200 V, is not practical.

A silicon photodiode can be represented by a current source in parallel with an ideal diode (Figure 3.15). The current source represents the current generated by the incident radiation, and the diode represents the p-n junction. In addition, a junction capacitance (C_j) and a shunt resistance (R_{SH}) are in parallel with the other components. A series resistance (R_S) is also connected in series with all components in this model.

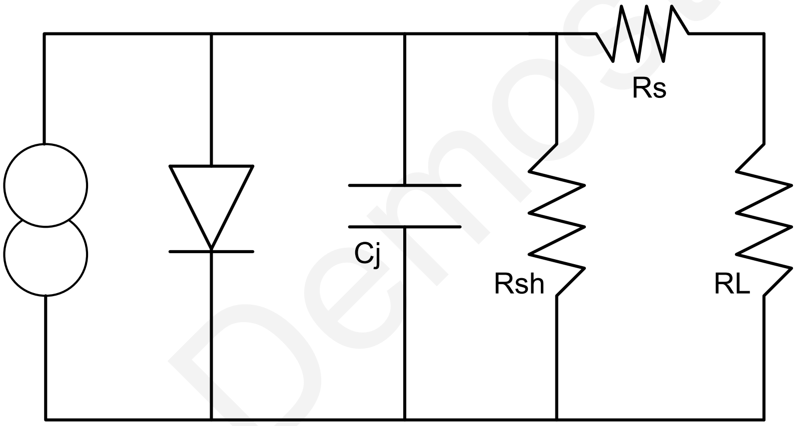

Figure 3.15: Photodiode's equivalent circuit.

Shunt resistance (R_{SH}), or dynamic junction resistance, is given by the slope of the current-voltage photodiode curve at zero voltage. It is temperature dependent, decreasing with increasing temperature. For best photodiode performance the highest shunt resistance is desired. The series resistance (R_S) of a photodiode arises from the resistance of the contacts and the resistance of the undepleted silicon. Ideally R_S should be very small. Finally, junction capacitance (C_j) is determined by the boundaries of the depletion region, which act as the plates of a parallel plate capacitor whose capacitance is directly proportional to the diffused area and inversely proportional to the width of the depletion region. It also depends on the reverse bias, since the depletion region increase with increasing reverse bias voltage.

Low noise is a desired characteristic of a photodetector, since noise current will limit the usefulness of the photodiode at very low light levels where the magnitude of the noise approachs that of the signal photocurrent. In a photodiode two sources of noise can be identified: shot noise and Johnson noise. Thermal, or Johnson noise is inversely related to the value of the shunt resistance of the photodiode and is caused by the thermal generation of carriers. This type of noise is the dominant current noise in the photovoltaic (unbiased) operation mode. On the other hand, shot noise is related to the statistical fluctuation of both the photocurrent and the dark current of the photodiode and it dominates when the photodiode is used in the photoconductive mode, where an external reverse bias is applied across the device causing an increase of dark current.

Photodiode light current is often causing linear over a wide range of light intensities with excellent linearity over 6 to 9 decades of light intensity. Consequently, photodiodes are often used in applications where absolute measurement of light intensity is required. The lower limit of the photocurrent linearity is determined by the noise current and the upper limit by the series resistance and the load resistance. Furthermore, the response time of a photodiode depends on the value of the applied voltage across the diode (since this has a major effect of the junction capacitance), and the load resistance.

Accordingly, a reverse bias can greatly improve the speed of response of the devices, due to increase in the depletion region width and, consequently, decrease in junction capacitance. Applying a reverse bias, however, will increase the dark and noise currents. On the contrary, photovoltaic mode of operation is preferred when a photodiode is used in low frequency applications, as well as ultra low light level applications, since noise current is lower. In photoconductive mode the dark current may approximately double for every 10 °C increase change in temperature, whilst in photovoltaic mode, shunt resistance may approximately double for every 6 °C decrease in temperature.

An important characteristic is the responsivity (R) or the sensitivity of a photodetector. The responsivity of a photodiode is a measure of the sensitivity to light and is defined as the ratio of the photocurrent to the incident light power (P) at a given wavelength:

$$R_\lambda = \frac{I_{ph}}{P}[A/W] \tag{3.25}$$

In other words, it is a measure of the effectiveness of the conversion of light power into electrical current. It varies with the wavelength of the incident light, as well as applied reverse bias and temperature.

Avalanche Photodiodes (APDs) have high sensitivity, high response speed and improved signal-to-noise ratio, since they utilize an internal gain avalanche mechanism. In particular, APDs operate in avalanche mode where a reverse bias near breakdown voltage (100 V - 200 V) is required. The high voltage biasing creates a strong electric field, that provides high kinetic energy to the light-induced electron-hole pairs, which then collide with atoms in the crystal lattice creating more electron–hole pairs, some of which cause further ionization. Compared to photodiodes, avalanche photodiodes can measure even lower light levels and are used in applications where high sensitivity is required. However, the very high reversed bias voltage needed for their operation, results in much higher dark current and, thus, resulting power consumption. Moreover, charge pumps are required, hence increasing power consumption and space. Also quenching circuits are needed to terminate the electron avalanche and to trigger the photocurrent processing in the subsequent circuits. In order for a regular photodiode to detect lower light levels, common practice involves increasing the gain in the operating circuit by increasing the feedback resistor value. This has the unwanted consequence of reducing the speed of response and increasing the thermal noise associated with the operating circuit. The effect of the thermal noise can be reduced by adding a parallel (to the feedback resistor) capacitor, which essentially lowers the phototransduction circuit's response time. Otherwise, it can be reduced in a later stage, through digital averaging techniques.

3.2.3 Phototransistor

A phototransistor can be viewed as a photodiode whose output photocurrent is fed into the base of a conventional BJT transistor. The PN junction is the collector-base diode of a bipolar transistor and the light-induced current effectively replaces the base current (Figure 3.16). The nature of the transistor itself is such that a change in base current can cause a significant increase in collector current. Thus, the base current from the incident photons is amplified by the gain of the transistor, resulting in current gains that range from hundreds to several thousands, providing higher sensitivity to the device. The phototransistor has a much lower level of noise when is compared to an avalanche photodiode, but the noise is higher compared to a photodiode, since dark current is also subject to the amplification. Furtheremore, unlike a photodiode, whose output is linear with respect to incident light over 7 to 9 decades of light intensity, the collector current of a phototransistor is linear for only 3 to 4 decades. Moreover the speed of response of a phototransistor is dominated almost totally by the capacitance of the collector-base junction and the value of the load resistance. These dominate due to the Miller Effect, which multiplies the value of the RC time constant by the current gain of the phototransistor. This leads to the general rule that for devices with the same active area, the higher the gain of the photodetector, the slower the response is.

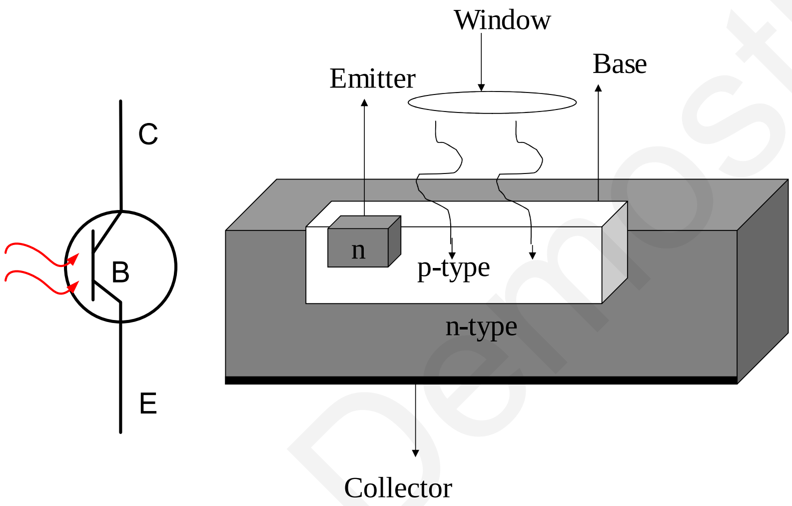

Figure 3.16: Phototransistor layer structure and electrical symbol

3.2.4 Conclusion on Photodetectors

Table 3.3 shows a brief summary of the main characteristics of the four candidate photodetectors, for the capsule system, as they described above. The advantageous properties of the devices are indicated in green, in contrast to the disadvantages, which are marked in red. Large photodiodes are shown to be the most appropriate fluorescence detectors for this application. This is mainly because, the low dark current in comparison to the phototransistors and the low bias voltage in comparison to avalanche photodiodes. Also, they do not need the extra charge pump and quenching circuitry, thus lower overall power consumption.

Table 3.3: Characteristics of different types of photodetectors

Parameters/Devices	Photoresistor	Photodiode	Phototransistor	APD detector
Responsivity (Sensitivity)	Highly variable	0.5-0.7 uA/uW	current gains from hundreds to several thousands	30-80 uA/uW (function of Vbias) Current gain around 30 to 1000
Sensitive in Temperature	Low	Low	Medium	High
Vbias	Around 5V	0V - 10V	0V - 10V	100V -200V near to breakdown voltage
Response Speed	Slow response at around 55ms	At around 6ns	At around 1-15us (C-B junction high capacitance)	High speed (strong electric field and low junction capacitance)
Dark Current	-	Low (compare to APD)	High (also subject of amplification)	Much higher because of high Vbias
Noise	High (thermal noise)	Low	Medium-High (higher dark current higher shot noise)	High (shot and excess noise)
SNR	Low	Medium	High	High
Output Linearity	Linear	Linear over 7 to 9 decades of light intensity	Linear over 3 to 4 decades of light intensity	Not linear output because of avalanche mechanism and the certain probability of ionization to occurs

3.3 Optically Transparent Capsule Housing materials

There are several materials for housing the fluoroscopic system, which are mainly approved for medical use. Those materials are Polyphenylsulfone, Polysulfone, Polyetherimide, Polymethyl methacrylate and Polycarbonate, all of which are plastics. Also, they are Soda-lime and Borosilicate, which belong to the glass category. The first three are unsuitable, as they are translucent, and have poor optical characteristics. Polycarbonate is also inappropriate, as it also has some potential biocompatibility problems. Choosing between plastic and glass, plastic is preferred as it is cheaper and can be easily formed into a complicated structure, that may have optical lenses and reflectors integrated to its body. Therefore, Polymethyl methacrylate, the well known Acrylic, was chosen as the housing material, which is often used as an alternative to glass option. Other characteristics of Acrylic are listed below [52]:

- It is transparent to IR light up to 2800 nm with a refractive index of 1.49. Index matching epoxy should have similar refractive index to prevent light reflections.
- It can be easily heat-formed without loss of optical clarity
- It is unaffected by aqueous solutions of most laboratory chemicals, cleaners, diluted inorganic acids and alkalis
- It is a strong and lightweight material with good impact strength higher than glass
- It has good degree of compatibility with human tissue and is biologically compatible.

3.4 Optics Optimal Structure

The optimal positioning of the excitation sources, the detectors and lenses can increase the overall detection sensitivity and efficiency of the capsule system by optimally screening the whole small intestine area. For that reason, two structures were considered as the most appropriate optics-position for the presented capsule application. Those structures are a) the side circular and b) the front circular positioning, shown in Figure 3.17.

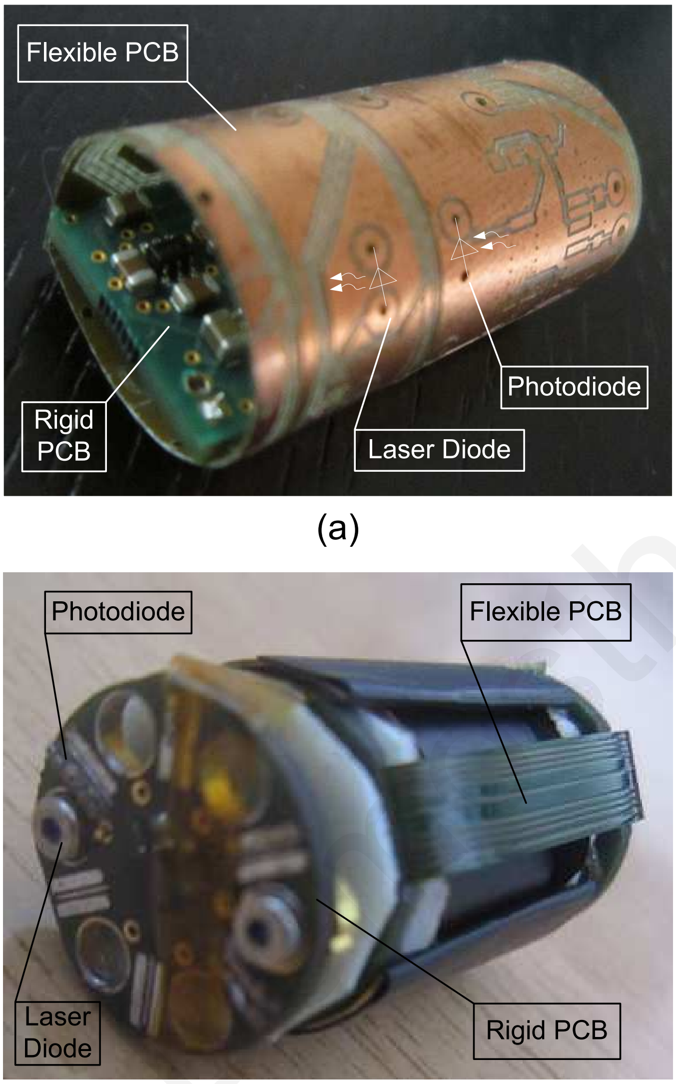

(a)

(b)

Figure 3.17: Optics a) side circular structure and b) front circular structure.

In both cases the excitation sources and the photodetectors are placed in a circular manner, covering in this way a cross section of the small intestine and allowing to the capsule fluorometer to perform an overall intestine screening. The spherical surfaces (lenses), which are responsible to diverge the excitation light to a total cross sectional area of the intestine, will be constructed on the acrylic capsule case. However, the actual implementation of the capsule housing with the embedded lenses is outside the scope of that research. The following sections provide a more detailed description of the two structures, as well as the necessary calculations related to the spherical surface characteristic parameters.

3.4.1 Side Circular Optics Structure

As Figure 3.17a shows, laser diodes and photodiodes are placed side by side in a circular manner around the capsule case side-walls. This structure, in combination with spherical surfaces for diverging the excitation light, allow the capsule to perform an efficient screening of an entire cross sectional area of the small intestine. Figure 3.18 shows the cross section of the Capsule - Intestine System, where the diameter of the capsule is 12 mm with an acrylic case of 2 mm thickness and a small intestine average value diameter of around 30 mm [3].

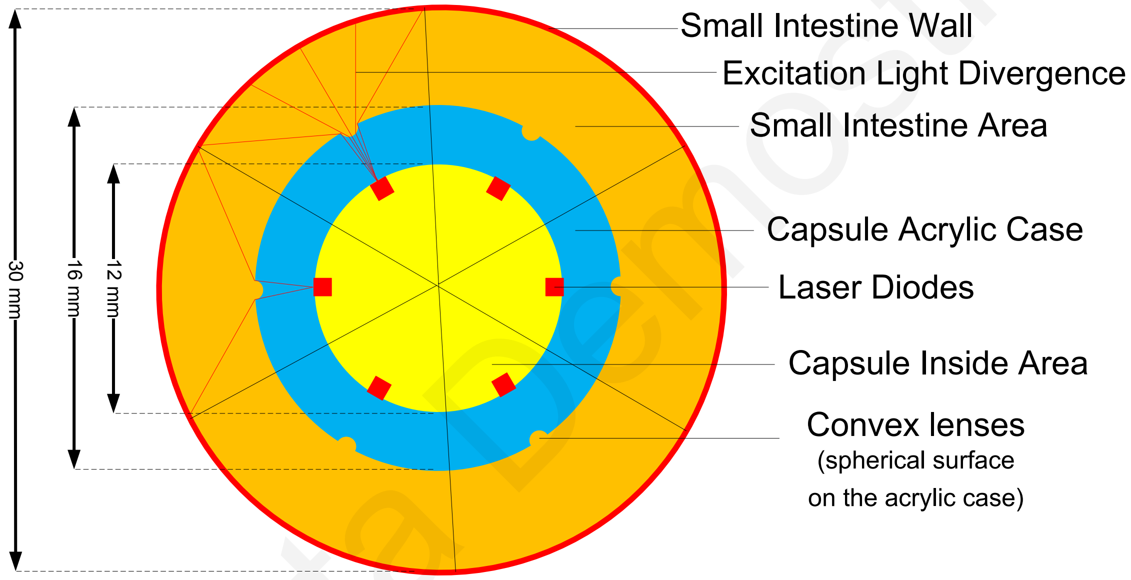

Figure 3.18: Capsule - Intestine System cross section of side circular optics structure.

Let us now consider the LD - Lens System and calculate the radius of curvature (R) of the spherical surface, such that the excitation light is refracted in a desirable angle illuminating in this way an arc-part of the intestine. With the assumption that the laser diode is attached to the capsule case walls with index matching epoxy, then the light ray from the LD is refracted at a single surface POQ that separates air and acrylic with a refractive index of 1 and 1.49 respectively (Figure 3.19). Furthermore, the divergence angle (U) of the laser beam is 8.5° based on the data sheet [4] of the device.

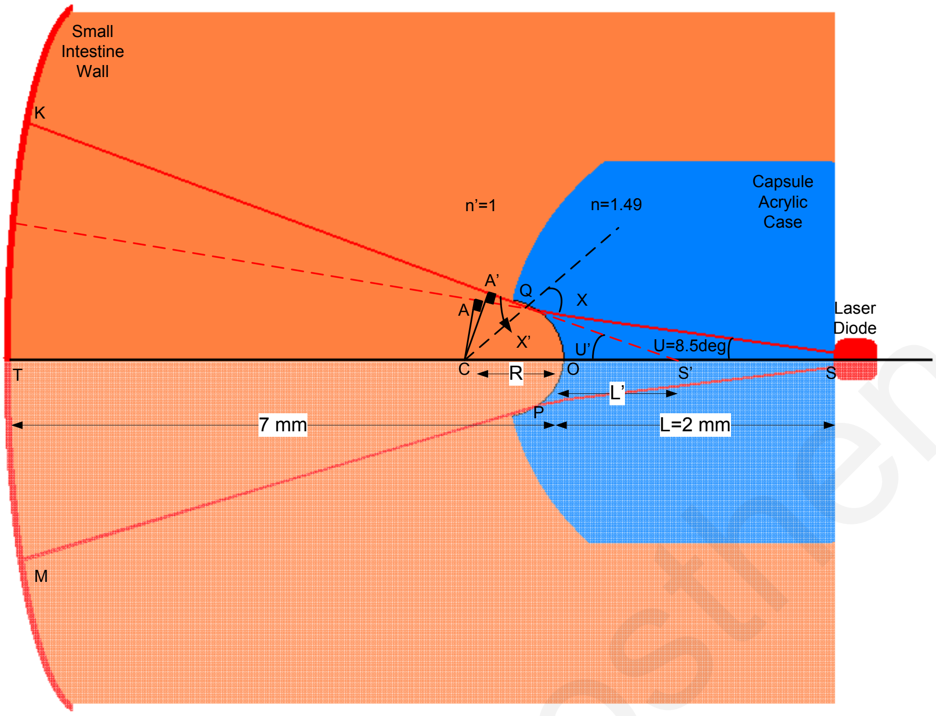

Figure 3.19: LD - Lens System. Refraction of laser beam ray at a spherical surface.

The following set of equations allows the calculation of the radius of curvature R of POQ surface [84]. From the right triangle S'A'C and SAC,

$$CA' = (L' + R)sinU' \tag{3.26}$$

$$CA = (L + R)sinU \tag{3.27}$$

and from the right triangle QA'C and QAC,

$$sinX' = \frac{CA'}{R} \tag{3.28}$$

$$sinX = \frac{CA}{R} \tag{3.29}$$

Applying Snell's law,

$$sinX' = \frac{n}{n'}sinX \tag{3.30}$$

Substituting Eqs. 3.28 and 3.29 into Eq. 3.30 then,

$$CA' = \frac{n}{n'}CA \tag{3.31}$$

Finally, the radius of curvature of the POQ surface is:

$$\begin{aligned} R =& \frac{CA'}{sinU'} - L' \\ =& \frac{\frac{n}{n'}CA}{sinU'} - L' \\ =& \frac{\frac{n}{n'}(L+R)sinU}{sinU'} - L' \end{aligned} \tag{3.32}$$

Therefore, the value of R can be calculated by assigning some values to the angle U′ and length L′ since all other parameters are known. The calculation of those parameters is given below.
The length of the arc $\widehat{KT}$ is 7.85 mm, derived from dividing the intestine perimeter by six,

$$P_{intestine} = 2\pi R_{intestine} = 30\pi = 94.25mm \tag{3.33}$$

$$\widehat{KTM} = 94.25/6 = 15.71mm \tag{3.34}$$

$$\widehat{KT} = 15.7/2 = 7.85mm \tag{3.35}$$

The length OQ can be approximately estimated through the tangent of angle U (eq. 3.36) or through the arc length of angle U (eq. 3.37). Since both equations give similar result, they consider valid for small distances.

$$OQ = tanU * L = tan(8.5) * 2 = 0.299mm \tag{3.36}$$

$$\widehat{OQ} = 2\pi L\frac{U}{360} = 2\pi 2\frac{8.5}{360} = 0.297mm \tag{3.37}$$

All the above, result to two equations (eq. 3.38 and 3.39) with U′ and L′ as unknown parameters. Solving those equations the missing parameters for equation 3.32 can be obtained (eq. 3.40).

$$\widehat{OQ} = 2\pi L'\frac{U'}{360} => 0.3 = 2\pi L'\frac{U'}{360} => L' = \frac{17.19}{U'} \tag{3.38}$$

$$\widehat{KT} = 2\pi(TO + L')\frac{U'}{360} => 7.85 = 2\pi(7 + L')\frac{U'}{360} \tag{3.39}$$

$$7.85 = 2\pi(7 + \frac{34.38}{U'})\frac{U'}{360} => U' = 61.80°, L' = 0.28mm \tag{3.40}$$

Therefore, from eq. 3.32, the radius of curvature of the POQ surface is approximately 0.29 mm (eq. 3.41)

$$\begin{aligned} R &= \frac{\frac{n}{n'}(L+R)sinU}{sinU'} - L' \\ &= \frac{\frac{n}{n'}LsinU - L'sinU'}{sinU' - \frac{n}{n'}sinU} = \frac{0.44 - 0.25}{0.88 - 0.22} \\ &= 0.29mm \end{aligned} \tag{3.41}$$

3.4.2 Front Circular Optics Structure

The front circular optics structure is shown in Figure 3.17b, where the six sets of alternating laser diodes and photodiodes are placed concentrically at the end of the capsule. They are positioned as such, so as to scan the intestinal walls whilst being pushed along by the peristaltic movement (Figure 3.20). This is important, since at this time, the intestine is pressed up closely to the capsule walls, thus keeping a fairly constant distance between the walls and the optics.

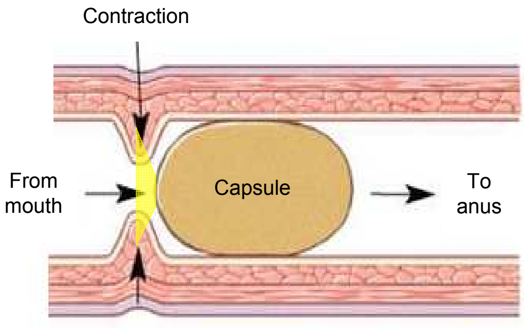

Figure 3.20: Peristaltic movements of small intestine.

Figure 3.21 shows the side and front view of the structure. Some useful dimensions are also indicated for the calculation of radius of curvature of the spherical surface. The calculation of R in front circular optics structure, uses the same equations as in the side circular structure, differing only by some parameter values. Specifically, KTM length is now 4.7 mm and TO distance is around 5 mm. Thus, from the equations 3.42 to 3.45, the radius of curvature of the POQ surface is approximately 0.83 mm.

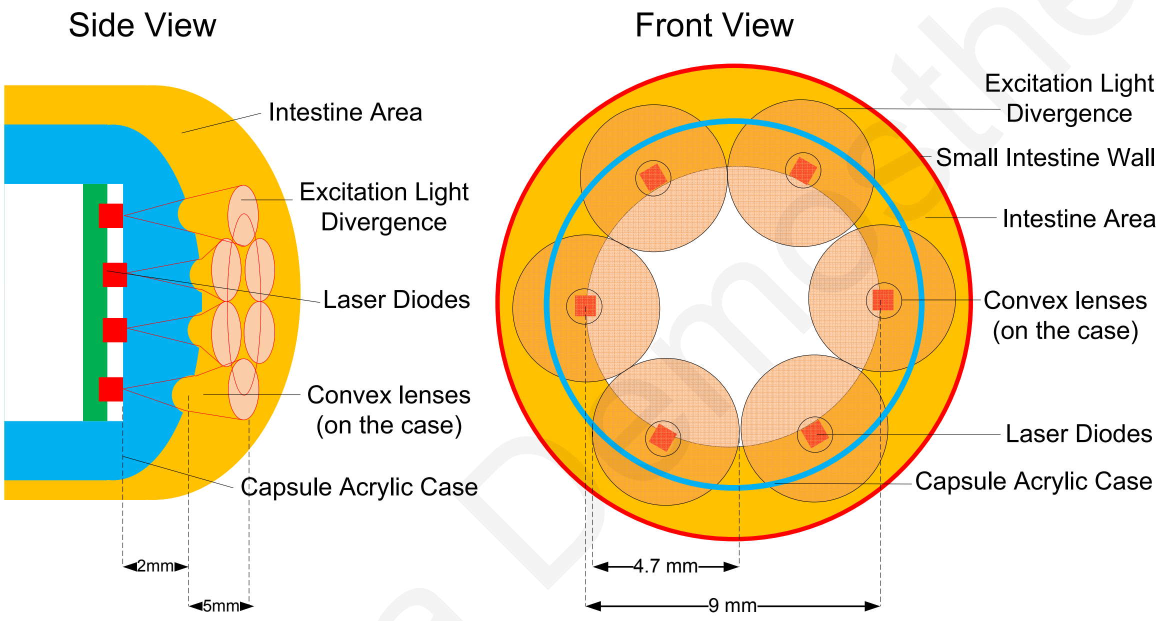

Figure 3.21: Capsule - Intestine System's front and side view of the front circular optics structure

$$\widehat{OQ} = 2\pi L'\frac{U'}{360} => 0.3 = 2\pi L'\frac{U'}{360} => L' = \frac{17.19}{U'} \tag{3.42}$$

$$\widehat{KT} = 2\pi(TO + L')\frac{U'}{360} => 2.35 = 2\pi(5 + L')\frac{U'}{360} \tag{3.43}$$

$$2.35 = 2\pi(5 + \frac{17.19}{U'})\frac{U'}{360} => U' = 23.49^\circ, L' = 0.73mm \tag{3.44}$$

$$
\begin{aligned}
R &= \frac{\frac{n}{n'}(L+R)sinU}{sinU'} - L' \\
&= \frac{\frac{n}{n'}LsinU - L'sinU'}{sinU' - \frac{n}{n'}sinU} = \frac{0.44 - 0.29}{0.40 - 0.22} \qquad (3.45) \\
&= 0.83mm
\end{aligned}
$$

3.5 Air Pockets as Light Diverging Lenses

An air bubble, in the index matching epoxy, in front of each LD, can be used as a divergent lens, to scan a larger segment of the intestine (Figure 3.22a) [106]. Each ray, in a collimated laser beam of infinitesimal thickness, that impinges on an air bubble, gives rise to a group of rays by reflection and refraction , as is shown in Figure 3.22b. The theory on an air bubble acting as a micro lens, has been thoroughly analysed by Davis [18], where he showed that the energy of the collimated beam of incidence upon an air bubble in water (with a large diameter in comparison to the wavelength of the incident light) is scattered in the general forward direction, ranging in angle from 0° to 82.8°. The author highlights that the surfaces 1 and 2 of rays incidence, contribute the most to the intensity of the scattered light within this angular range. Thus, we expect a similar behaviour from light interacting with bubbles found in the index matching epoxy ($n_{water} = 1.333$, $n_{epoxy} = 1.52$, $n_{acrylic} = 1.49$).

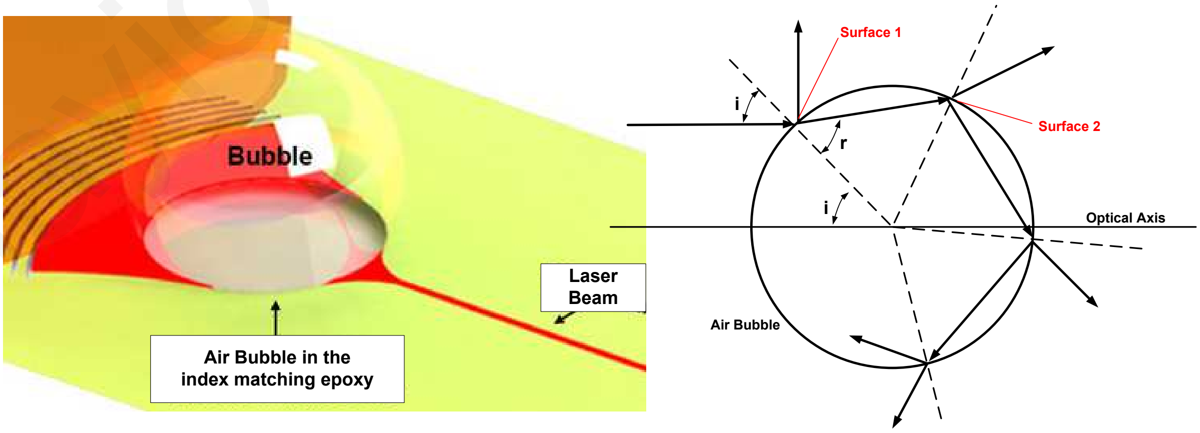

(a) (b)

Figure 3.22: Laser Diverging Bubble Lens: a) Air bubble in the index matching epoxy, b) Reflection and refraction of components of an incident ray.

An experiment was performed to verify the validity of the principle to the capsule application. During the attachment of the pcb to the capsule case, which was filled with index matching epoxy, an air bubble was trapped in front of each LD (Figure 3.23a). The cylindrical shape of the laser diode allowed the formation of such a micro-lens. The experiment uses a calibrated photodiode and Keithley 4200SCS for the measurement of the LD's optical intensity at an angular range from 0° to ±90° and at a radius distance of 1 cm (Figure 3.23b).

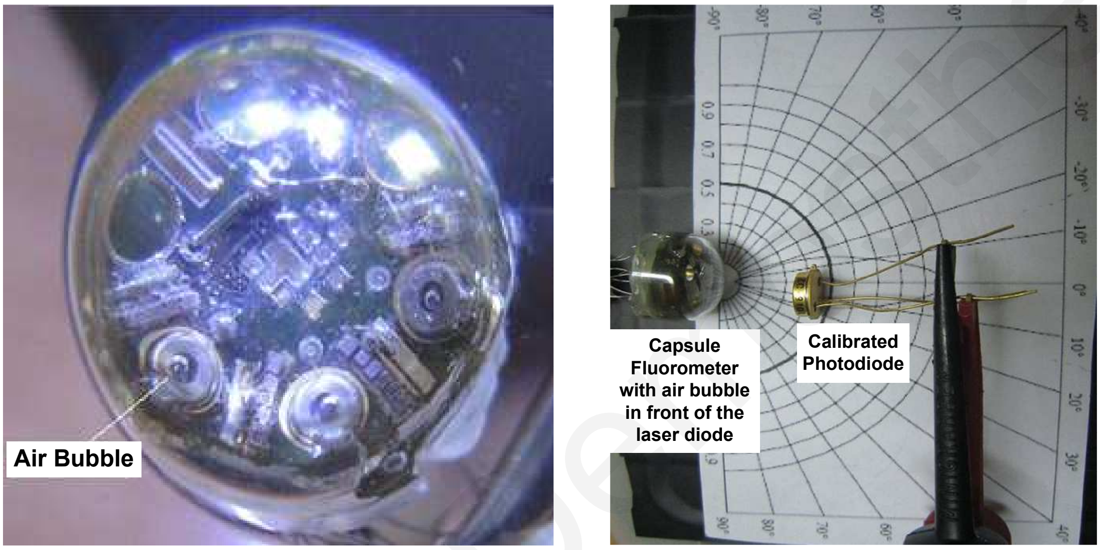

(a)

(b)

Figure 3.23: a) The formation of an air bubble in front of each LD, b) Experimental setup for verification of the principle.

The results are shown in Figure 3.24, where the data set marked with blue corresponds to the angular distribution of laser intensity, scattered by an air bubble micro-lens, while the data set marked with red corresponds to same measurements obtained only by a LD. It is observed that the air bubble causes a further divergence of the laser beam, which has an initial divergence angle of 17°, as stated in the data sheet [4] and also presented in the experimental data. The intensity of light at a diverging angle of 30°, is almost half to the intensity measured at the optical axis (0° divergence). Thus, a light diverging of 60° from each one of the six laser diodes, can completely illuminate the walls of the small intestine, though the intensity will be lower at the 30° divergence angle.

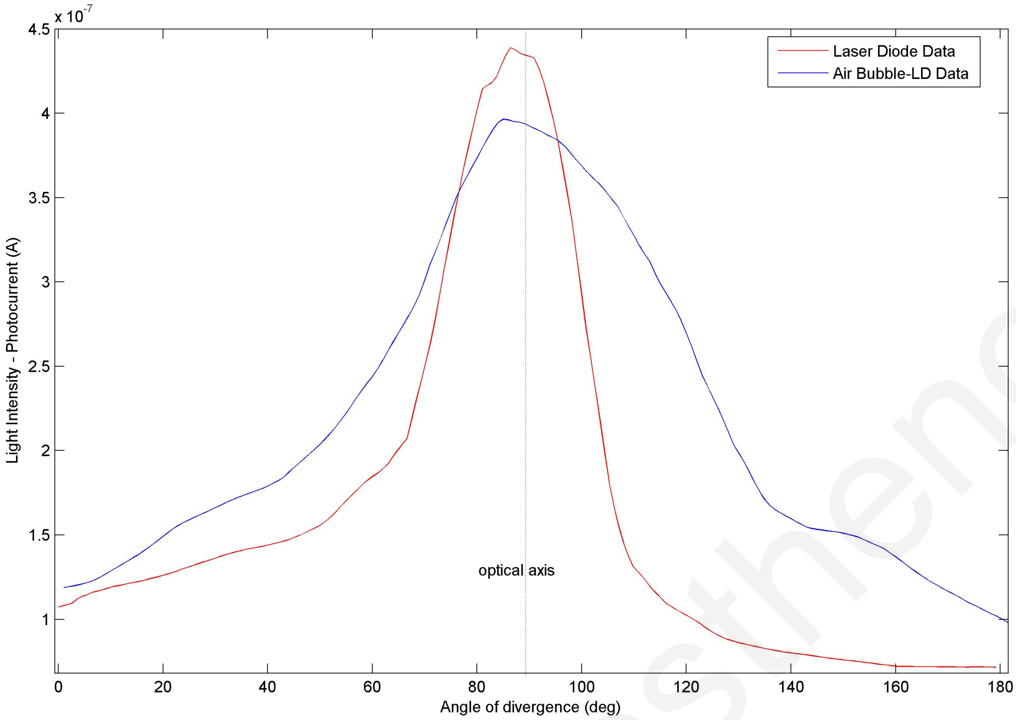

Figure 3.24: Angular distribution of light intensity of LD, scattered by an air bubble in index matching epoxy. A divergence of light, by the air bubble, at higher angles is observed compare to the angular distribution of the LD's intensity.

3.6 Conclusions

This chapter concludes with several decisions and results on the optics and opto-electronics of the system. These are concluded below:

- As an excitation source, a laser diode with emission wavelength at around 780 nm, is used. The narrow spectral range of the LD, allows the more efficient filtering of the excitation spectrum from the fluorescence.

- A long pass optical filter with cut-off wavelength at 800 nm can reduce the excitation light, allowing the detection of the emitted fluorescence signal.

- A constant current LD driver circuit that operates in power cycling mode, is used. Such a circuit provides relatively constant luminescence to the LD, reducing the variations of the fluorescence intensity. Calculations show that, those variations can not affect the ability of the system to detect and discriminate the two critical concentrations of ICG.

- As a photodetector, a photodiode is used, that has low dark current in comparison to a phototransistor and low bias voltage in comparison to an avalanche photodiode. Also, it does not need the extra charge pump and quenching circuitry.
- Acrylic is chosen as the capsule housing material, mostly because it is transparent to IR light and it is also approved for medical use.
- Side circular and front circular positioning of the optics and optoelectronics was decided, where the LDs and photodiodes are placed in a circular manner, illuminating a cross section of the intestine.
- The divergence of the laser diode beam to scan a larger segment of the intestine, can be realised either through micro-lenses constructed on the acrylic housing, or through an air bubble in the index matching epoxy, that acts like a micro-lens.

The following chapter addresses the design and implementation of the mixed signal electronics of the capsule, together with all the detailed considerations and calculations.

Chapter 4

Implementing the Electronics

This chapter presents the implementation of a screening capsule prototype that is able to detect and distinguish increased levels of IR fluorescence emitted from indocyanine green (ICG) aqua solutions of low concentrations. Several system optimisations on VHDL coding and hardware level are also presented, which are related to storage and power management, capsule structure and size, and optical data recovery. The following sections concern the customisation of a mixed signal electronic system with off-the-shelf components and its integration on a compact-size PCB. The system includes the following: excitation source driver, photodetector interface, an A/D converter, an accelerometer, a flash memory, storage and power management algorithms, signal processing algorithms, peripheral communication interface, contactless data transfer interface, reference circuits, timers and clock generator.

The general operation of the system can be summarized as follows. An excitation source driver bias the light sources with constant current so as to ensure constant intensity of the excitation light (section 3.1.1) and thus give a consistent fluorescence value for a given concentration of fluorophore. The light sources flash sequentially through switching transistors in a circular arrangement, thus covering a cross sectional view of the intestine. Simultaneously, the photodetectors receive the fluorescence light coming from the excited fluorophore, which carries information on the existence or non-existence of cancer, and through amplification, the weak fluorescence will be enhanced. The signals are then be digitized by an ADC and stored to an internal flash memory. After, to readout the stored data, a 4-wire SPI interface and/or an optical data transmission interface can be used.

Variations in physical sample distance, due to variations in the capsule speed, can either be handled by having a high data sampling rate, which is power hungry, or through a speed/acceleration dependent sampling rate. In addition, a complex programmable logic device (CPLD) is responsible for the signal processing, the control of photo-transducer switching, the storage and power management, and the SPI communication with the peripherals IC (i.e. ADC, flash memory, accelerometer). Furthermore, a clock generator is needed to provide a global clock to the CPLD, and also several voltage reference circuits to power supply all the devices.

4.1 The First Generation Capsule

Electronic circuit design usually requires a few iterations to converge on a circuit. In this section the first generation capsule is presented, which was used to show the feasibility of such a fluorescence detection capsule and which was used as a stepping stone towards an optimized design. As there is educational value in a first iteration, this is presented, rather than directly present the second generation capsule.

4.1.1 Hardware Architecture and Implementation

The implemented hardware satisfies the three important factors that an IR screening capsule system must have: a) IR fluorescence sensitivity, b) small size, and c) low power consumption. The system hardware is shown in Figure 4.1 and consists of a flexible PCB (brown) connected to the capsule main body rigid PCB (green) through a mini ZIF connector (FH26-23S-0.3SHW). Figure 4.2 shows the full four layer PCB, which was designed in Altium software. Standard mixed-signal design techniques were used with separated analog and digital parts, as well as different ground and power plane. The main body rigid PCB has dimensions 13 mm x 27 mm, while the flexible PCB has dimensions 41 mm x 27 mm (Figure 4.3) so it can be wrapped around the rigid PCB in a diameter of 13mm, forming in that way a compact cylindrical shape with the optical photo-transducers (laser diodes, photodiodes) placed in the side circular structure described in section 3.4.1.

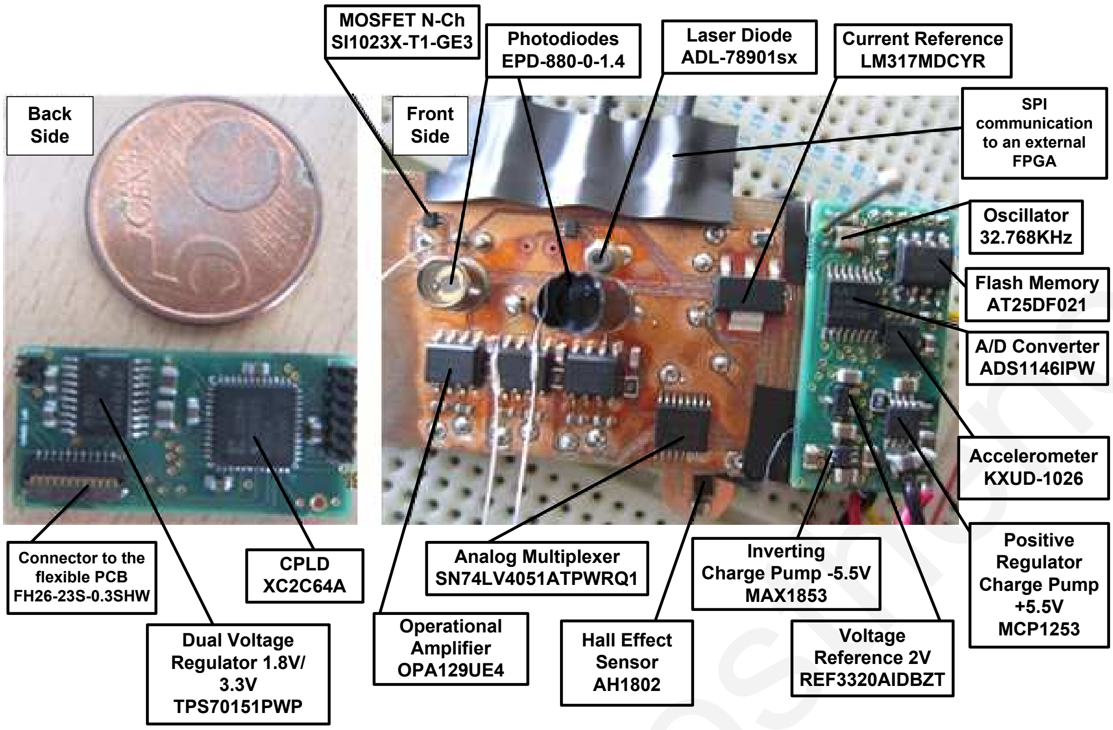

Figure 4.1: Hardware Implementation.

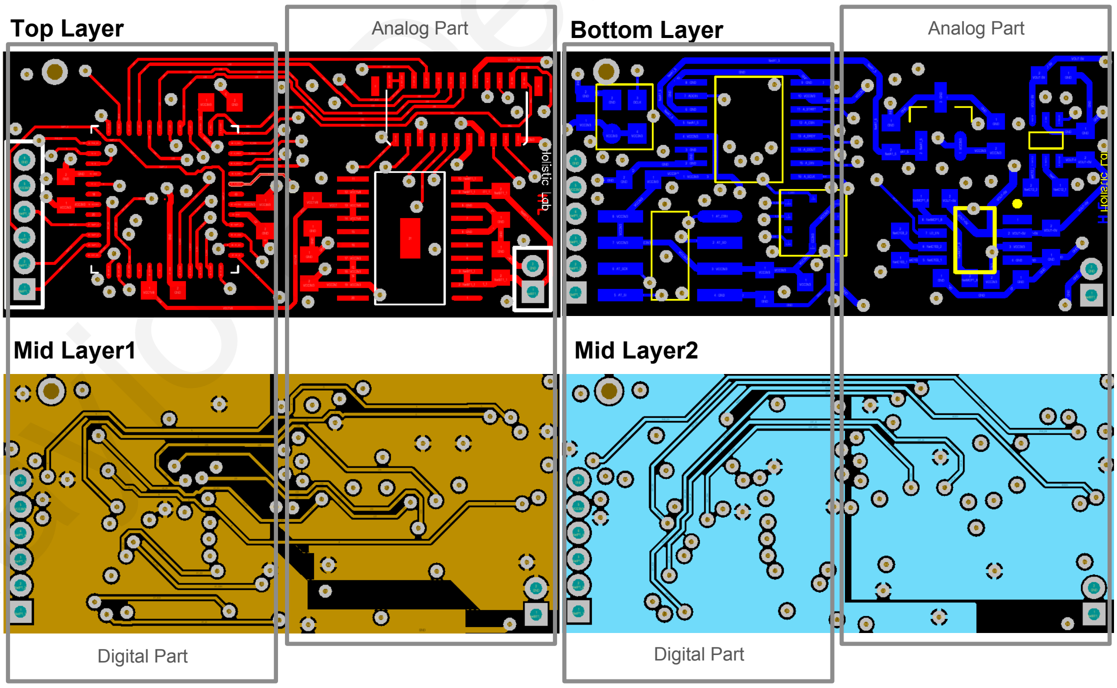

Figure 4.2: Four Layer Rigid PCB: top layer (top left corner), bottom layer (top right corner), mid-layer-1 (bottom left corner), mid-layer-2 (bottom right corner).

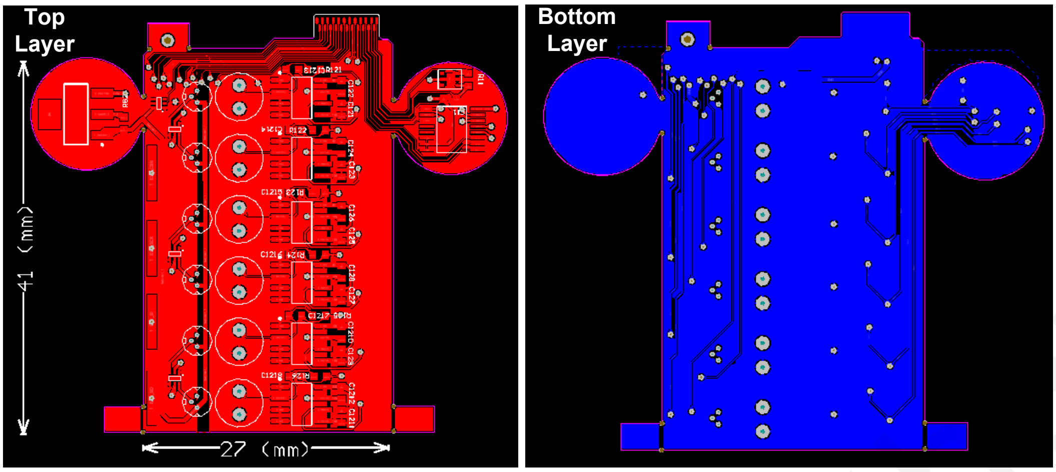

Figure 4.3: Two Layer Flexible PCB: top layer (red), bottom layer (blue).

Figure 4.4 shows the hardware architecture of the capsule, which is segmented in the flexible (Circuit Schematic - Appendix A) and the rigid PCB (Circuit Schematic - Appendix A). The flexible PCB consists of: (1) six excitation laser diodes (ADL-78901sx) with a constant current biasing module (LM317MDCYR), (2) n-channel MOSFET transistors (SI1023X-T1GE3) for lighting up the LDs one at a time, (3) six detector photodiodes (EPD-880-0-1.4) with their operational amplifiers (OPA129UE4), (4) an analog multiplexer (SN74LV4051ATPWRQ1), and (5) a Hall effect sensor (AH1802). The rigid PCB consists of: (1) a sixteen bit ADC converter (ADS1146IPW) with 2V external voltage reference (REF3320AIDBZT), (2) a non-volatile memory (AT25DF021) to store the collected fluorescence data, (3) a three - axis accelerometer (KXUD-1026) with one of its axes aligned in the direction of the movement, (4) a CPLD module (CoolRunner-II, XC2C64A) that implements signal-processing algorithms and SPI communication protocol to interface with the above peripheral units, (5) an oscillator of 32kHz for driving the master clock of the CPLD and several voltage regulators; (6) a dual voltage reference 1.8 / 3.3V (TPS70151PWP) to power up the CPLD and the peripheral units and (7) charge pumps of ±5.5 V (MAX1853 and MCP1253) for biasing the operational amplifiers required to detect the tiny photocurrent.

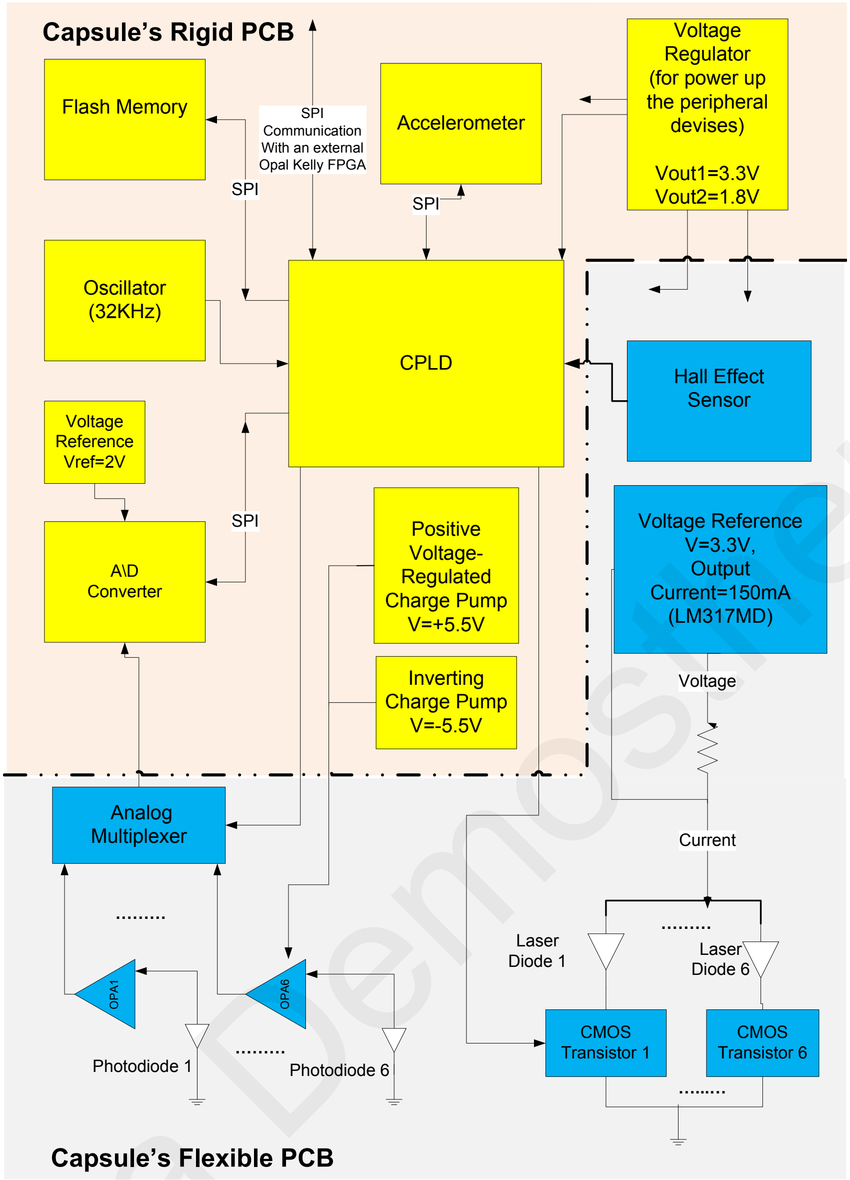

Figure 4.4: Hardware Architecture.

4.1.2 System's Components Documentation

The system required a processor responsible for the management of all the functions taking place inside the capsule. For this purpose, a Complex Programmable Logic Device (CPLD) was preferred over a Field Programmable Gate Array (FPGA), a Digital Signal Processor (DSP) and a micro-controller.

Micro-controllers lack the ability of parallel processing, since they perform one instruction cycle at a time. This fact makes them require a relatively fast clock in comparison to programmable logic devices, leading to an increase in power consumption. Moreover, a micro-controller that is small enough in size has much fewer IOs than a programmable logic devices of comparable size, thus introducing a limitation on input-output signals usage. Also, programmable logic devices (CPLDs and FPGAs) provide increased performance over traditional DSPs with the same flexibility, since they can handle more processes at the same time because of their parallel architecture. Likewise, programmable logic devices have a flexible architecture that can be adapted for a specific DSP function and they have sufficient capacity to fit multiple MACs (Multiply/Accumulator) or algorithms into a single device along with the interface circuitry required by the application, as opposed to a traditional DSP that only has a single MAC. In general, programmable logic combines the flexibility of a general-purpose DSP plus the speed and density of an ASIC implementation [51], [78], [77], [91], [38].

CPLDs have a non-volatile character, small size and low power consumption, which make it preferable over FPGAs. FPGAs and CPLDs are composed of configurable logic cells or macro-cells with programmable interconnects between the CLBs (Configurable Logic Block) and the inputs and outputs. FPGA has much more logic capability than CPLD and is usually found within complex applications. CPLDs typically have thousands to tens of thousands of logic gates, while FPGAs typically range from tens of thousands to several million. Although, for less complex high speed designs and low power applications, CPLDs are more suitable. The important thing with CPLDs is their non-volatile character, which allows the device to store the logic configuration program even when no supply exists and to function immediately on system start-up. On the contrary, FPGA with SRAM-based configuration character loses any programming when the device is not powered, so it must be reconfigured each time after power-up. To avoid losing the configuration program, an external configuration memory moduleis needed, such as a ROM or flash memory. This implies occupation of more space on the PCB, which is undesirable [13], [91], [101], [109], [91].

Transimpedance amplifiers with low input bias current and low input current noise are also used in the system, since the photodiode's photocurrent, generated from the fluorescence light, is expected to be very small; in the order of pico to nanoamperes (see Figure 3.7). An input bias current on the inverting terminal of the amplifier will result in an output offset. To minimize these effect, transimpedance amplifiers with very low input bias current are preferred. Also, amplifiers with large input current noise to overshadow the weak signals, can not be practical for amplification of very small current. Table 4.1 shows the characteristics of select amplifiers, with the OPA129 outperforming the others, due to its small surface mount package, the comparable low input current noise and the low (some fA) input bias current. Furthermore, OPA129 has a substrate pin that should be connected to a guard ring around the input and be driven by a circuit node equal in potential to the input terminal of the op amp, resulting in a zero potential difference. In the presented case, the guard ring is grounded because of the virtual grounded input. In that way the input is well shielded, minimizing the leakage of photocurrent from the terminal.

Table 4.1: Important Characteristics of Several Transimpedance Amplifiers

Amplifiers	Input Bias Current	Input Current Noise	Supply Current	Package
AD549L VS = ± 15 V	40-60 fA	0.11 fA/Hz	0.6-0.7 mA	8-PinTO-99
LMC6001AL V+ = 5V, V− = 0V	10-25 fA	0.13 fA/Hz	0.45-0.75 mA	8-Pin TO-99, 8-Pin PDIP
LMP2231 V+ = 5V, V− = 0V	20-1000 fA	10 fA/Hz	0.01-0.016 mA	SOT-23, 8-Pin SOIC
LMP7721 V+ = 5V, V− = 0V	3-20 fA	10 fA/Hz	1.1-1.5 mA	8-Pin SOIC
opa111BM VS = ± 15 V	500-1000 fA	0.4-0.6 fA/Hz	2.5-3.5 mA	8-Pin TO-99
opa128LM for VS = ± 15 V	40-75 fA	0.12 fA/Hz	0.9-1.5 mA	8-Pin TO-99
opa129 VS = ± 15 V	30-100 fA	0.1 fA/Hz	1.2-1.8 mA	SO-8

The digitization is performed via a 16-bit sigma-delta A/D converter (ADS1146), with an internal digital filter and oscillator, and an external voltage reference of 2 V that allows a conversion of voltage signals in the range of 30.5 uV ($2V/(2^{16}-1)$) to 2 V. Since the output voltage is a result of the photocurrent amplification through an operational amplifier with a negative feedback resistor of 30 MΩ, the range of the measurable current with the specific ADC is from 1 pA to 66.6 nA (Figure 4.5 and equations 4.1 - 4.2), which is in agreement with the fluorescence photocurrent values. Changes in the ADC voltage reference and the value of the feedback resistor can redefine a new measurable current range in the case of fluorescence detection failure. For example, with 1 V ADC voltage reference and 300 MΩ feedback resistor, the measurable current range shifts to lower values from 50 fA to 3.3 nA, which justifies the selection of an amplifier with input bias current and current noise in the fA scale. The trade-off in that case is that, by increasing the feedback resistor the thermal noise increases.

$$I_{min} = \frac{V_{min}}{R} = \frac{\frac{2V}{2^{16}-1}}{30M\Omega} = 1.02pA \tag{4.1}$$

$$I_{max} = \frac{V_{max}}{R} = \frac{2V}{30M\Omega} = 66.6nA \tag{4.2}$$

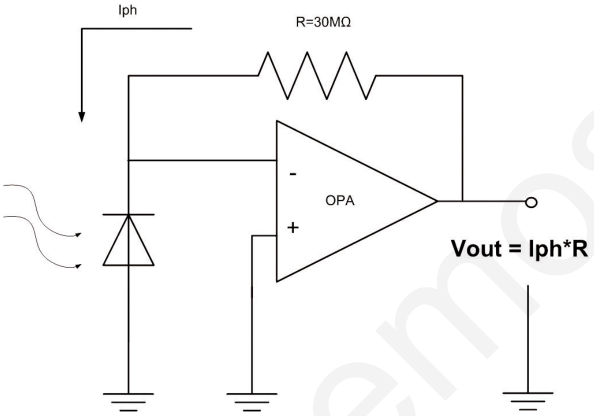

Figure 4.5: Photocurrent amplification through an operational amplifier with a negative feedback resistor.

A flash memory (AT25DF021) of 2 Megabits capacity was chosen for the storage of the digital fluorescence data in the capsule. With a data resolution of 16-bits, a sampling rate at 6 samples per second (since there are 6 LDs-photodiodes and, thus, six fluorescence data per screening cycle) and a five-hour maximum screening process of the small intestine area (with 8 hours travel to the overall digestible system), a storage capacity of 1728000 bits (16 bits * 6 sps * 60 s * 60 min * 5 hours) was needed, which makes the 2 Magebits flash memory ideal for the specific application. Flash memory is a non-volatile storage chip that keeps the data saved even when the power is removed and can be electrically erased and reprogrammed. It is considered as a specific type of EEPROM (Electrically Erasable Programmable Read-Only Memory) with the difference that it is erased and programmed in large blocks. EEPROM erases and rewrites its content one byte at a time or, in other words, at byte level. On the other hand, flash memory erases or writes its data in entire blocks, which makes it a very fast memory compared to EEPROM. The key advantage of flash memory above other storage methods is its low power consumption. For that reason a serial flash memory was chosen, small in area size, with low power dissipation during write operation at around 12 mA, that uses a serial SPI interface for sequential data access.

Last but not least, it was confirmed that the output current of all the voltage regulators can feed the following stages.

1) The charge pumps MAX1853 (-5.5 V) and MCP1253 (+5.5 V) with output currents 30 mA and 120 mA respectively supplying the six operational amplifiers (OPA129UE4) with total current dissipation of 10.8 mA (1.8 mA maximum current consumption from each one).

2) The external voltage reference REF3320AIDBZT with output current 35 mA connected to the ADC with reference input current of 30 nA.

3) The current reference module consisted of a voltage regulator LM317M and a feetback resistor with maximum output current 500 mA biasing the laser diodes (one at a time) with 100 mA current.

4) The dual output voltage regulator TPS70151PWP with output current 500 mA at the 3.3 V output and 250 mA at the 1.8 V output feeding all the digital and analog peripherals components with total current dissipation at around 113 mA.

4.1.3 Hardware Functionality

Low concentration aqua solutions of indocyanine green have an excitation maximum at 780 nm and an emission maximum at 810 nm. The fluorescence emission spectrum is around 790 nm to 860 nm (see Section 2.3 for details). Therefore, the capsule system is equipped with laser diodes having an excitation wavelength at 785 nm biased intermittently with 100 mA constant current, providing 131 mW optical intensity (equation 3.1). For each LD there are corresponding photodiodes, which operate in photovoltaic mode where no reversed bias is applied, resulting in lower dark current and also lower shot noise current. The photodiodes have large active area (1.2 mm^2) for the detection of the weak fluorescence signal emitted by the ICG fluorophore. The large active area gives the system its high sensitivity and good signal-to-noise ratio. Furthermore, each photodiode has an integrated optical long-pass filter, with a cut-off frequency of 800 nm, to prevent the high-intensity excitation wavelengths from reaching the detector. Thus, the resulting photocurrent is mainly produced by fluorescent light. The produced photocurrent is amplified and converted to an output voltage through a transimpedance amplifier, which is then digitized and stored in a flash memory. When the hall sensor is activated, the system is switched into data extraction mode and only then the data can be recovered from the system. With that functionality, there is an option of placing the capsule in a magnetic case allowing in this way the realisation of wireless data extraction. At this stage, the data are extracted from the capsule system to an external Opal Kelly FPGA board through 4-wire SPI communication and recovered as a .bin file through a USB interface.

More specifically, an SPI master module is implemented in an Opal Kelly FPGA (VHDL coding - Appendix B) and is responsible for externally controlling the capsule internal flash memory through 4-wire SPI signals (CSn, SCK, SI, SO). The flash memory has to obey unprotecting, erasing, writing and reading the memory. The commands for those instructions were given through a Front Panel Xilinx interface (Front Panel Coding - Appendix B), which was made specifically for this purpose. The Front Panel interface is linked with the SPI master VHDL code. Functionality is implemented in the form of, several push buttons GUI: the Unprotect button releases all the sectors in the memory from protection and the Erase button prepares the memory for a new writing procedure by deleting any written data that occupy memory space. This function should be done every time that new data is obtained, otherwise the writing can not be accomplished properly, leading to the storage of wrong data values. By pressing the Read Data push button a read memory command is executed and all the data from the flash memory are moved to a pipe in-out memory within the external FPGA. Then, with the BTPipe button all the data are recovered to a .bin file through USB interface. The file can be imported in Matlab for further processing (MatLab coding - Appendix B).

A CPLD was configured to perform a number of tasks that follow the timing diagram shown in Figure 4.6: (a) to flash the six excitation laser diodes in sequence at least every one second with a pulse duration of 5 ms, (b) to multiplex the fluorescence signals to an ADC, which signals were sensed from a corresponding photodiode and amplified to a transimpedance amplifier, (c) to store the collected data to flash memory and (d) to drive the SPI master modules, a clock divider and a system controller. One of the other tasks of the controller is to regulate the sampling rate of the capsule, which moves slowly most of the time (velocity of intestine peristalsis is 1-2cm/min [37]). During rapid movement, the output of an accelerometer is used to increase the sampling rate to 10 full scans/second and thus ensure a thorough scan of the G.I. tract, whilst consuming less power than if a fixed sampling rate was used (see section 4.3.1).

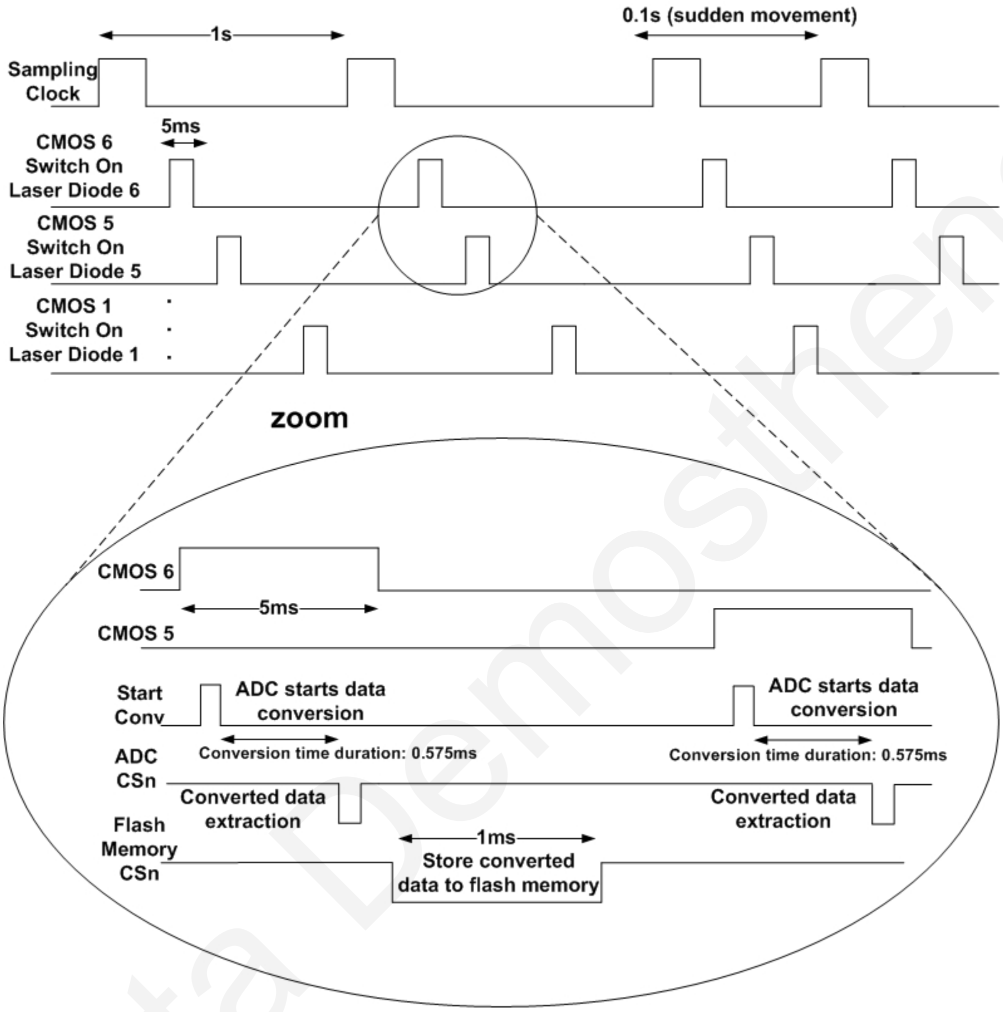

Figure 4.6: Timing Flow Diagram.

Since the flashing duty cycle and the excitation pulse of the laser diode have been defined, the emitted energy per square centimetres must now be estimated and confirm that this is lower than the maximum permissible tissue exposure (MPE) given from equation 3.23. With an LD pulse duration at 5 ms, the MPE is calculated around 0.22 J/cm^2. Now, from equation 3.1, the optical power emitted by the LD with $5 * 10^{-3}$ flashing duty cycle (5 ms/1 s), is estimated at around 0.66 mW, which corresponds to an energy of $3.3 * 10^{-6} J$ $((0.66 * 10^{-3} W) * (5 * 10^{-3} s))$. That energy hits a tissue area of radius 7.85 mm (equation 3.35)($\pi * R^2 = 1.9 cm^2$), which corresponds to exposure energy per square centimetre of $1.7 * 10^{-6} J/cm^2$ $((3.3 * 10^{-6})/(1.9) J/cm^2)$. This value is far below the MPE.

4.1.4 Experimental Testing and Results

4.1.4.1 System Calibration

The system was calibrated by replacing a photodiode with a current source (Keithley 6221) that simulates the fluorescence photocurrent. Figure 4.7 shows the resulting decimal values with the applied DC currents, and gives an evaluation of the order and range of photocurrent that can be detected and measured with the proposed system.

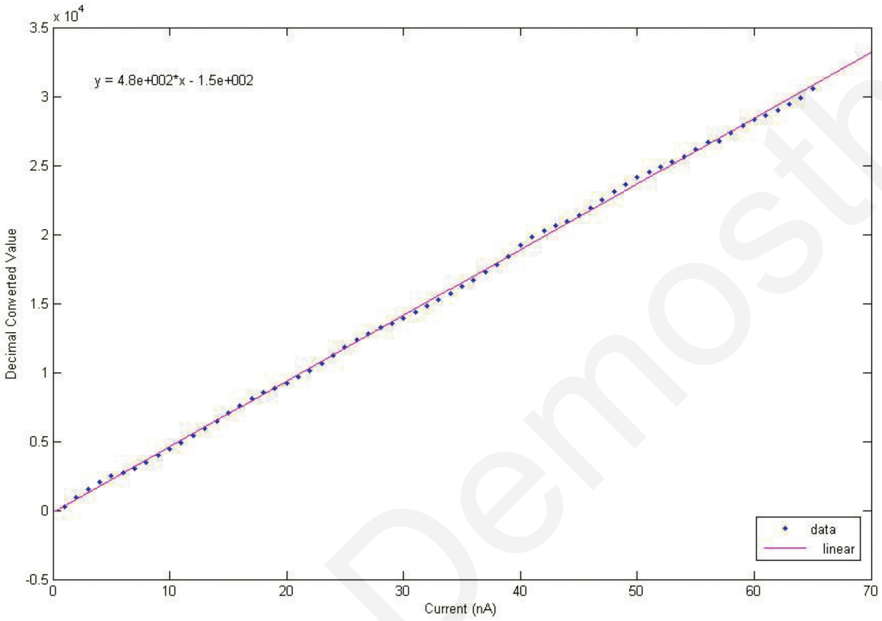

Figure 4.7: Decimal A/D Converted Values Vs. Photocurrent.

4.1.4.2 ICG Concentration Detection

The main and the most important functionality of the presented system is the ability to detect increased levels of fluorescence emitted by ICG solutions of low concentrations. That functionality will provide a system able to detect and discriminate molecular ICG contrast agents, which are selectively up-taken by cancerous cells. Inayama et al. [43] present the development of an indocyanine green derivative used as an infrared fluorescent labelling substance for the detection of microlesions by an IR fluorescence endoscopy. They show that human gastric cancer tissues stained with different concentrations of ICG in the range of 125nM (0.1ug/ml) to 12.5uM (10ug/ml) can provide sufficient fluorescence intensity. Based on this study, the developed prototype uses a transimpedance amplifier with a 30 MΩ resistor in the feedback loop, providing a gain of 0.03 V/nA, thus enabling the detection of ICG concentrations in the nanomolar to micromolar scale.

ICG solution of 250 uM was prepared by dissolving 0.39 mg of ICG in 2 mL distilled water. Lower concentrations were created from the dilution of a portion of the main solution with distilled water. The several solutions of different concentrations of ICG were placed in cylindrical transparent glass cuvettes, of 2 mL capacity. The experimental setup is shown in Figure 4.8. The cuvettes with the ICG solutions were placed in a dark box for isolating the optical part of the system (laser diode and photodiode) from any outside light sources. The excitation laser diode and the photodiode (for the detection of the fluorescence signal) were placed in a perpendicular structure as shown in Figure 4.8. Thus, the detector photocurrent was mostly produced by ICG fluorescence light, since the direct and reflected excitation light is reduced with the perpendicular arrangement. The fluorescent signal was acquired from the capsule system and the digitised value was stored in the internal memory. The converted data were then recovered with an external FPGA and a computer front panel interface through SPI communication and pipe out procedure.

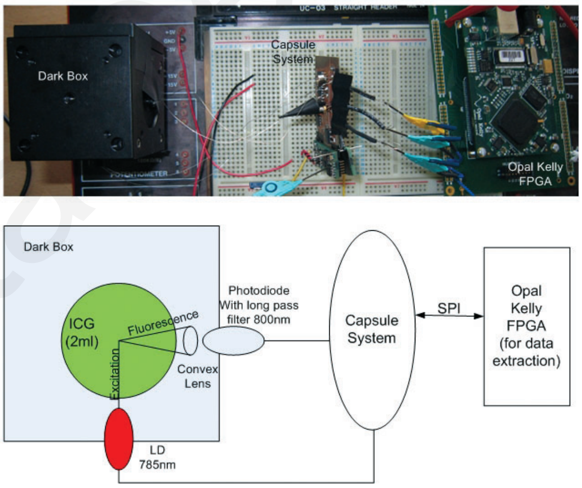

Figure 4.8: Experimental Setup for ICG Concentration Detection.

The in-vitro experimental results are shown in Figure 4.9. The system is able to detect different concentrations of ICG from 20 nM to 3.6 uM, with sensitivity at about 0.5 uV/nM. However, a higher sensitivity can be achieved with changes in photocurrent amplification. Although, Figure 4.10 shows that the two critical concentrations of ICG related to abnormal and healthy tissues at 225 nM and 19 nM respectively (based on section 2.3) are clearly discriminated.

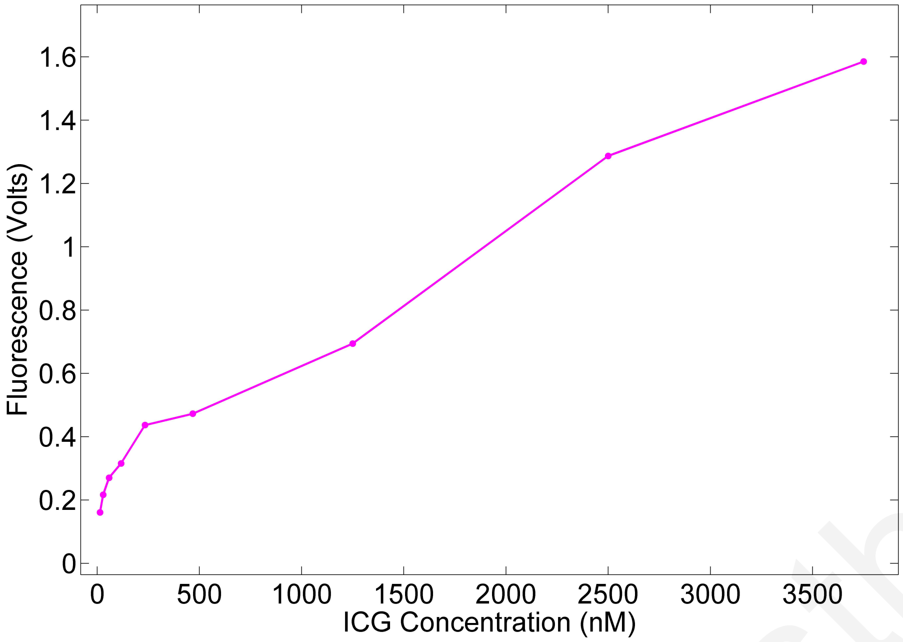

Figure 4.9: Fluorescence Vs. ICG Concentration.

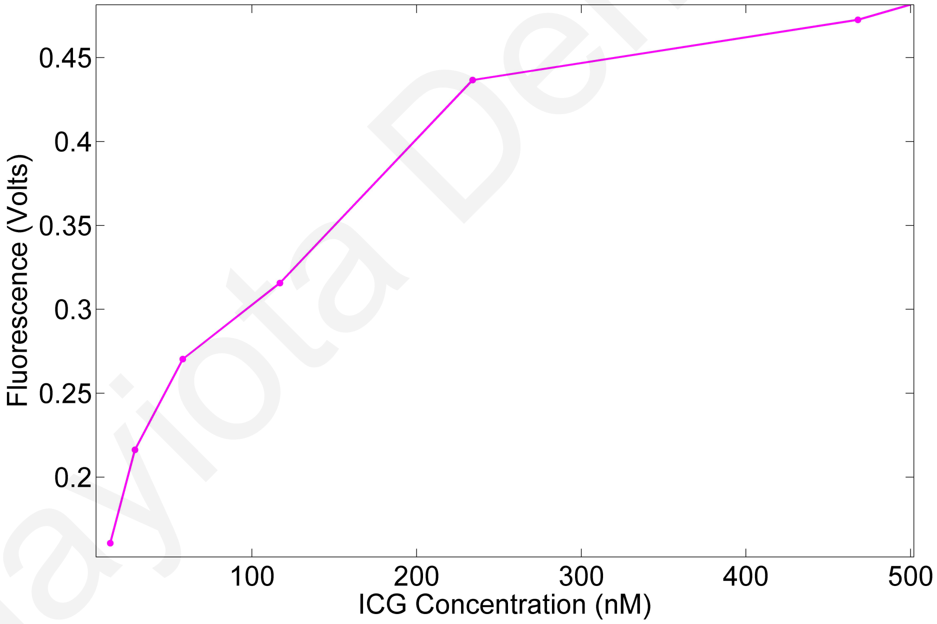

Figure 4.10: ICG Fluorescence at the Lower Concentrations.

After demonstrating that the objective of detecting such low levels of fluorescence without having to resort to designing a custom ASIC, a second generation capsule was designed, this time aiming for a more compact structure and with additional elements for reading out data wirelessly.

4.2 Second Generation Capsule

The first generation design indicated the feasibility of fitting a fluorometer with in a capsule and including sufficient data storage space to screen the small intestine. The second generation capsule is an optimized version, that capitalizes on smaller components, a custom designed rigid-flex PCB, and on lessons learnt from the previous iteration. This led to a prototype that: a) has a size comparable to the size of the existing endoscopic capsule, b) has low power consumption for allowing an approximate 8-hour operation for screening the entire G.I. track, and c) has IR fluorescence sensitivity for detecting low concentrations of ICG and further detecting early cancer.

4.2.1 System Implementation and Functionality

Figure 4.12 shows a photograph of both sides of the system hardware, implemented on a flexible - rigid PCB (Circuit Schematic - Appendix A). Three rigid circular PCBs, that are 12 mm in diameter, are connected to each other through a flexible PCB in such a way that allows them to fold over in a more compact size, and pack tightly in the capsule case as illustrated in Figure 4.35a. The material of the capsule case is plastic (made from a test tube), for demostration purposes. Components required and signal density of the system, lead to a four layer PCB design, as is shown in Figure 4.13. A complete system was designed with dimensions that suitably small, to enable ingestion, but which are also large enough to enable the capsule to come into close contact with the intestine walls during peristalsis. Therefore, the dimensions of the encapsulated system are 13 mm x 25 mm, which are also comparable with the size of a typical imaging capsule with 11 mm diameter and 30 mm length.

Figure 4.11: The Encapsulation of the System in a Compact Capsule.

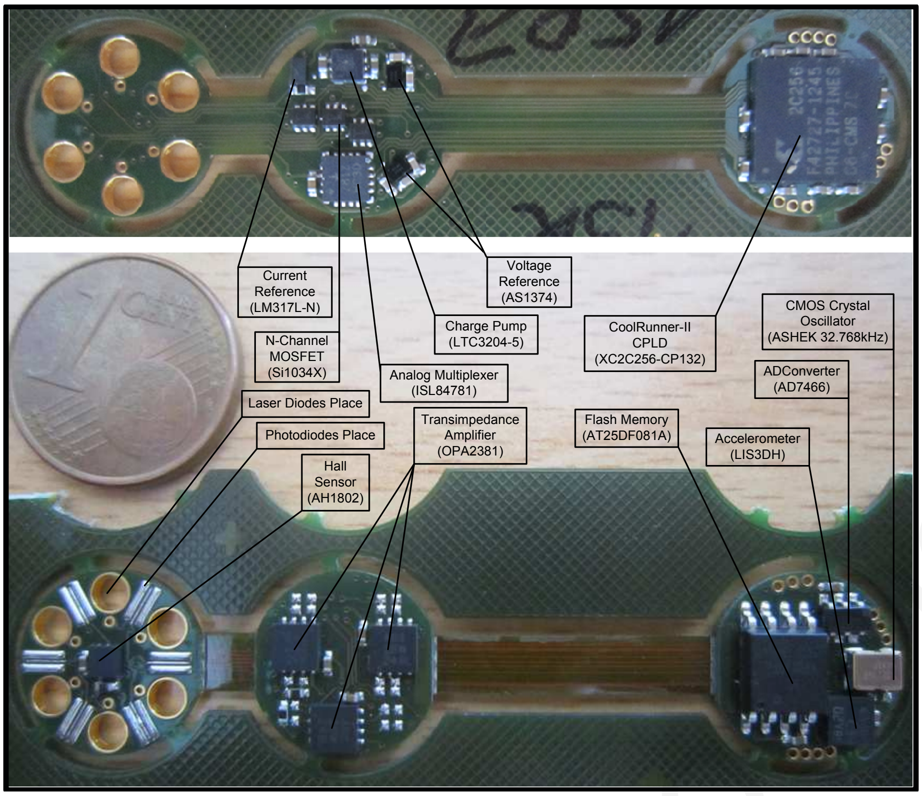

Figure 4.12: Hardware Implementation of the Second Capsule.

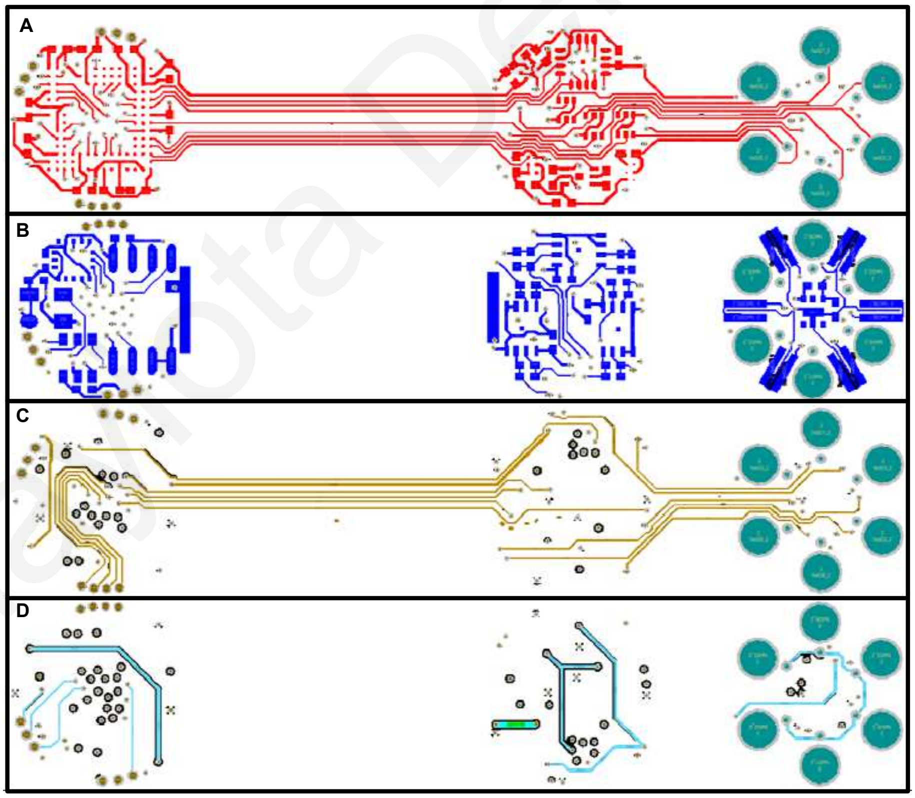

Figure 4.13: Four Layer PCB: (A)top layer, (B) bottom layer, (C) mid-layer-1, (D)mid-layer-2.

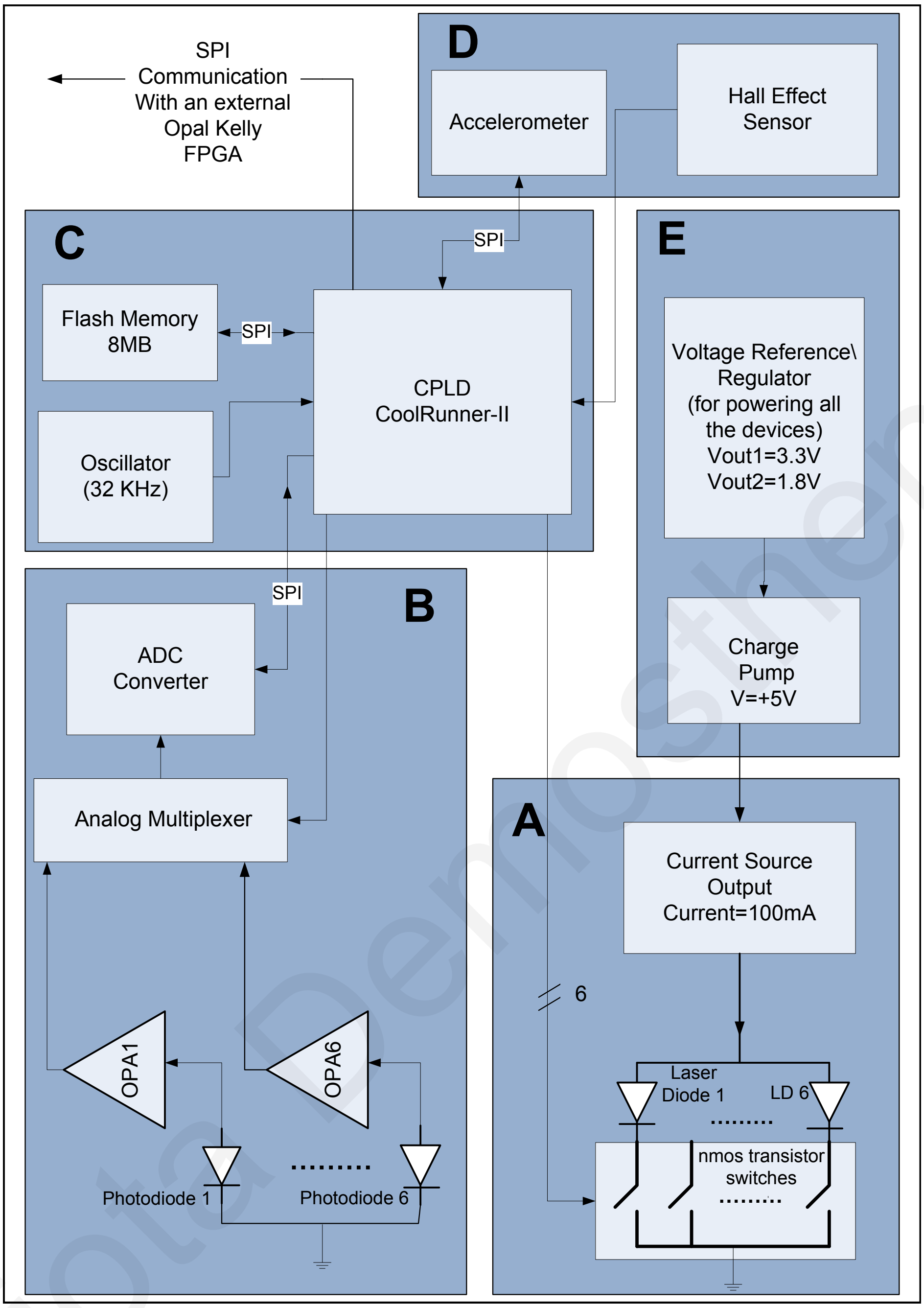

Figure 4.14: Hardware Architecture.

Figure 4.14 shows the hardware architecture of the capsule system. The PCB body consists of several modules: (A) An *Illumination Module* with six excitation laser diodes (ADL-78901SX) intermittently biased by a constant current source (generated via LM317L-N), which lit up in sequence, via n-MOSFET transistors (Si1034X), (B) A *Detection Module* with six detector photodiodes (EPD-880-8-1.4) connected to six operational amplifiers (OPA2381) for the amplification of the weak fluorescence signal, and an analog multiplexer (ISL84781), for sequentially selecting and routing each signal to a twelve bit ADC converter (AD7466), (C) A *Controller Module*, that includes a CPLD CoolRunner-II that implements signal-processing algorithms and SPI communication protocols to interface with the peripheral units, and a non-volatile memory (AT25DF081A) for storing the digitised fluorescence data, (D) A *Sensor Module* with a Hall effect sensor (AH1802) and a three-axis accelerometer (LIS3DH) for sampling rate regulations, (E) A *Power Module* with three different voltage supplies 1.8V/3.3V/5V, (AS1374 for 1.8/3.3V and LTC3204-5 for 5V) for powering the CPLD and the peripheral units.

As is shown in the Time diagram in Figure 4.15 the six laser diodes flash in sequence every one second with a pulse duration of 5 ms. A corresponding photodiode senses the fluorescence and produces a photocurrent which is amplified and multiplexed to an ADC. Each time that a LD is lit up (duration 5ms), a particular fluorescence signal is sampled multiple times and averaged to further improve the signal-to-noise ratio by $\sqrt{N}$, where N is the number of averaged samples. The result is stored in flash memory. During rapid movement, acceleration information is again used to decrease the sampling period from 1 s to 0.1 s.

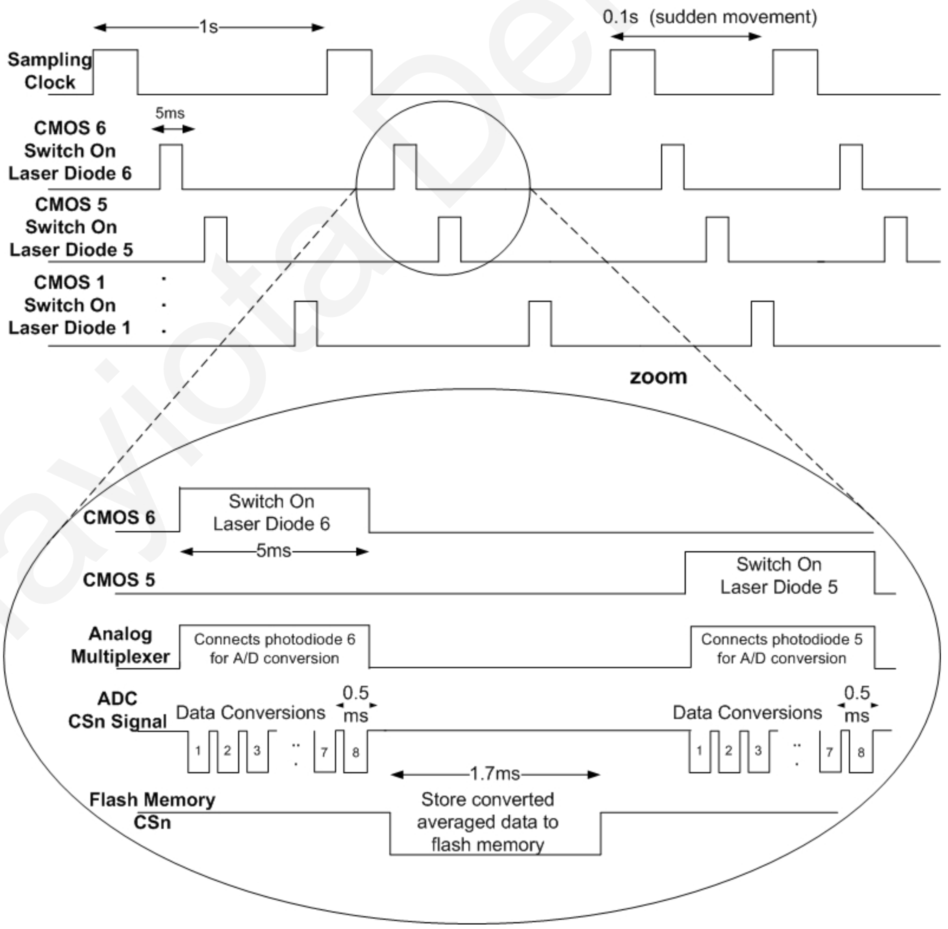

Figure 4.15: Timing Diagram.

When the screening procedure is accomplished, the data are extracted from the capsule, with the help of an external docking unit. The data coupling to the external docking unit is conducted through a wireless infrared data transmission scheme, which is activated through the onboard hall sensor, when the capsule is placed in the magnetic docking unit. A wireless scheme is needed since it would be very costly to develop hermeticly sealed conductive feedthroughs, and the laser diode transmitter is part in the capsule anyway. The external unit connects to a PC via a USB interface and displays the results.

4.2.2 Capsule Testing and Results

The key objective of the second generation capsule is to detect the increased levels of fluorescence given by swine intestine tissues, which are stained with the IRF dye ICG. Tadatsu et al. [88] present, the development of indocyanine green infrared-labelling agents that target microlesions presented in humans intestine. They show that indocyanine green derivatives with different concentrations in the range of 0.1ug/ml (~129 nM) to 500 ug/ml (~645 uM) can provide sufficient fluorescence intensity for diagnosis of microcancers with IR fluorescence endoscopy.

4.2.2.1 In-Vitro Experiments

The functionality of the second generation capsule was first tested in-vitro with the experimental setup used for testing the first capsule prototype (Figure 4.16).

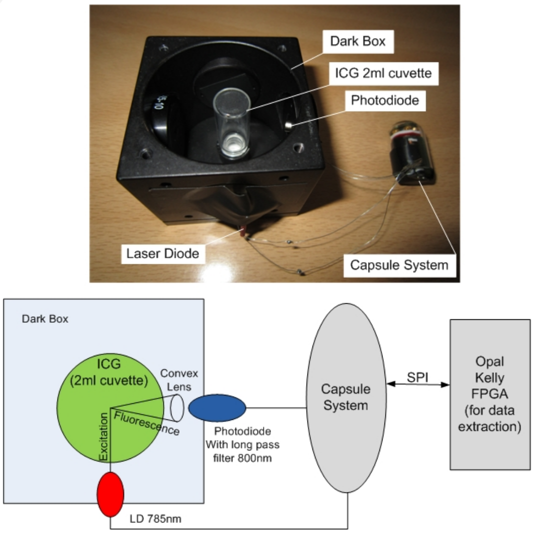

Figure 4.16: Perpendicular arrangement and environmental-light isolation of the optical part of the system for ICG concentration detection.

The following experimental data were collected through a single analog-to-digital conversions of the fluorescence signal, obtained from excitation processes of 5 ms duration (excitation pulse 5 ms). The fluorescence data exhibited large noise, which was introduced into the signal by the previous amplification stage with the MΩ feedback resistor (the noise coming from the photodiode is negligible by comparison). For that reason, the data underwent signal processing in Matlab before extracting the final results. Specifically, the fluorescence data of each ICG concentration were filtered with an equally-weighted eighth order moving average filter, i.e. the output is given by the sum of eight samples, each weighted with $1/8^{th}$ of their value. The mean value of the filtered data corresponds to the fluorescence binary value for each ICG concentration. Figures 4.17 to 4.19 show the fluorescence results with ICG concentrations at signal amplifications of 0.02 V/nA, 0.05 V/nA and 0.1 V/nA respectively. The use of the moving average filter enables the detection of different ICG concentrations. This filter then implemented on the system in order to provide real-time detection. The optimisation of the real-time averaging procedure is presented later in this chapter.

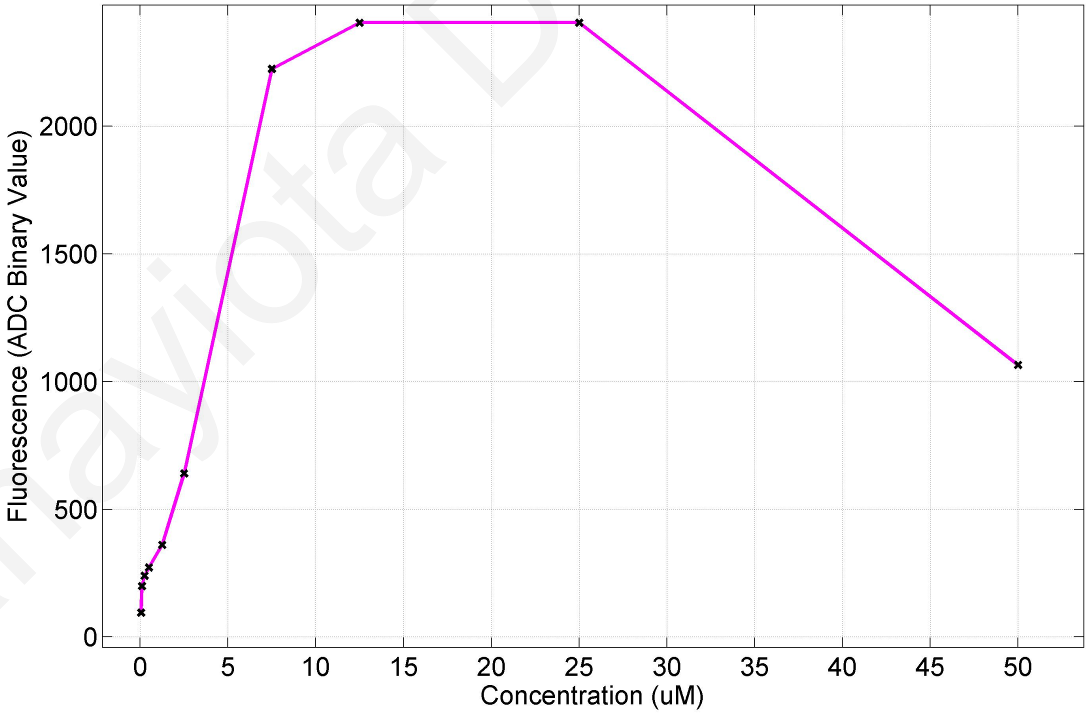

Figure 4.17: Fluorescence Vs. ICG concentrations under signal amplification with a 20 MΩ feedback resistor.

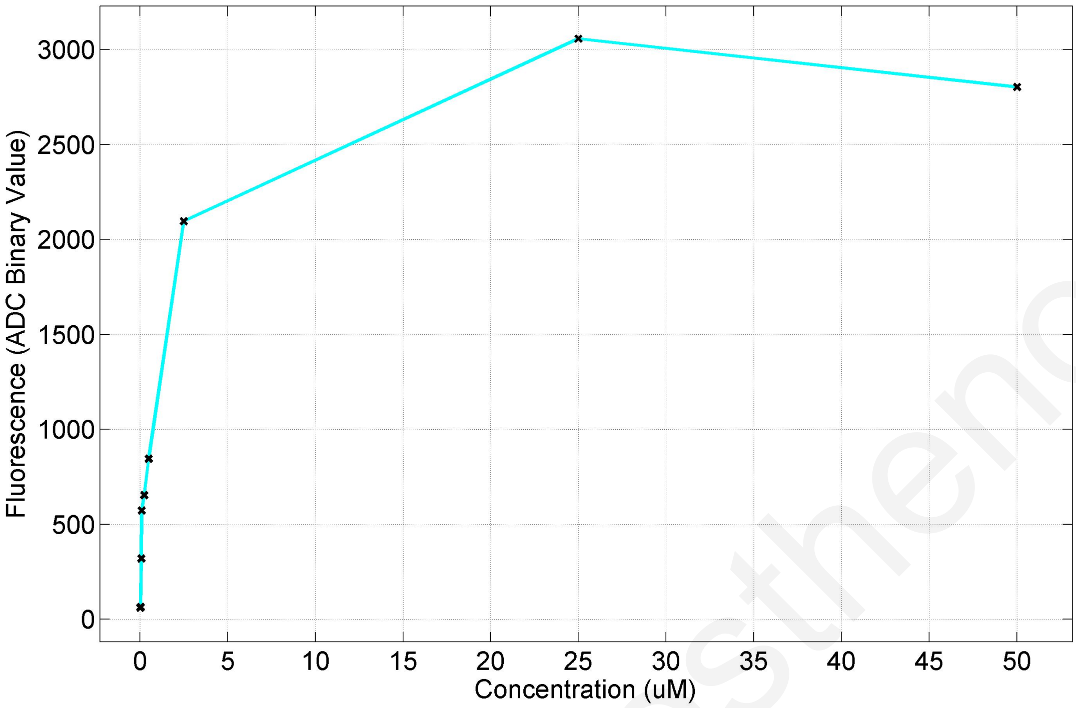

Figure 4.18: Fluorescence Vs. ICG concentrations under signal amplification with a 50 MΩ feedback resistor.

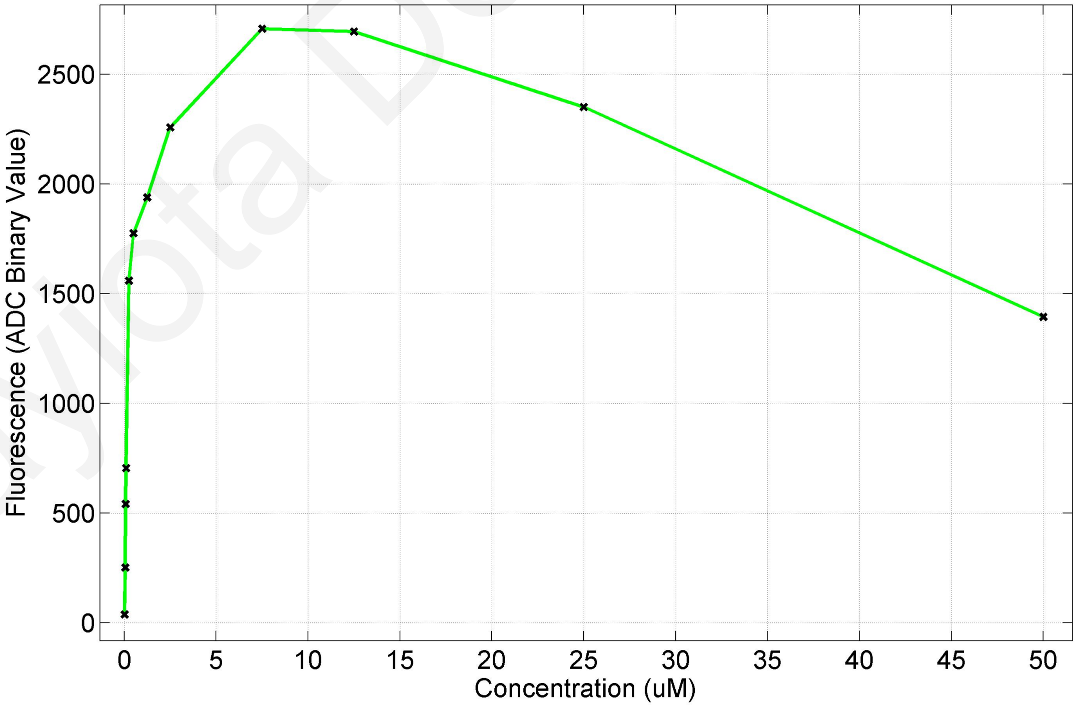

Figure 4.19: Fluorescence Vs. ICG concentrations under signal amplification with a 100 MΩ feedback resistor.

The effect of the excitation pulse duration on the fluorescence intensity was also investigated. Based on equation 3.1, the optical power of the excitation source increases at higher laser diode pulse duty cycle, resulting in an increases of the fluorescent intensity. Figures 4.20 and 4.21 show the ICG-fluorescence results, with ICG-excitation at different pulses durations of 4, 8, 16, 32, 64 and 128 ms. The results do not differ significantly, since the changes in the excitation pulse duration only slightly affect the fluorescent intensity, which also displays some other variations presented extensively in section 3.1.1. Thus, the excitation pulse was chosen to be around 5 ms, allowing the system to function with a lower power consumption with the laser diodes draining 100 mA current for just 5 ms in every excitation cycle.

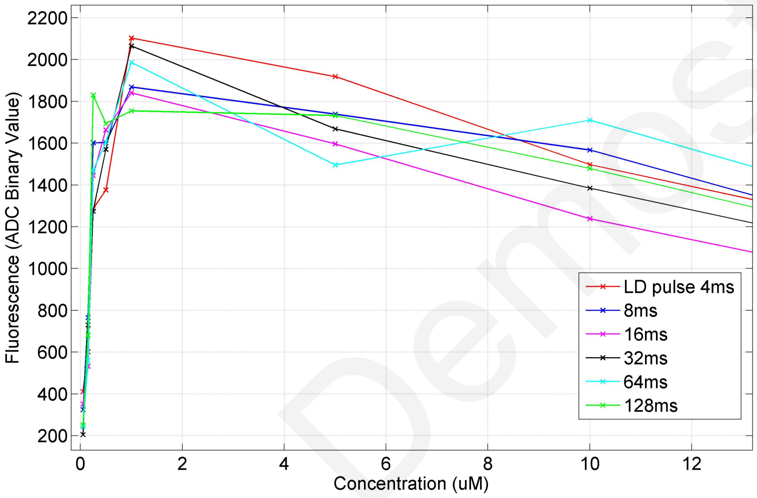

Figure 4.20: Excitation of ICG concentrations with different LD pulse durations.

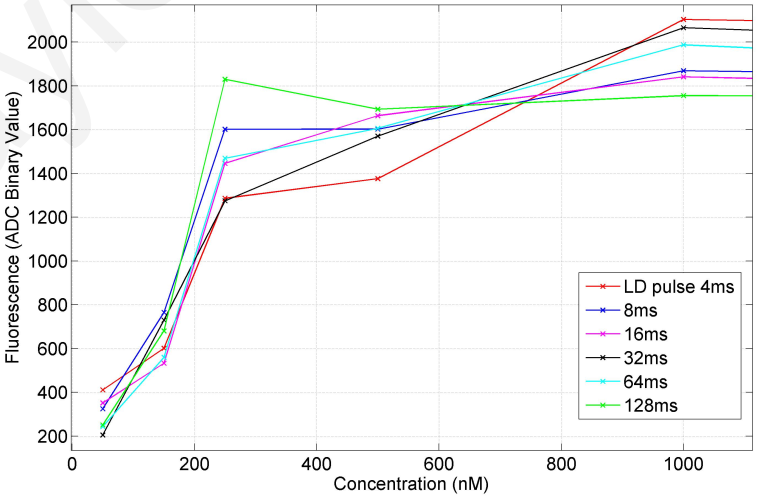

Figure 4.21: Zoomed-in results at lower ICG concentrations.

An additional factor that can make the system more reliable at detecting different fluorescence-intensity levels, is the reduction of the noise coming from the pre-amplification stage. However, this is non-practical, since the large amount of thermal noise to the signal is introduced by the big feedback resistor in the transimpedance amplifier. Although, the big feedback resistor is necessary to provide enough amplification to the fluorescence signal, allowing higher sensitivity in the discrimination of ICG concentrations in the nanomolar scale. Hence, a methodology was implemented that measures the average value of several fluorescence data collected in every excitation procedure (Figure 4.15). Figure 4.22 shows the averaging (blue line) of four and eight data samples of the noisy fluorescence data (red line). The larger the number of the fluorescence data collected in every excitation, the higher the noise reduction achieved through averaging.

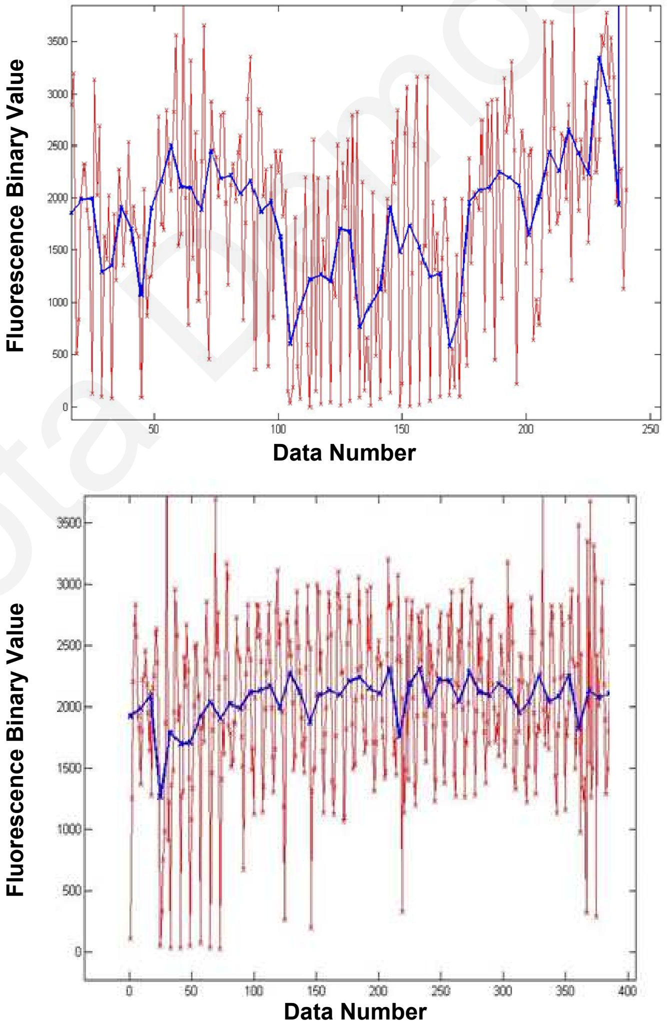

Figure 4.22: Fluorescence data averaging of four (top) and eight (bottom) data samples.

Figure 4.23 and 4.24 show the fluorescence results with ICG concentrations for different N (the number of averaged samples). It was observed that for $N = 4$ the noise levels are too high to be able to reliably detect the ICG trend with concentration. On the other hand, for $N = 16$ the smoothing effect of higher averaging becomes apparent with the lower fluorescence peak response. Thus, an averaging of eight data samples was considered as the most appropriate for the capsule system.

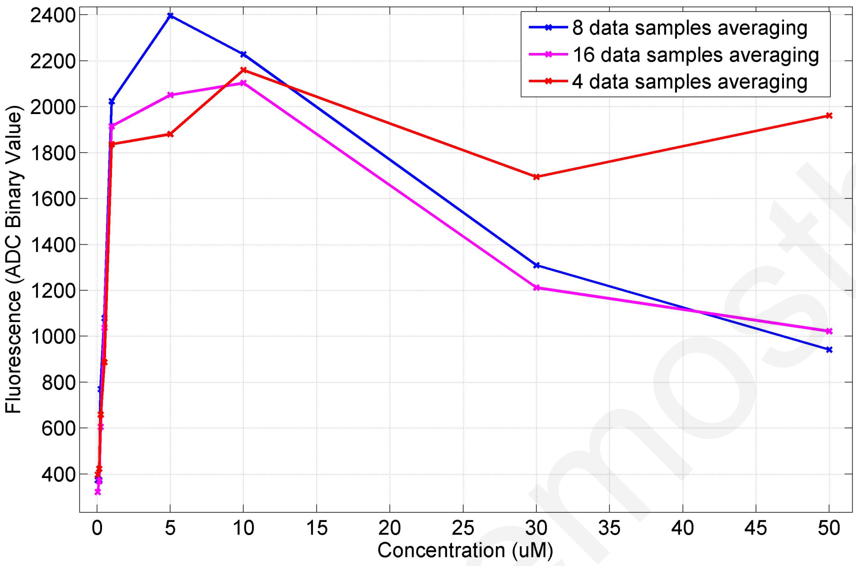

Figure 4.23: Fluorescence Vs. ICG concentrations with averaging of 4, 8 and 16 data samples.

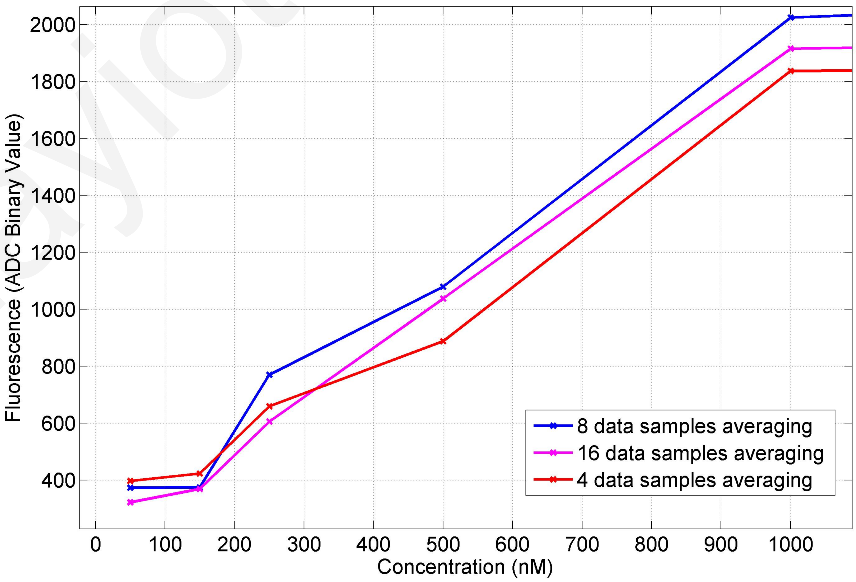

Figure 4.24: Zoomed-in results at lower ICG concentrations.

The averaging methodology of eight fluorescence data samples (N=8) was also implemented for different signal amplifications. Figures 4.25 to 4.30 show the results of fluorescence versus ICG concentrations under 0.15 V/nA, 0.2 V/nA and 0.27 V/nA amplifications respectively.

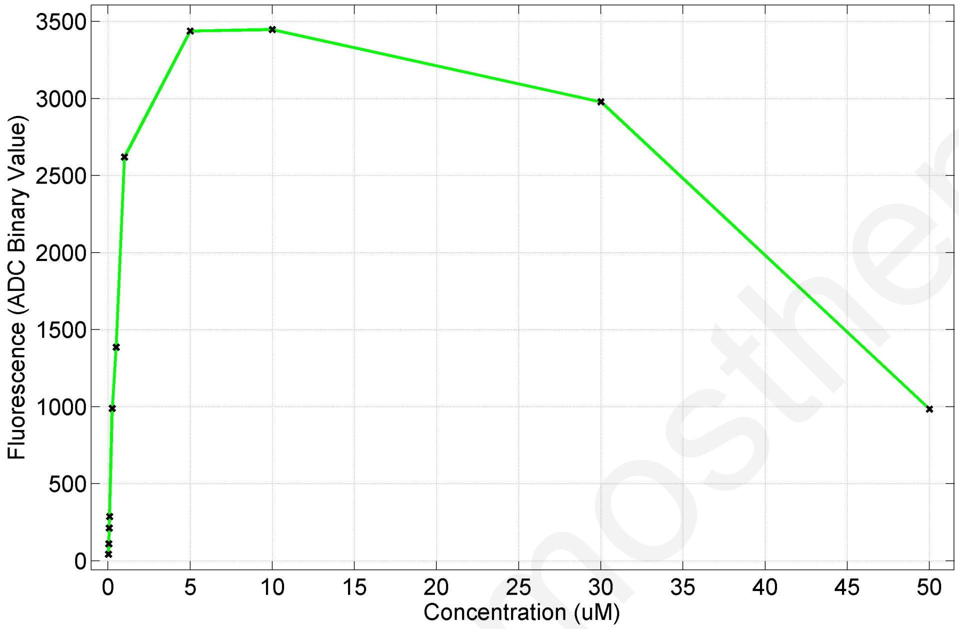

Figure 4.25: Fluorescence Vs. ICG concentrations under signal amplification with a 150 MΩ feedback resistor using the averaging-noise-reduction methodology (N=8).

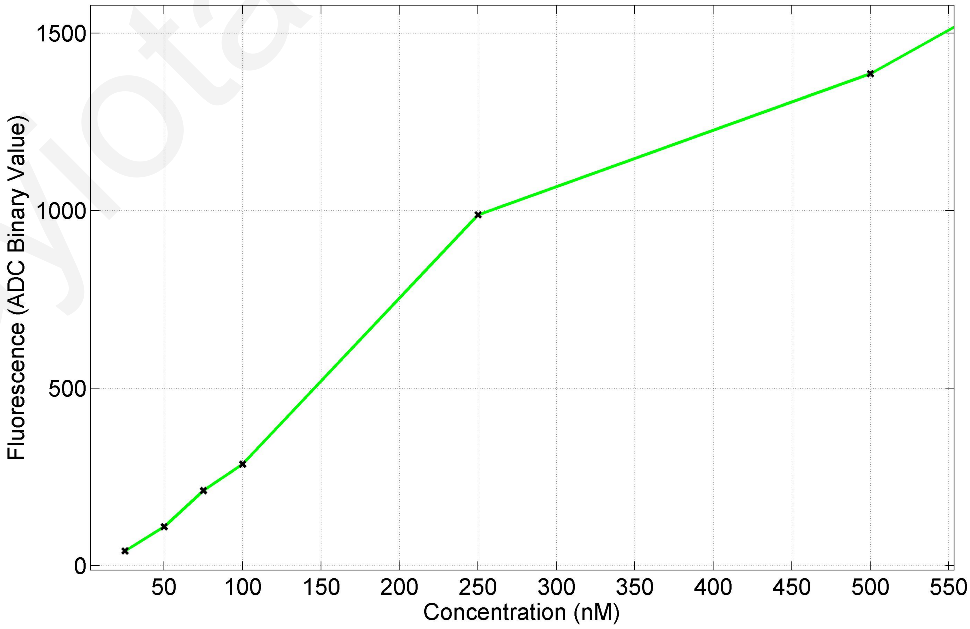

Figure 4.26: Zoomed-in results at lower ICG concentrations.

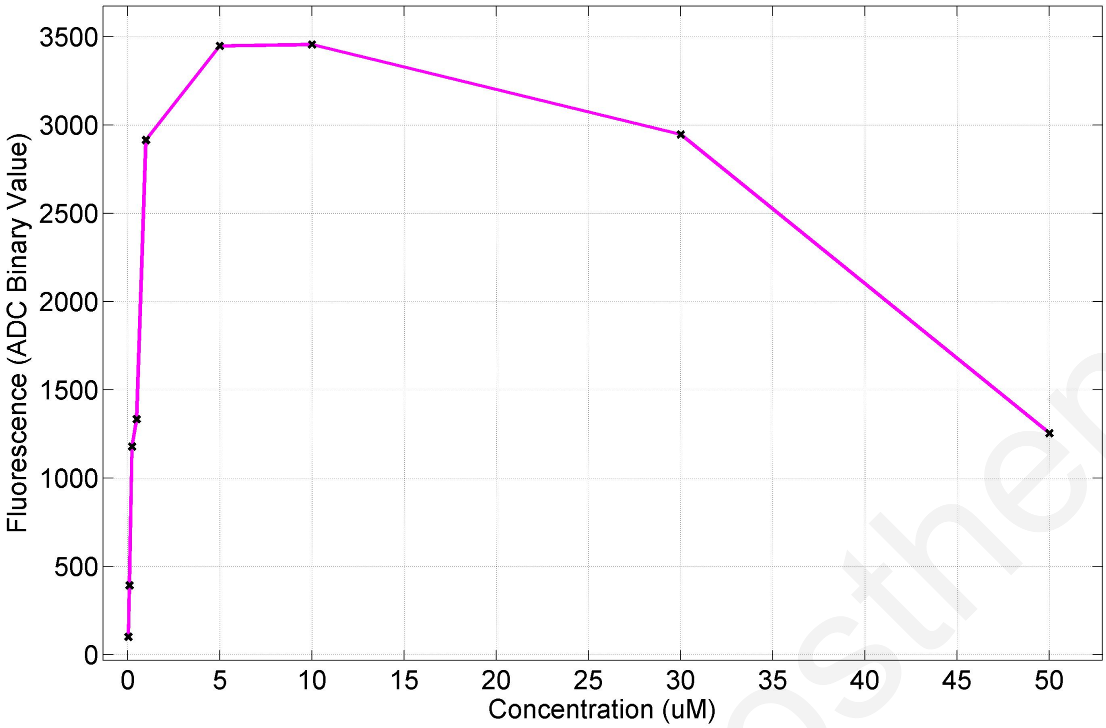

Figure 4.27: Fluorescence Vs. ICG concentrations under signal amplification with a 200 MΩ feedback resistor using the averaging-noise-reduction methodology (N=8).

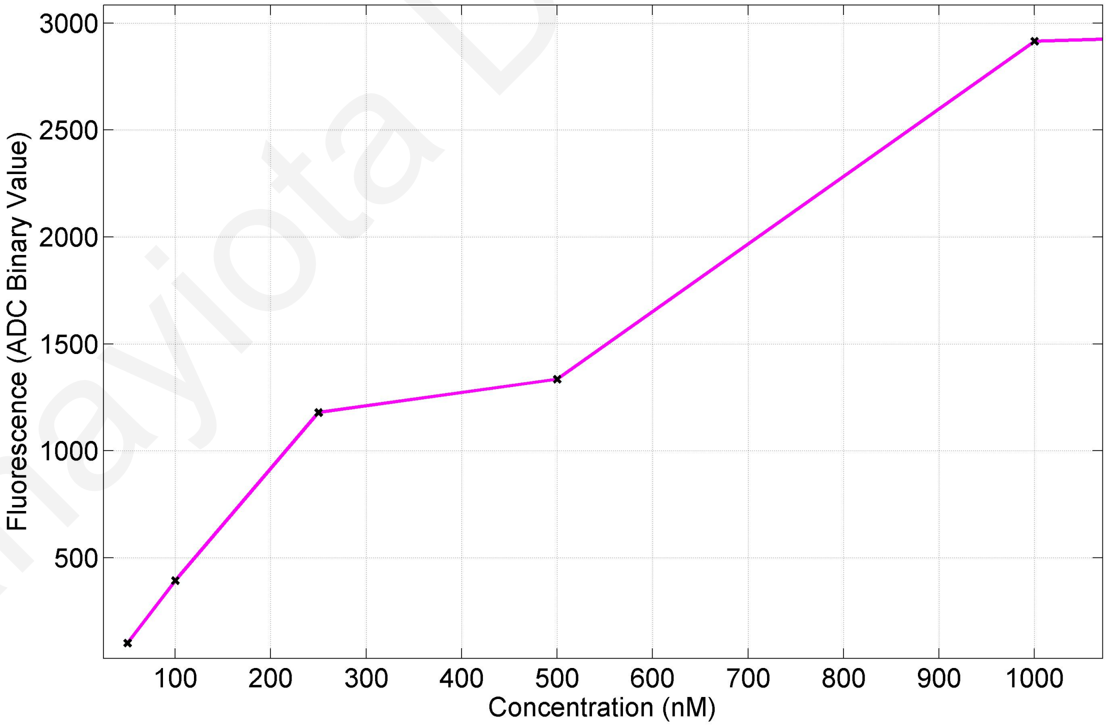

Figure 4.28: Zoomed-in results at lower ICG concentrations.

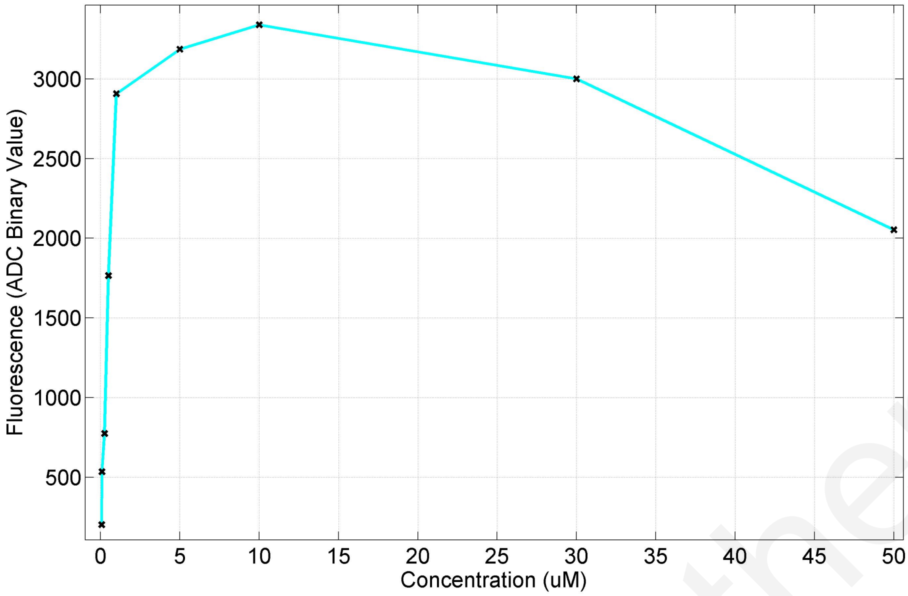

Figure 4.29: Fluorescence Vs. ICG concentrations under signal amplification with a 270 MΩ feedback resistor using the averaging-noise-reduction methodology (N=8).

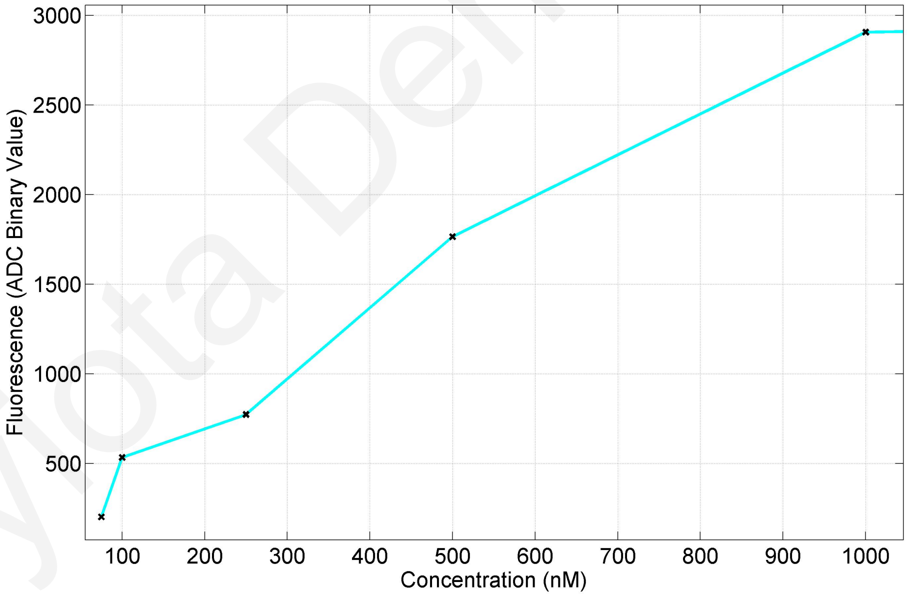

Figure 4.30: Zoomed-in results at lower ICG concentrations.

Therefore, it is verified that the system is able to detect different concentrations of ICG, with sensitivity at nanomolar range from 25 nM to 50 000 nM. In particular, the system is able to discriminate the two critical concentrations of 19 nM and 225 nM, which represent the healthy and cancerous cells respectively based on the calculations presented in section 2.3.

4.2.2.2 Ex-Vivo Experiments

The functionality of the capsule with the front-end optics structure was also tested in swine intestine tissue impregnated with ICG solution of different concentrations. ICG solution of 231 uM was prepared by dissolving 0.36 mg of ICG in 2 mL distilled water. Lower concentrations of 18 nM, 46 nM, 92 nM, 231 nM, 2.3 uM, 23 uM and 46 uM were prepared from the dilution of a portion of the main solution in distilled water, and were injected into swine intestine tissues. The last step may have further diluted the concentration, however we have assumed that this is negligible.

In the front-end optics structure, the excitation laser diode and the photodiode are placed side-by-side, as shown in Figure 4.31. In this configuration, we expect that the excitation light (785 nm), which is much more intense than the returned fluorescence intensity (790-860 nm), will be partially reflected from the capsule walls, as well as from the ICG-impregnated tissue sample. Nevertheless, it was shown that the long-pass filters integrated on the photodiodes, with cut-off at 800 nm, were sufficient for keeping this unwanted component at bay.

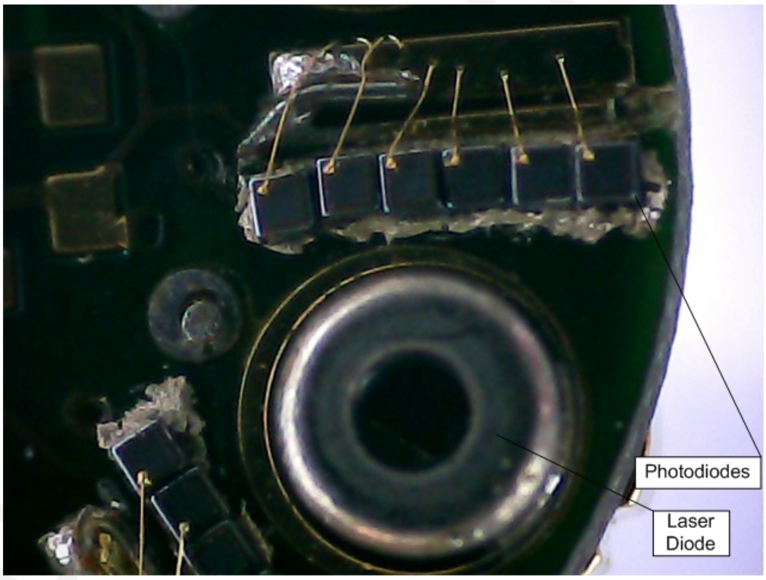

Figure 4.31: Front-end optics structure. The laser diode and the photodiode are in parallel.

As is shown in Figure 4.32, the system is able to discriminate between tissue of various ICG concentrations in the range of interest. Figure 4.34 provides similar results when photodiodes of lower sensitivity (smaller active area) were used. It is observed that fluorescent increases with increasing concentration in low-concentration region ($< 300nM$) while the emission strength decreases with the concentration in high-concentration region ($> 300nM$). The existence of emission strength maximum as a function of concentration is mainly a result of the re-absorption of emitted photons that never reach the detector [99]. Moreover, higher concentrations of 46 uM and 231 uM present even lower fluorescence, since they are not effectively excited by 785 nm light but with 708 nm wavelength (section 2.3).

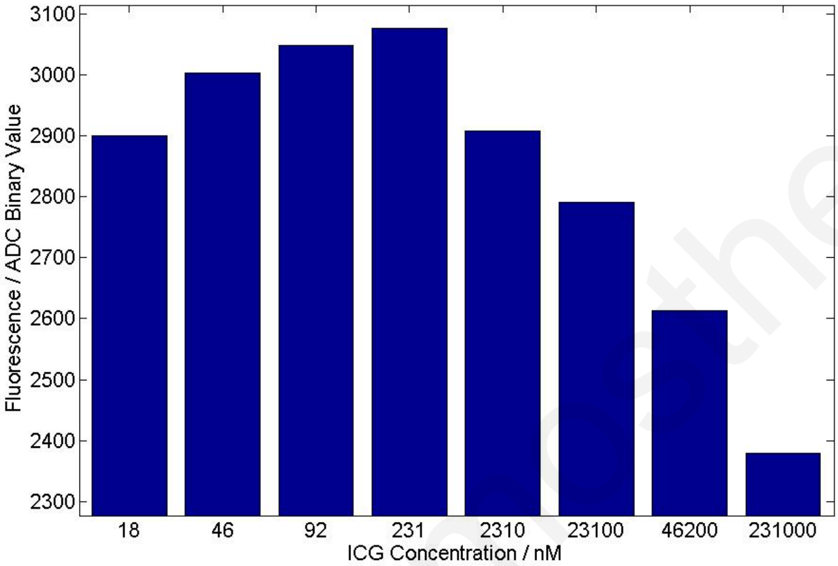

Figure 4.32: Discrimination, with the capsule system, of different concentrations of ICG impregnated in swine intestine tissue.

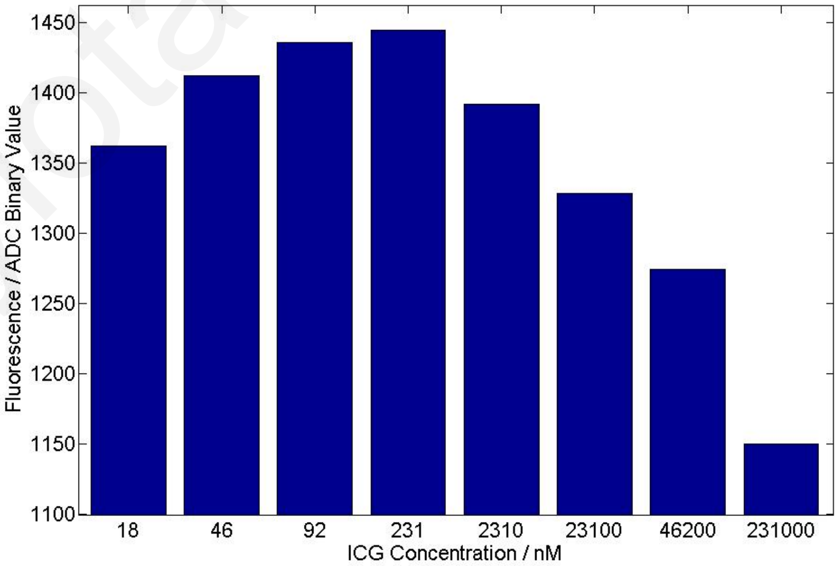

Figure 4.33: Discrimination, with lower-sensitivity photodiodes, of different concentrations of ICG impregnated in swine intestine tissue.

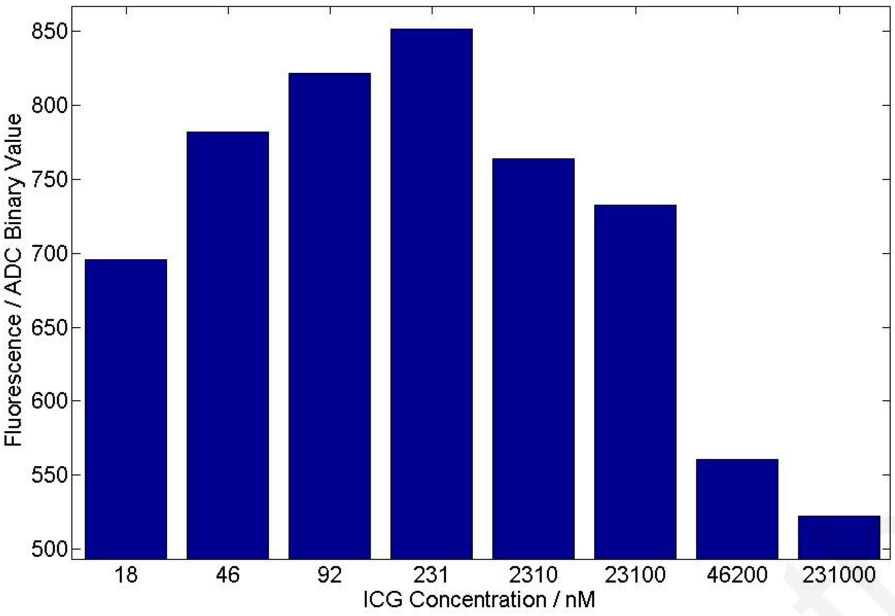

Figure 4.34: Discrimination, with lower-sensitivity photodiodes, of different concentrations of ICG impregnated in swine intestine tissue.

Another set of experiments, test the screening ability of the system (Figure 4.35a) on a long part of swine intestine that was impregnated with ICG of different concentrations. The capsule scanned the walls of the intestine through a screening procedure with an average speed of 1 mm/sec (Figure 4.35b). This is the average speed that food moves in the intestine. Figures 4.36 and 4.37 show the ability of the system to discriminate the different intestine-impregnated ICG concentrations through the screening procedure.

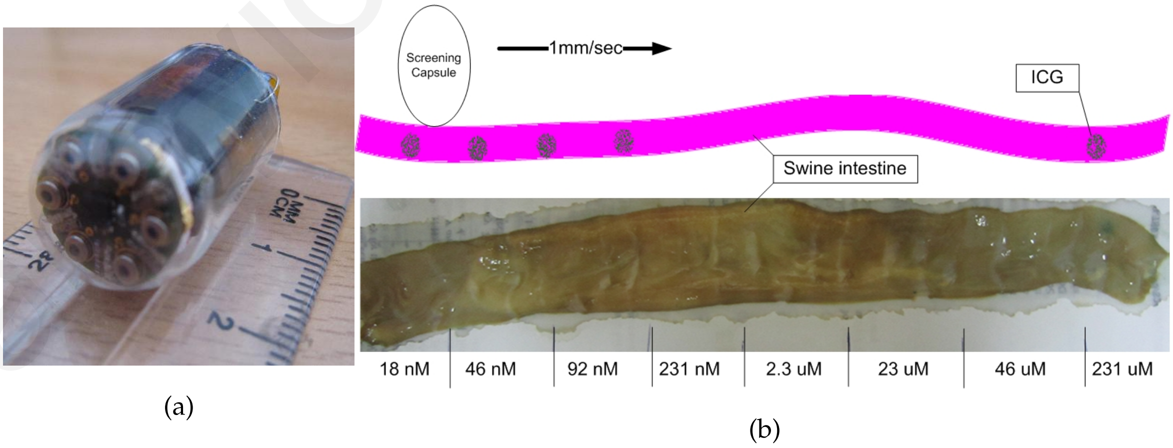

(a)

(b)

Figure 4.35: a) The Completed Ingestible Microcancer Detection Capsule, b) Screening of swine intestine that was impregnated with ICG of different concentrations.

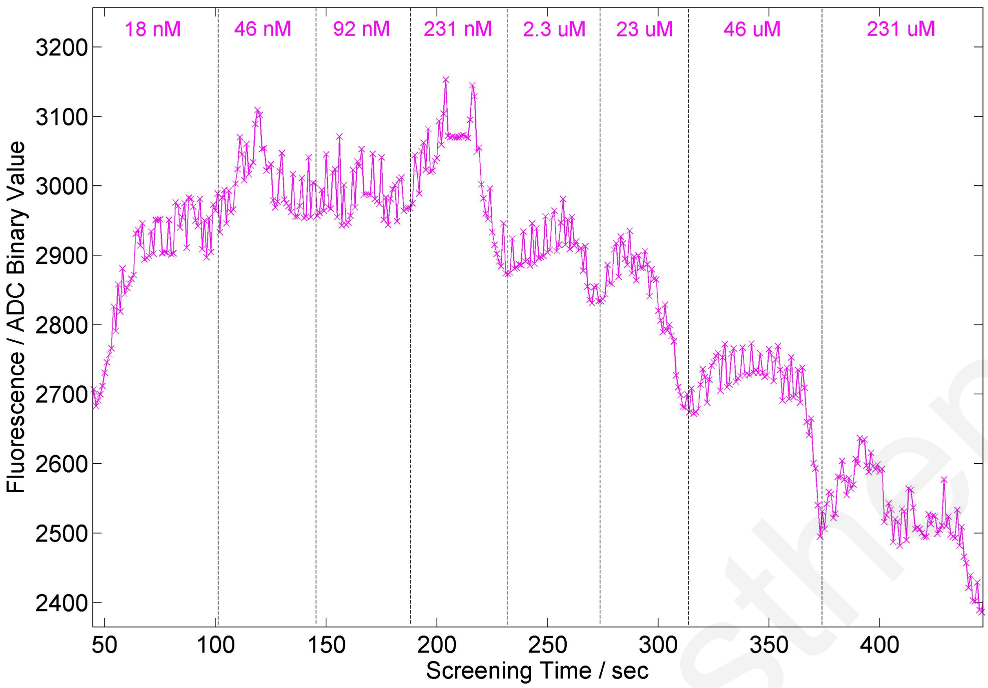

Figure 4.36: ICG Concentrations Discrimination by Screening the Swine Intestine.

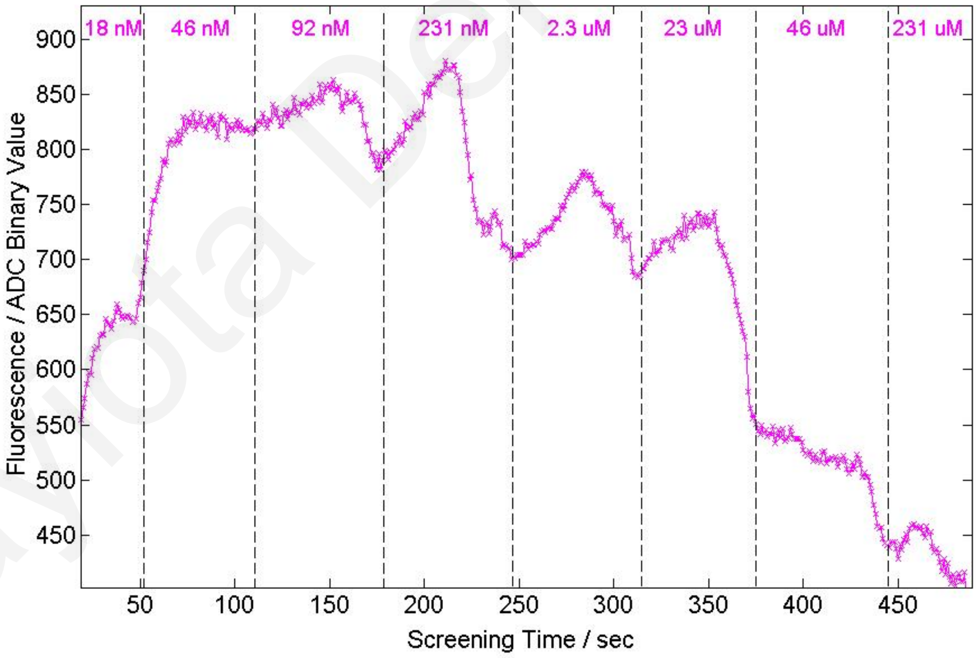

Figure 4.37: ICG Concentrations Discrimination by Screening the Swine Intestine - Usage of lower-sensitivity photodiode.

Next, a swine intestine was impregnated with only 231 nM ICG at two different places, at a distance to each other. The intestine was again screened with an average speed of 1 mm/sec. Time markers 45-95 s and 170-225 s were noted when the capsule was screening the ICG-injected areas. The results in Figures 4.38 and 4.39 show the fluorescence detection of the two areas in the intestine, around the noted time markers.

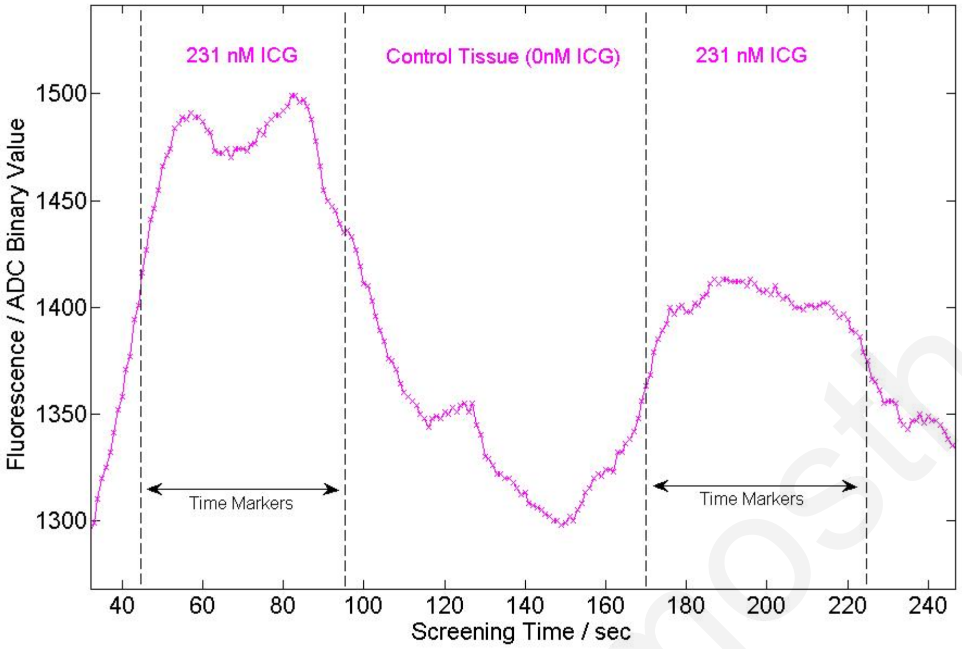

Figure 4.38: Detection of ICG-injected areas on the walls of the swine's intestine.

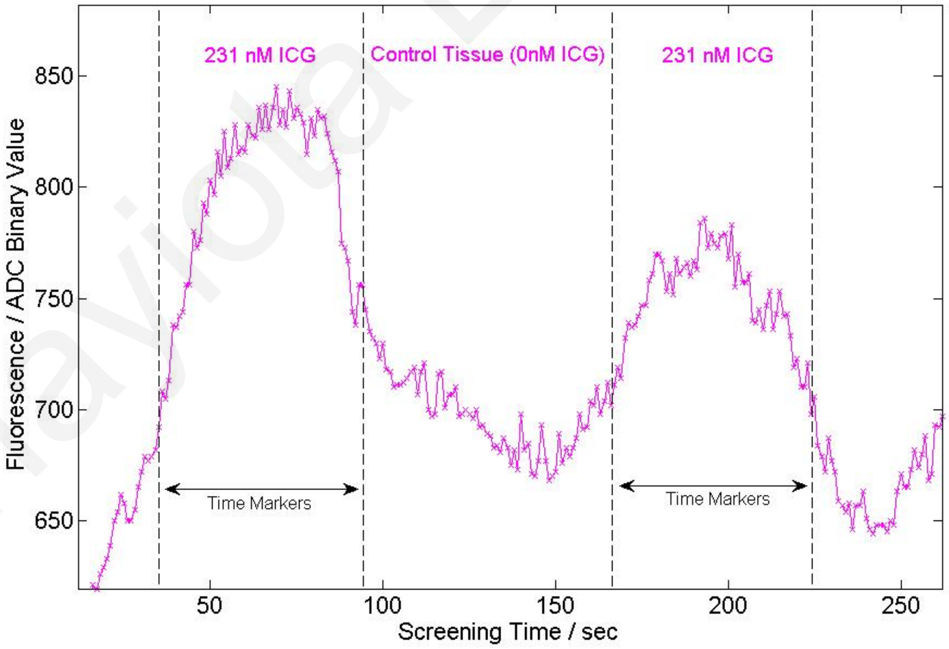

Figure 4.39: Fluorescence detection of the ICG-injected areas on the swine's intestine - Usage of lower-sensitivity photodiode.

4.3 Advanced Features

4.3.1 Sampling Rate and Power Management

A methodology is proposed for regulating the data-acquisition sampling rate of the cancer screening capsule and of any endoscopic capsule in general [21]. The proposed method utilizes acceleration information to increase the sampling rate during rapid movement. In order to test this method a module was designed, which allows a quick implementation of the methodology. This module consisted of a custom-built PCB, which interfaced with an Opal Kelly FPGA board, in addition to other components. The whole setup was tested on a Motion Dynamic simulator. The proposed methodology ensures a thorough scan of the G.I. tract, whilst consuming less power than the fixed sampling rate used in existing capsules.

Currently, commercially available capsules have a fixed image acquisition rate of approximately 2-18 images/sec in order to be able capture the entire G.I. tract, by providing uniform temporally-distributed images. As a result, current capsule technology is either very power hungry, when a high sampling rate is used, or it does not adequately scan all sections of the intestine, when a low sampling rate is used. Key constraints related to battery capacity and size are: a) the capsule needs to be small enough to be easily swallowed i.e. <1.5cm diameter and b) imaging process must last 8 hours or more.

Capsules are pushed through the intestine via peristalsis. Peristalsis generally occurs over short segments (approximately every 6 cm) and propagates at a rate of 1–2 cm/min [37]. For this reason, current commercial capsules acquire images with a fixed image acquisition rate. PillCam SB (the first endoscopic capsule by Given Imaging Ltd), Olympus EndoCapsule and the SSSA Capsule provide an acquisition rate of 2 images/sec. The next generation of capsules by Given Image has a higher frame rate of 4 images/sec. A magnetically propelled capsule developed by Olympus Company uses an inductive external power source, allowing an image acquisition rate of up to 5 images/sec. Inductively powered systems are more cumbersome, since the patient needs to wear a ‘belt’ carrying relatively heavy external batteries and the recording device. Since a capsule travels relatively quickly through the esophagus, specialized capsules are used to scan the esophageal tract at higher sampling rates, for example, the PillCam ESO and ESO2 sample at 14 images/sec and

18 images/sec respectively. Their battery, however, will only last for 30 minutes, thus requiring a second capsule to scan the rest of the GI tract. The capsule developed by the Norika Project Team incorporates a rotating CCD camera to enable image acquisition at different positions for the whole GI tract with capture rate of up to 30 images/sec. That capsule is also externally powered and the diagnostic system includes heavy peripheral equipment such as an external controller, a transmitter vest and a workstation [64], [63].

If one considers that a capsule is stationary most of the time, and occasionally moves forward during peristalsis, one can deduce that a constant image acquisition rate of 2–5 image/sec is not optimal. Furthermore, it is possible for the capsule to rapidly shoot forward, as the intestine contracts around the capsule. In the case of rapid movement, available capsules may not image certain sections of the GI tract, which could be a problem if these are diseased. Even though using a constant high sampling rate, would give sufficient coverage. This is not practical since most capsules rely on silver-oxide watch batteries with limited capacity, e.g. two SR45 batteries in series can provide a 3 V supply with around 60 mAh capacity. Other battery types with larger capacities are not approved for clinical use.

In the following sections, a novel solution is presented that overcomes the disadvantages of the above-mentioned systems by using acceleration information to change the sampling rate during rapid movements. This functionality can increase the reliability of the endoscopic capsules and reduce the power consumption of image capturing.

4.3.1.1 Variable Sampling Rate Proof-of-Concept Test Hardware

A hardware platform was designed for quick and flexible testing of the underlying principles before these were applied to the capsule system (Circuit Schematic and PCB - Appendix A). Many of the components that are included in the test platform may not be needed in an autonomous capsule; however, these were included to allow exploration of various options. Figure 4.40 shows a photograph of the experimentation platform module, which consists of: (1) a three - axis accelerometer, with one of its axes aligned in the direction of the movement, and (2) an Opal Kelly board that allows quick testing of VHDL code that implements signal-processing algorithms and communication protocols to interface to non-volatile memory and the accelerometer. Furthermore, the Opal Kelly board has a USB interface that allows quick interfacing to a PC for debugging purposes.

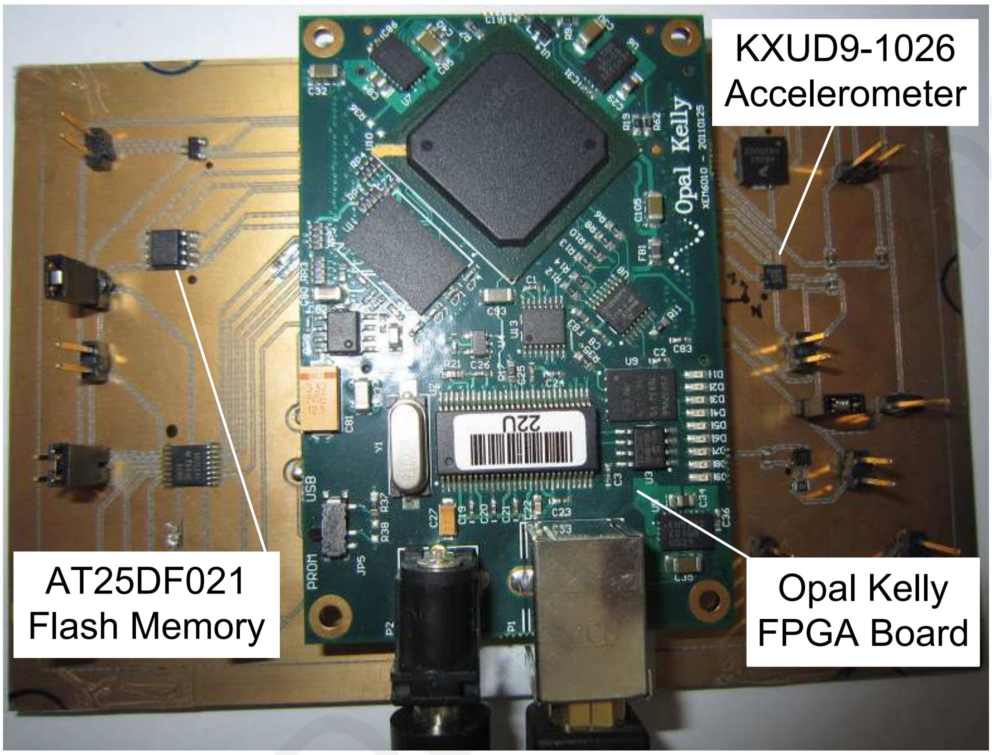

Figure 4.40: Hardware Implementation.

The FPGA code consists of various modules presented in Figure 4.41. As shown in the flowchart, the accelerometer provides x-axis data every 10 ms to a signal-processing system (SPS) through an SPI bus link. The SPS calculates the modulus of changes in acceleration, by subtracting the previous and current acceleration value and then averages this signal through an exponentially-weighted moving-average filter [22], to reduce the effect of noise. The SPS output is then input to a threshold-decision unit, which determines, through a multiplexer, if a faster sampling rate of 10 circular scans per second (csps) should be used or if the slower sampling rate of 1 csps is appropriate. In more complex implementations, one can choose to have intermediate sampling rates for different capsule speeds. At the same time the sampling clock and the acceleration data are transmitted through the SPI bus to be stored on a non-volatile flash memory for testing purposes. The same VHDL code was eventually used to store the data on the non-volatile flash memory.

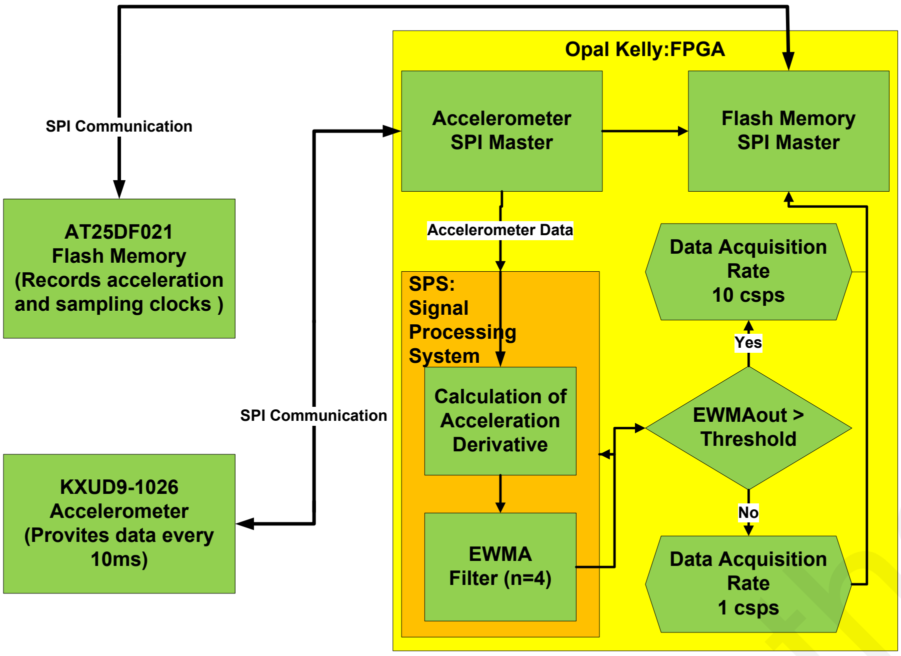

Figure 4.41: Hardware Flowchart.

4.3.1.2 Functionality Testing

The module was tested on a single-axis rate table TES-3T (Figure 4.42), which can be programmed to rotate at one-axis while simultaneously being manually tilted to any angle. The rate table was used to simulate capsule movement in the heavily convoluted intestine. Rate table control and/or recording of its current position (deg) and velocity (deg/sec) is performed via a PC running National Instruments LabVIEW.

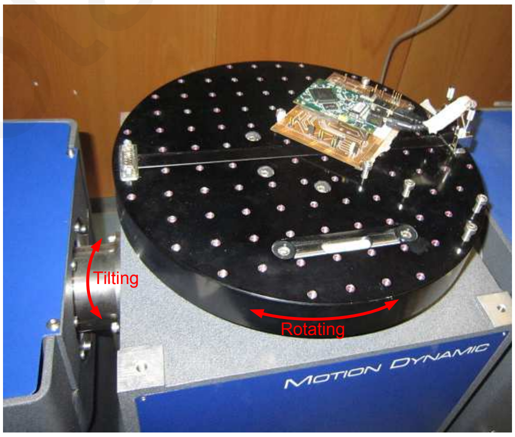

Figure 4.42: Single-Axis Rate Table TES-3T.

Figure 4.43 and 4.44 present the results from the execution of a manual displacement of 25°. The velocity increases and decreases within a time frame of 200ms, whilst the measured acceleration represents the derivative of velocity.

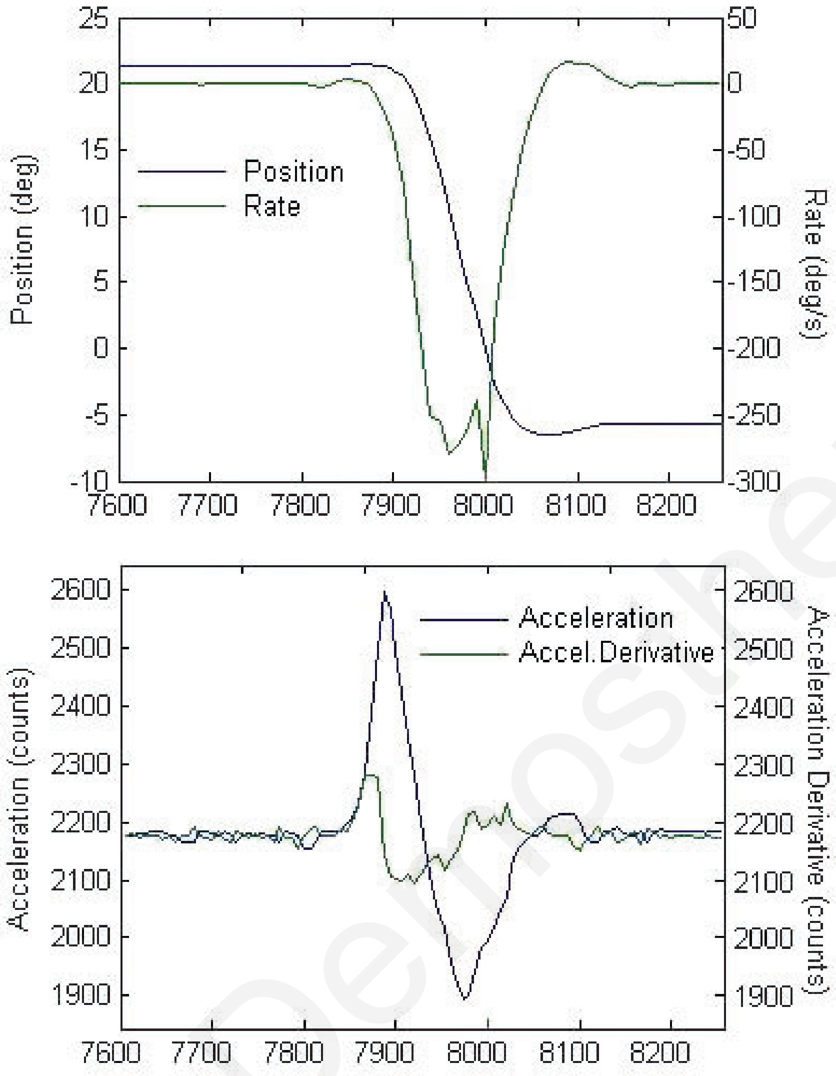

Figure 4.43: Position, Velocity, Acceleration and Acceleration Derivative results of a 25° manual displacement.

Figure 4.44 shows the processed acceleration derivative, the filtered output and the sampling clock, as executed in real-time on the FPGA. The usage of a low-pass filter avoids false triggering leading to an unnecessary higher sampling rate, whilst the capsule is almost stationary.

The output of the accelerometer consists of two components, one arising from the effect of gravity g and the other from the actual movement of the capsule a_x. The effect of gravity depends on the orientation of the capsule with respect to the gravitational field i.e. $k = sin\theta$, where θ is the angle between the accelerometer axis and the surface of the earth. Hence,

$$A_x = a_x \pm k.g \quad k < 1 \tag{4.3}$$

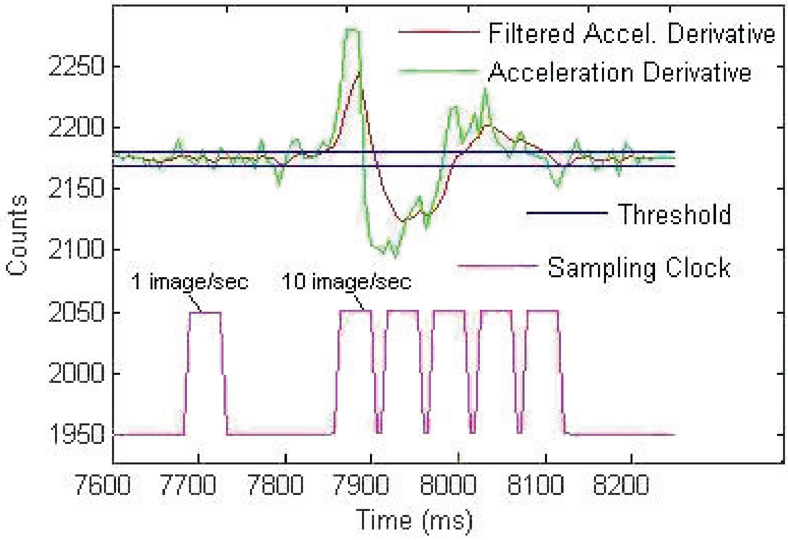

Figure 4.44: Acceleration Derivative, Filtered Acceleration Derivative, Threshold value and Sampling Clock results of actual 25° manual displacement.

It is important to ensure that the algorithm modulating the data sampling rate is relatively unaffected by the gravitational component. Assuming that the tilting action of the endoscopic capsule is a slow event, this is not detectable by using the derivative of acceleration. Figure 4.45 shows measured results illustrating that the above methodology is robust to the effect of gravity and slow changes in capsule orientation. Also, Figure 4.46 shows the result of testing the same system in oscillation mode (2 Hz), for different swing amplitudes, i.e. 10°, 20°, 30°, 40° and 50°. The system behaves as expected for both short and relatively long rapid movements.

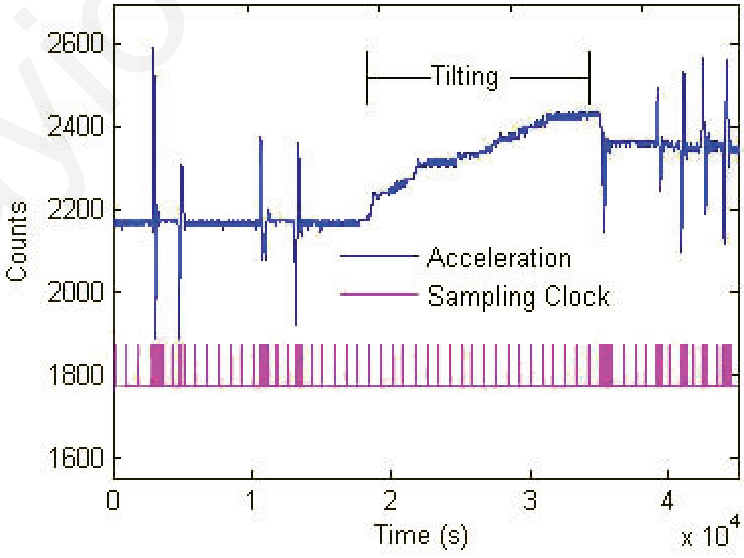

Figure 4.45: Acceleration and Sampling Clock results of tilt and sudden movements.

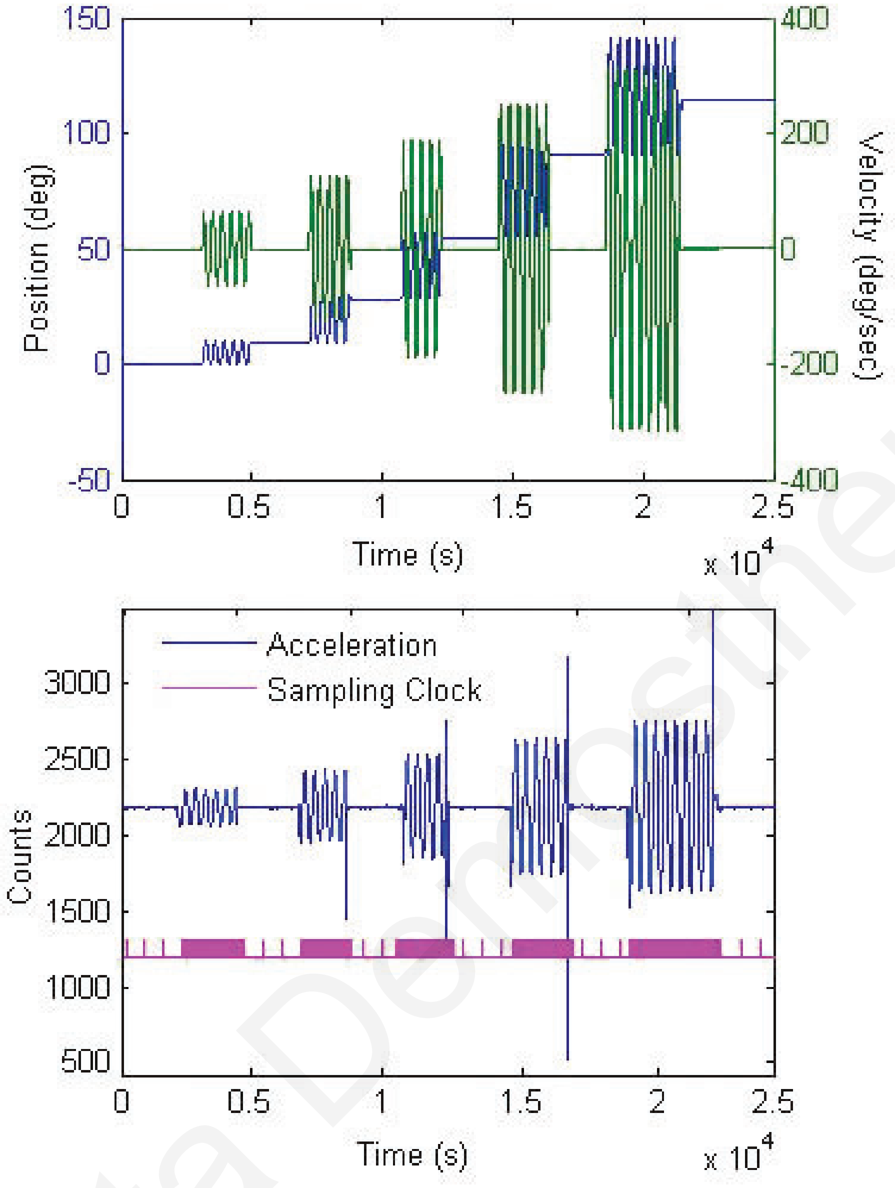

Figure 4.46: Position, Velocity, Acceleration and Sampling Clock results of 2Hz oscillations with amplitudes 10˚,20˚,30˚,40˚,50˚.

4.3.1.3 Current Consumption at Fixed and Variable Sampling Rate

Peristalsis has a rate of 10 cycles/min and propagates at a rate of 1-2 cm/min [37]. During fast movements an increased sampling rate of 10 circular scans per second (csps) is used. If we assume that this rate is only required for $1/8^{ths}$ of the time, 1 circular scan per second would be sufficient for the remaining time, as the peristalsis propagation is around 2 mm/peristaltic-cycle. Then, the equivalent sampling rate for this capsule is $(1/8)10csps + (7/8) \times 1csps \approx 2csps$. Thus, the sampling rate of 2 csps corresponds to 12 fluorescence data per second. Respectively, 36 fluorescence data per second, corresponds to a screening capsule with fixed sampling rate of 6 csps. Thus, the total power consumption of a constant rate capsule would be three times more, compared to a variable sampling rate capsule.

The current consumption analysis of a complete system with a variable sampling rate, is shown in Table 4.2. Power cycling of components allows the reduction of the total power, without affecting the performance. Analog to digital conversion requires approximately 0.5 ms to complete, thus conversion of 12 fluorescence data each with eight values for averaging, requires $48/1000^{ths}$ of a second corresponding to 0.96 uA of current consumption. For the remainder of the time, the ADC (AD7466) operates on sleep mode with lower current consumption at 0.1 uA. Similarly, the flash memory (AT25DF081A) requires approximately $12/1000^{ths}$ of a second to store twelve data of sixteen bits with current consumption along programming operation at 10 mA. However, in sleep mode it consumes 25 uA. In addition, the fluorescence-amplification circuitry runs simultaneously with the excitation, which lasts approximately 5 ms. Thus the 5 V charge pump (LTC3204-5) and the voltage regulator (AS1374a) that power up the amplifiers (OPA2381) are in operation mode for a period of $60/1000^{ths}$ of a second, consuming a current of 6.6 uA. While the amplifiers are in operating mode, they consume a current of 48 uA. Higher current consumption occurs when the laser diodes switch on, requiring an intermittent constant current of 100 mA.The total current consumption of the LDs, with a pulse duration of 5 ms and average sampling rate 2 csps is approximately 6 mA. At the same time the constant current source (LM317L-N), that biases the laser diodes, works also for a period of $60/1000^{ths}$ of a second, consuming 3 uA. The rest of the devices; the analog multiplexer (ISL84781), the voltage reference that powers up the CPLD and all the peripherals (AS1374b), the CPLD, the oscillator, the hall sensor (AH1802) and the accelerometer (LIS3DH), are in continuous operation with a current consumption at approximately 107.95 uA. The total current consumption was calculated around 6.3 mA, which means that the system can run for almost 9.5 hours with silver-oxide SR45 batteries of 60 mAh capacity (mean value screening duration of the gastrointestinal track is around 8 hours). Respectively, the total current consumption for the fixed sampling rate capsule, is around 18,9 mA and can operate for only 3.2 hours. The same analysis is provided in Table 4.3 for the first generation prototype system.

Table 4.2: Current Consumption Analysis of Second Generation Capsule

Component	Operating Mode	Sleep/Shutdown Mode	Current Consumption with Sampling Rate 2csps
AT25DF081A	(2*6*1ms/1000ms)*10mA=120uA	(988ms/1000ms)*25uA= 24.7uA	144.7uA
AD7466	(2*6*8*0.5ms/1000ms)*20uA=0.96uA	(952ms/1000ms)*0.1uA= 0.1uA	1.06uA
LTC3204-5	(2*6*5ms/1000ms)*60uA=3.6uA	(940ms/1000ms)*1uA= 0.94uA	4.54uA
AS1374(a)	(2*6*5ms/1000ms)*50uA=3uA	(940ms/1000ms)*2uA= 1.9uA	4.9uA
OPA2381	(2*6*5ms/1000ms)*0.8mA=48uA	-	48uA
Laser Diodes	(2*6*5ms/1000ms)*100mA=6000uA	-	6000uA
LM317L-N	(2*6*5ms/1000ms)*50uA=3uA	-	3uA
ISL84781	0.05uA	-	0.05uA
AS1374(b)	50uA	-	50uA
CPLD	50uA(at 32kHz)	-	50uA
LIS3DH	2uA	-	2uA
Oscillator	0.9uA	-	0.9uA
AH1802	5uA	-	5uA
Total Current Consumption			6314.15uA

Table 4.3: Current Consumption Analysis of First Generation Capsule

Component	Operating Mode	Sleep/Shutdown Mode	Current Consumption (2csps)
AT25DF021	(12*1ms/1000ms)*12mA=144uA	(988ms/1000ms)*51uA= 50.39uA	194.39uA
ADS1146	(12*0.7ms/1000ms)*420uA=3.53uA	(991.8ms/1000ms)*0.3uA= 0.29uA	3.83uA
MAX1853	(12*5ms/1000ms)*165uA=9.9uA	(940ms/1000ms)*0.5uA= 0.47uA	10.37uA
MCP1253	(12*5ms/1000ms)*60uA=3.6uA	(940ms/1000ms)*0.1uA= 0.09uA	3.69uA
OPA129UE4	(12*5ms/1000ms)*1.2mA=86.4uA	-	86.4uA
Laser Diodes	(12*5ms/1000ms)*100mA=6000uA	-	6000uA
CPLD	50uA(at 32kHz)	-	50uA
REF3320	3.9uA	-	3.9uA
KXUD9	220uA	-	220uA
Oscillator	1.5uA	-	1.5uA
LM317MD	50uA	-	50uA
SN74LV4051AT	20uA	-	20uA
TPS70151	230uA	-	230uA
AH1802	5uA	-	5uA
Total Current Consumption			6879.08uA

In conclusion, it has been shown that the variable sampling rate methodology can save capsule power, whilst reducing the risk of omitting images in segments of the intestine during which the capsule travels faster than normal. Calculations show that the proposed method will enable a capsule to consume almost three time less power than the fixed sampling rate capsule, whilst eliminating false triggering of the faster sampling rate, by noise or by gravitational acceleration.

4.3.2 Memory-Efficient Storage Management

Regulating the ten-fold increase in the data-acquisition sampling rate during sudden movements of the capsule, poses some storage limitation issues. The higher the sampling rate, the larger the amount of data samples that have to be stored in the internal memory. This issue can be overcome either by replacing the flash memory with a higher capacity one, or by managing the collected data in a way that will decrease the amount of stored data. Here, the latter is chosen and a storage management methodology is presented that uses spike detection procedure for the storage of a time-stamp information that indicates a detection of cancer in the small intestine. Considering the cancerous affected area as an intense fluorescence signal in a noisy background (Figure 4.47), then a general procedure of spike detection can be used for the detection of cancerous cells.

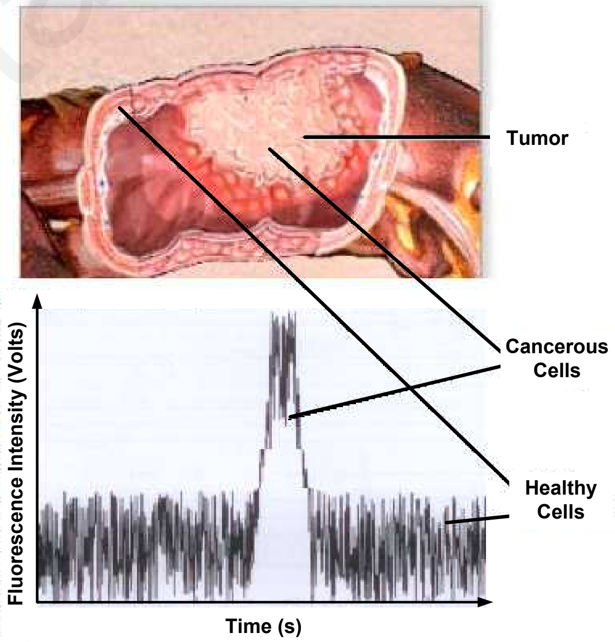

Figure 4.47: Correlation of cancer with a spike voltage.

The proposed methodology follows a number of steps, which are shown in Figure 4.48. The digitised fluorescence signal is driven through a low pass filter that removes the noisy background. The filtered data is subtracted from the current value and the absolute value result is compared with a threshold value. Detection then takes place through threshold crossing. If the result is higher than the threshold, then a detection is made and a time-stamp value is stored to the memory. The utilisation of this strategy only stores the pertinent data in the memory by providing the time of when an increased level of fluorescence was detected above the background average or a predetermined threshold.

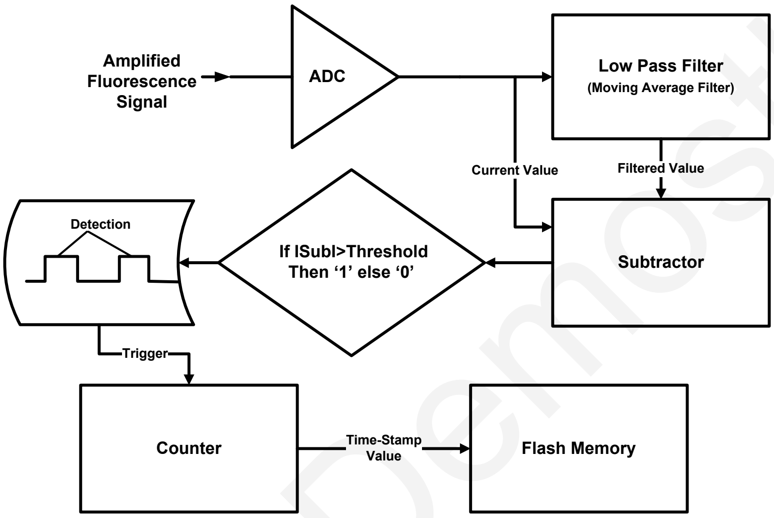

Figure 4.48: Basic steps for spike detection.

The following sections focus on the design of an appropriate, hardware-efficient, digital low pass filter that can be used in the screening capsule. More specifically, a module is presented that implements a particular class of moving average filters, the Exponential Weighted Moving Average (EWMA) filter, which is compared to a regular moving average filter (MA).

4.3.2.1 Basic Moving Average Filter

The Moving Average (MA) filter is one of the most widely used digital filters [19]. The MA filter replaces the current sample with the average value of the latest n samples of a data sequence. Its mathematical expression at any instant i is given by:

$$y_{MA_i} = \frac{1}{n}\sum_{j=0}^{n-1} x_{i-j} \qquad i \geq n-1 \tag{4.4}$$

where x_{i-j} is the input signal, y_{MA_i} is the output signal, i.e. the moving average, and n is the number of points considered in the average. Such a filter is useful for reducing random noise in a signal by attenuating out-of-band noise. This is applicable for the detection of action potentials in a noisy background. It should be noted that in the basic MA filter described above the data points affect the average value equally.

The implementation of a regular Moving Average filter is shown in Figure 4.49 and represents the optimum hardware-efficient structure. After amplification, an ADC converts the fluorescence analog signal into a digital data sequence, which is sent to an adder/accumulator as well as to a n-FIFO register to keep track of the n latest samples of the input data. With every input sample that is added to the accumulator, an element (the oldest in the n-FIFO register) is removed from the sum. At startup the n-FIFO contains n zeros, so the average, which is at the output of the adder, is not valid until at least n samples have been loaded. From there on the oldest element is subtracted from the average and the newest one is added. The division by n is realized in each sample by having bit shifting by direct wire connections. Thus, n must be an integer power of 2. So for $n = 2, 4, 8 \ldots, 2^{th}$ the division is realized correspondingly with $1, 2, 3 \ldots, m$ bits shift to the right. Additionally, performing the division before the addition prevents an overflow in the sum result.

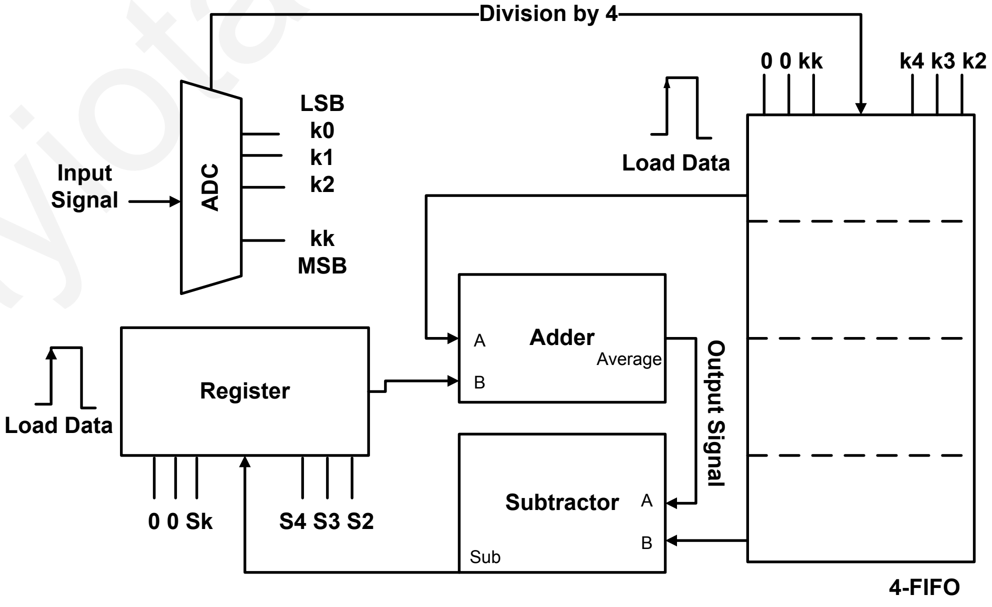

Figure 4.49: The minimal hardware implementation of a MA filter (with n=4).

One can see that the size of the FIFO increases with the number of points, n, in the average, hence the MA architecture becomes less hardware-efficient for lower cut-off frequencies. This is where a hardware-efficient low pass filter design is needed that is compact enough to be used in a future IC implementation of the capsule system or even to be programmed in the low capacity CPLD that is currently used on the system.

4.3.2.2 Proposed Moving Average Filter

In dynamic signals, the current value tends to better reflect the signal behaviour. A filter that places more emphasis on the most recent sample would, therefore, be more useful. Such a filter is the Exponential Weighted Moving Average filter (EWMA). This type of filter is similar to the regular MA filter, with the difference that more weight is given to more recent data. The EWMA is described by the following mathematical expression:

$$y_{EMA_i} = \left(\frac{n-1}{n}\right) y_{EMA_{i-1}} + \left(\frac{1}{n}\right) x_i \qquad i \geq 1 \tag{4.5}$$

where x_i is the input signal, y_{EMA_i} is the current output signal (weighted average), $y_{EMA_{i-1}}$ is the previous EWMA value, and n is a constant that determines the weight given to new points with respect to the prior average value. This is somewhat related to the number of points in a moving average. Furthermore, the above expression takes the following form for the computation of the EWMA of any $i+N$ steps, where N is an arbitrary point in future time:

$$y_{EMA_{i+N}} = \left(\frac{n-1}{n}\right)^{N+1} y_{EMA_{i-1}} + \sum_{j=0}^{N} \frac{(n-1)^{N-j}}{n^{N+1-j}} x_{i+j} \tag{4.6}$$

One can see that far in the future the previous average $y_{MA_{i-1}}$ will have almost no weight, whereas the most recent value x_{i+N}, will have the highest weighting. The choice of n will determine the rate of attenuation of the older values. The effect of different values of n on the filter response in time can be seen in Figure 4.50, in which the input stimulus is a noisy action potential. As n increases the output signal becomes smoother and responds slower, implying a lower cut-off frequency of the low-pass.

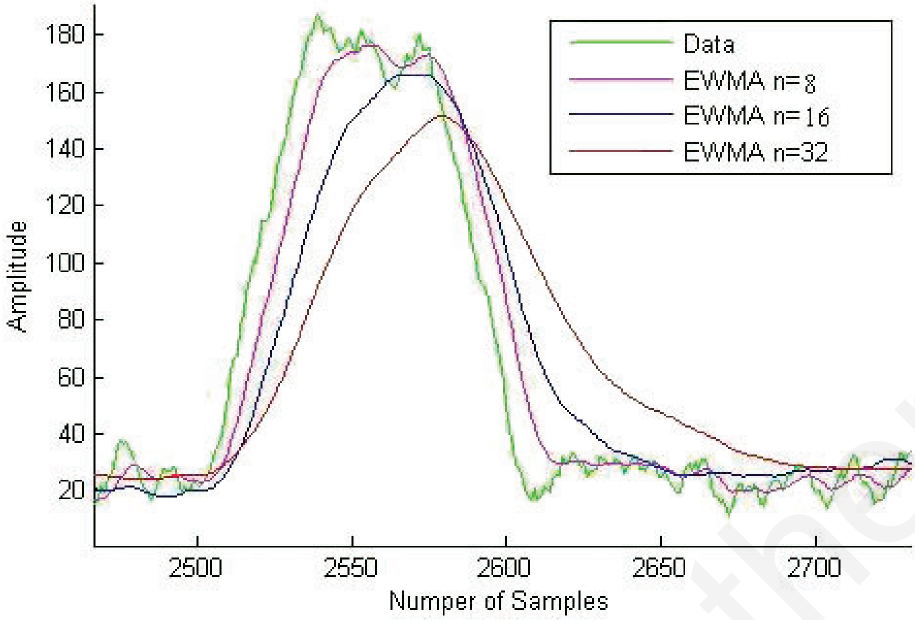

Figure 4.50: EWMA filters of different order.

The implementation of an exponential moving average filter is shown in Figure 4.51. Compared to the regular MA filter, and as can also be seen from the mathematical expression 4.5, only one addition and one multiplication is required. This is always the case, regardless of the number of the data points, *n*, considered. The division by *n* is not that important from the point of view of the hardware size since it is realized by bit shifting by connectivity. Thus, we are expecting the same restrictions

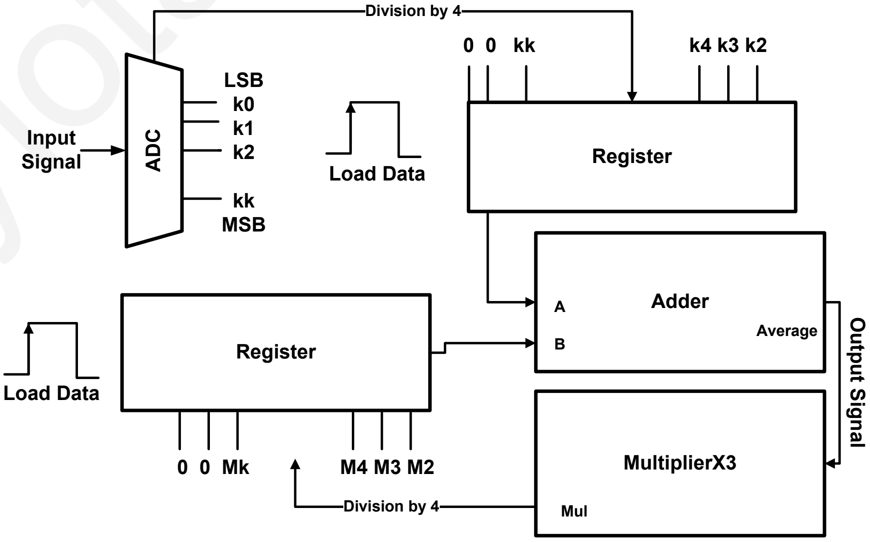

Figure 4.51: The implementation of a EWMA filter (with n=4).

as in the MA for the number n. It is already obvious that the hardware-non-efficient FIFO (in the MA technique) is replaced by a multiplier (in the EWMA technique) and, therefore, we can successfully implement a hardware-efficient lowpass filter. The function of the EWMA filter starts with a positive clock edge that triggers the import of the current sample and the previous EWMA value into the adder. The subsequent negative clock edge gives a new calculated EWMA in the output, while the multiplication takes place simultaneously and so prepares the next value that will be added in a new input sample.

4.3.2.3 Comparison of the Filters Behaviours and Size

For the capsule application there is an interest in the general frequency response and time domain behavior of the filters, as well as the area cost of the hardware. Therefore, a comparison of the EWMA and MA filters with respect to these characteristics is presented next.

Figure 4.52 shows the behavior of both filters for various n in the frequency domain. These simulations were conducted in Matlab by inputing sinusoidal signals at different frequencies and estimating the gain of the output with respect to the input. It can be seen that for the same n the regular MA filter has a larger corner frequency (-3dB gain) than the EWMA, however it has a sharper roll-off, which also includes significant stopband ripple. As the filter order increases: (1) a lower cut-

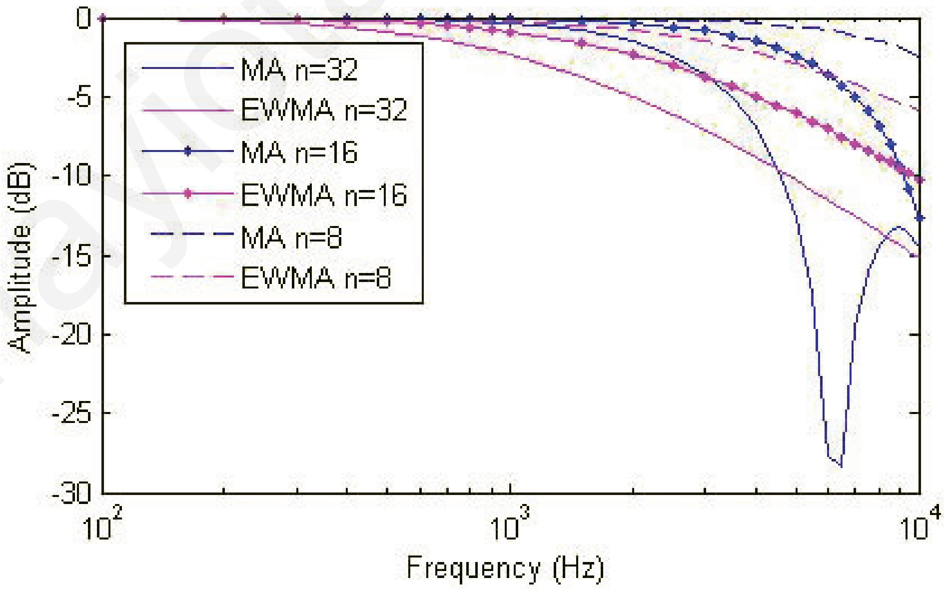

Figure 4.52: Frequency response of MA and EWMA filter of different order.

off frequency can be achieved (this effect is much stronger for the EWMA than the MA), and (2) the MA presents a faster roll-off behaviour compared to the EWMA. In addition, a similar cut-off frequency for a MA filter of order n can also be achieved with an EWMA filter of order $n/2$. So, both filters have almost the same behavior to low frequency input fluorescence signals.

Figure 4.53 shows the behaviour of both filters in the time domain, with an input signal of a noisy action potential. As expected, the behaviour of the EWMA filter of order $n/2$ was analogous to that of the MA filter of order n. Thus, both filters display similar behaviour with low frequency input fluorescence signals. Two cases of similar behaviour are presented: (1) case 1, which is the behaviour of MA with $n = 32$ and EWMA with $n = 16$; and (2) case 2 of MA with $n = 16$ and EWMA with $n = 8$.

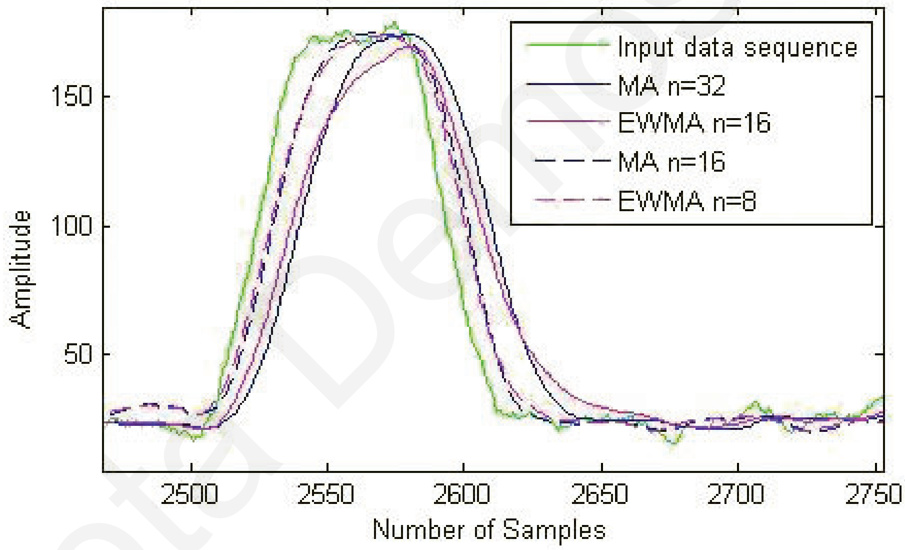

Figure 4.53: The behaviour of MA and EWMA in the time domain

The similarity between the time responses of an EWMA and a MA filter was assessed using the Pearson's Correlation Coefficient (PCC) on the curves of Figure 4.53. The PCC indicates the strength of a linear relationship between variables and is obtained through the following formula:

$$r_{xy} = \frac{\sum_{j=1}^{m} (x_i - \bar{x}) (y_i - \bar{y})}{(m-1) S_x S_y} \tag{4.7}$$

where x and y are the sample means of X and Y, S_x and S_y are the sample standard deviations of X and Y and m is the total number of the samples.

The results for the Pearson's Correlation Coefficient are shown in table 4.4. The Pearson correlation is +1 (-1) in the case of a perfect increasing (decreasing) linear relationship and the results that we have here seem to be very close to unity.

Table 4.4: Pearson's Correlation Coefficient

	Regular MA Filter	Exponential Weighted MA Filter	Pearson's Corr.Coeff.
1st case	n=32	n=16	0.9885
2nd case	n=16	n=8	0.9971

Another way to assess the dependence of these two averages was through a scatter plot, which shows the functional relationship of two quantities. Scatter plots for both cases are shown in Figure 4.54 and as we can see there is a linear relationship between MA with $n = 32$ and EWMA with $n = 16$, and respectively between MA with $n = 16$ and EWMA with $n = 8$.

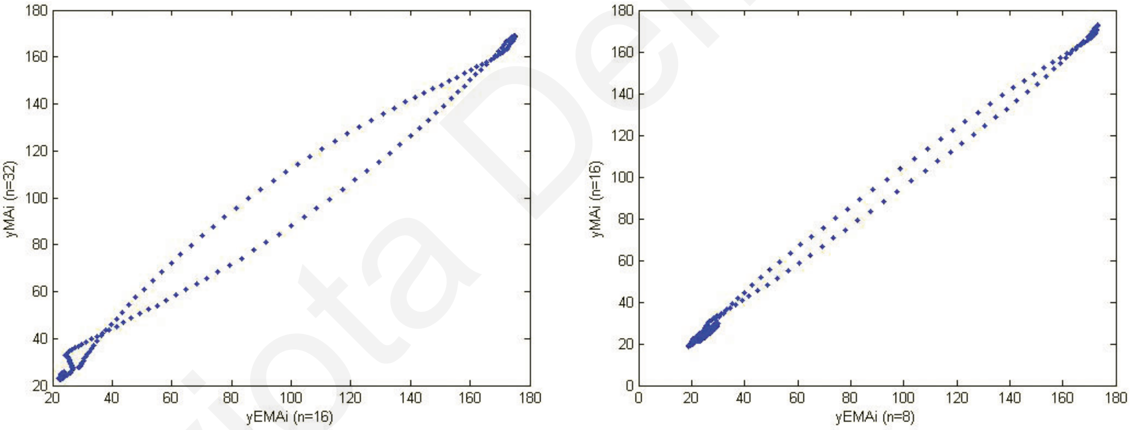

(a)

(b)

Figure 4.54: Scatter plots for a) case 1 and b) case 2

To summarize, the main conclusion is that an $n/2$ order EWMA filter can be used, which is more hardware-efficient than a MA filter with n points in the average and which has similar behaviour in the time domain and still can provide spike voltage detection.

Generally digital circuits can use the minimum device sizes, so in order to compare the hardware size (implementation efficiency) a transistor count for both filter types was performed. Assuming that the input signal is converted to samples with

8 bit sampling precision and knowing that 1 bit adder can be constructed with at least ten transistors [66], and a 1 bit register also with ten transistors (which is the D latch with transmission gate) then the number of transistors that are needed for the above two cases can be shown analytically in table 4.5. Therefore, it seems that the EWMA filter is almost 85% more hardware-efficient than the MA filter, which is a considerable reduction.

Table 4.5: Hardware Comparison

1^{st} case	Regular MA Filter n=32	Transistor Number	Exponential Weighted MA Filter n=16	Transistor Number
Different Hardware Parts	32-FIFO and Subtractor	2656	Multiplier*15 and Register	320
Percentage		100%		12%

2^{st} case	Regular MA Filter n=16	Transistor Number	Exponential Weighted MA Filter n=8	Transistor Number
Different Hardware Parts	16-FIFO and Subtractor	1376	Multiplier*7 and Register	240
Percentage		100%		17.4%

4.3.2.4 Hardware Simulation of the Methodology

The hardware architecture of the storage management methodology was implemented in Quartus designer. Both low pass filters presented above (with $n_{MA} = 64$ and $n_{EWMA} = 32$) were implemented in the module and simulated separately with Modelsim software. The input data was created in Matlab and is shown in Figure 4.55. There are two fluorescence spike voltage that correspond to a larger and a smaller cancerous area. Figure 4.55 also shows the filtered results through a MA and EWMA filter. This data was digitised and introduced to the storage management module for simulation proposes.

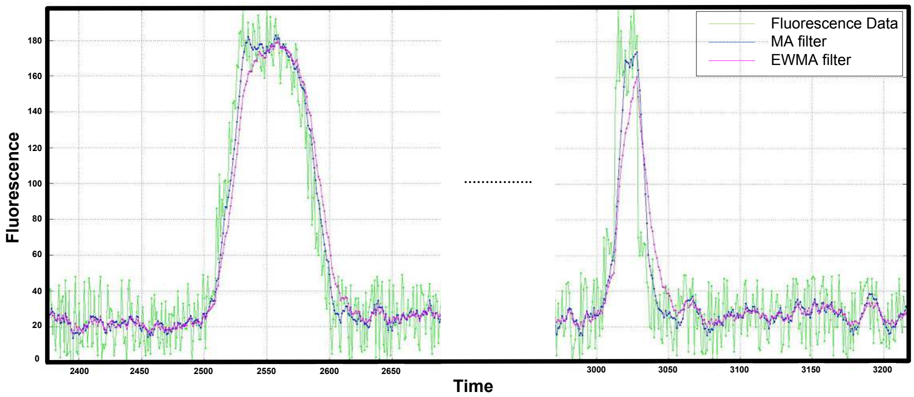

Figure 4.55: Fluorescence signals representing a larger and a smaller cancerous area.

Simulations of both topologies, shown in Figure 4.56, present the proper functionality of the storage management module with an effective detection of both ”cancerous” areas at expected time. Time-stamps in the topology with the EWMA filter indicate a timely faster spike detection, since this filter places more emphasis on the most recent sample.

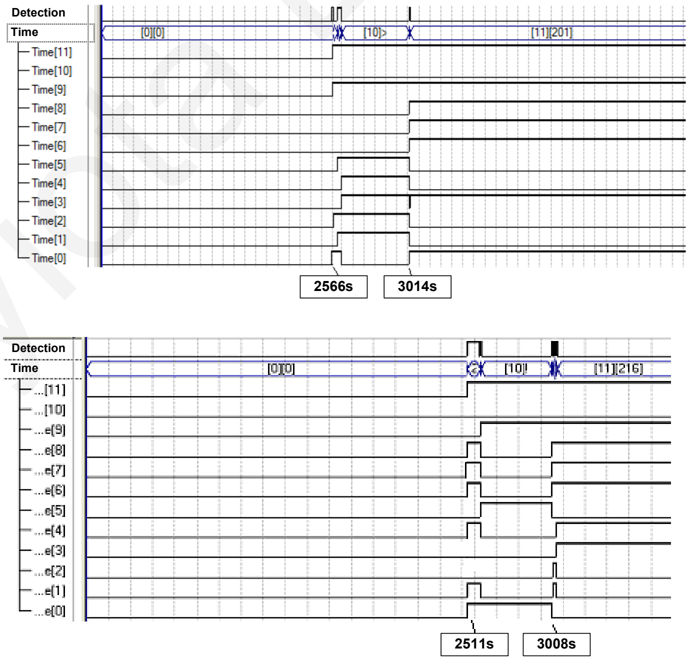

Figure 4.56: Simulation results of the Storage Management Module. MA filter (top) and EWMA filter implementation (bottom).

4.3.3 Optical Data Transmission

The extraction of fluorescence data from the capsules internal memory can be accomplished either through a 4-wire SPI interface (with an external FPGA playing the role of the SPI master to the SPI slave flash memory) for prototype debugging purposes, or through an infrared optical communication link. It is important to avoid the feedthroughs in the final version to keep the cost down and to minimise the chance of fluids leaking into the capsule. Figure 4.57 shows a picture of the prototype contactless data recovery system, which consists of: (a) a magnetic case that triggers capsule's hall sensor for data extraction, (b) a photodiode as the IR receiver, (c) an amplifier (OPA659) with high slew rate to track and reinforce the IR digital signals, (d) two charge pumps (MCP1252/3 and MAX1853) of $\pm 5V$ for power-supplying the amplifier and (e) an Opal Kelly FPGA board (XEM6010) for signal processing and USB interfacing of the data with a PC.

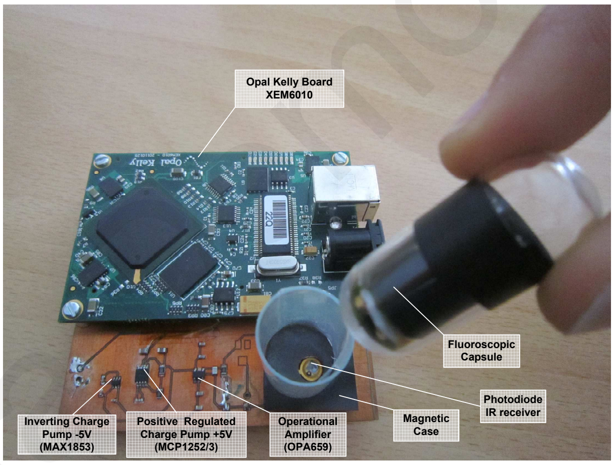

Figure 4.57: Contactless Data Recovery System

Once a capsule is placed in the magnetic case, the hall sensor outputs a digital signal that initiates the capsule readout mode. The CPLD reads the data from the flash memory via an SPI interface and then drives one of the IR excitation laser diodes in order to transmit the data to the data recovery system. In order to avoid using two LDs, i.e. one for the clock signal and one for the data signal, the transmitted output data was encoded within the capsule using a Manchester code, where the clock and data can be recovered from a single signal [28], thus halving the power to transmit the data. Manchester code represents binary values by a transition rather than a level ('0' or '1'). The transition occurs at mid-bit, with a low-to-high transition used to represent a logic '0', and a high-to-low to represent a logig '1' (Figure 4.58).

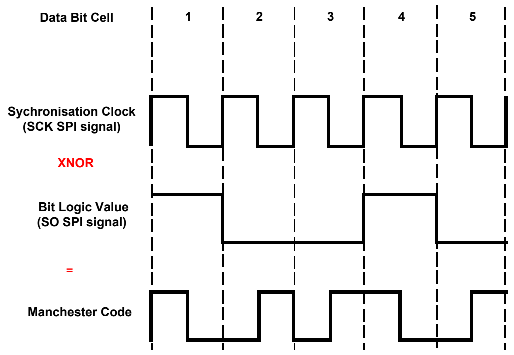

Figure 4.58: Conversion of SCK and SO SPI signals to a Manchester code.

To verify the correct transmission of the data via the IR scheme, the stored data was read out with two methods; firstly it was extracted by using a 4-wire SPI protocol and then the same data was extracted via the wireless-optical method described above. A small sample of the data extracted with the two methods is shown in Figure 4.59 where the data value can be seen to be the same. As the optical transmission is digitally encoded it is extremely robust. For recovering the IR data after the amplification, a modified Manchester Decoder from Xilinx (Application Note: XAPP339 - V1.3 October 1, 2002) was used in the data recovery system. The data was subsequently extracted to a .bin file through a USB Opal Kelly FPGA interface.

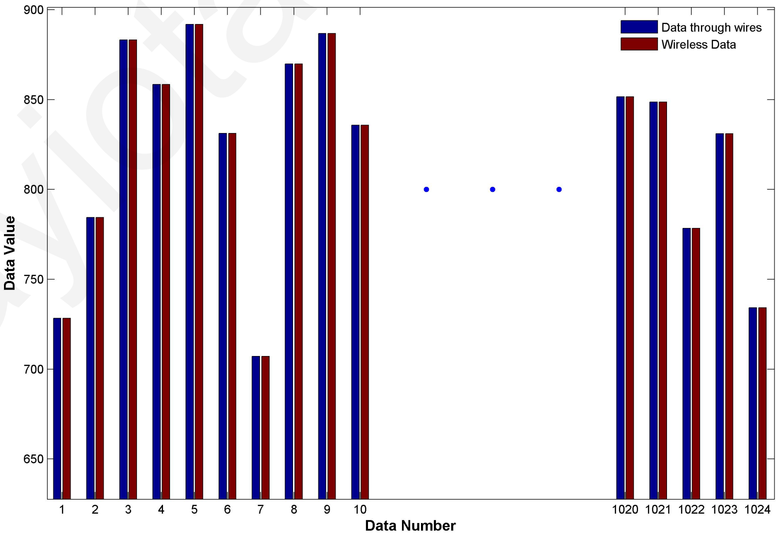

Figure 4.59: Capsule data extracted through a) 4-wire SPI interface and b) IR-optical transmission.

4.4 Summary

In this chapter an endoscopy cancer-screening capsule prototype was presented, which has demonstrated that it can detect Indocyanine Green-based cancer labelling agents, from the nanomolar to the micromolar range. The capsule has been tested in-vitro and ex-vivo, using ICG-impregnated swine intestine. The overall size of the capsule is suitable for ingestion by humans. It uses a variable sampling rate methodology, which reduces the amount of redundant data collected and enables the low current consumption of 6.3 mA. Furthermore, the magnetically-activated, wireless data readout technique does not require conductive feedthroughs or the hermetic seal of the capsule to be broken, in order to recover the data. Hence, the technical feasibility of a microcancer screening method for the small intestine, based on existing fluorescence biomarkers, has been proven.

Chapter 5

Conclusion

This thesis explores and develops a fluoroscopic screening capsule prototype for early-stage detection of cancerous cells in the small intestine, in order to provide more effective treatment to the patient. The development of such a device, which detects early-stage small intestine cancer via fluorescence emitted by ICG IR-biomarker, introduces, to the medical community, a novel, non-invasive cancer screening method for the small intestine. This project has successively delivered the first completely autonomous IR-fluorescence-based ingestible endoscopic cancer screening capsule that has no external wiring or receiver, that is relatively cheap, with low power requirements and that is able to detect and discriminate low concentrations of the IR-fluorophore indocynine green, which is related with the present of cancer in the small intestine.

5.1 Contributions

The key contribution of this thesis is the development of a unique IR-fluorescence-based endoscopic capsule, to implement a novel non-invasive cancer screening method for the small intestine. In implementing this capsule, a number of unique features were developed that can also be used in other applications. These are:

- The implementation of a sampling rate control algorithm that uses acceleration information in order to regulate the image/data acquisition sampling rate of a regular endoscopy capsule, thus reducing the power consumption of the system, avoiding unnecessary data collection, whilst providing a methodology for thoroughly scanning the G.I. tract.

- The usage of on-board memory, to eliminate the need for real time data transmission and to allow the patient to go about their normal activity, whilst undergoing screening. This avoids the use of an external data-receiver belt, which is used by the current endoscopic capsules.
- The implementation of a memory-efficient storage management algorithm, which uses a moving-average filtering technique in combination with threshold crossing methodology for the detection of fluorescence spikes, in a noisy background.
- The development of a contactless data recovery system, which is able to re-use the excitation laser diodes, to download the stored data, without breaching the hermetic seal. Once the capsule is attached to a read-out case, a magnetically-activated signal initiates the readout process.
- The use of air bubbles in epoxy to increase the divergence angle of the collimated laser diode beam.

5.2 Recommendations for Future Work

Future work on this topic would most be related to the commercial development of the capsule, since this work has proven the technological feasibility of the idea, and through a prototype, has led to a technology readiness level of the idea, that is suitable for the creation of a spin-off company.

Most definitely, the design and fabrication of a customised integrated circuit, which would include the majority of the discrete components used in this prototype, would further decrease the overall size and power of the system. This would free up more space for the optical parts of the system (optical filters, lenses, more detectors and excitation sources) and would increase battery life. Moreover, an integrated solution could increase the fluorescence detection sensitivity, by using charge-based amplifiers, thus enabling a decrease in the illumination power, which currently consumes about 95% of the power. Also if there is room for larger photodiodes, then once again it is possible to decrease the illumination power.

Finally, before being tested on humans, a series of in-vivo experiments in animal models are required. Such experiments will prove the ability of the capsule to detect early-stage cancers in living beings.

Appendix A

Altium Designer: Circuits Schematics and PCBs

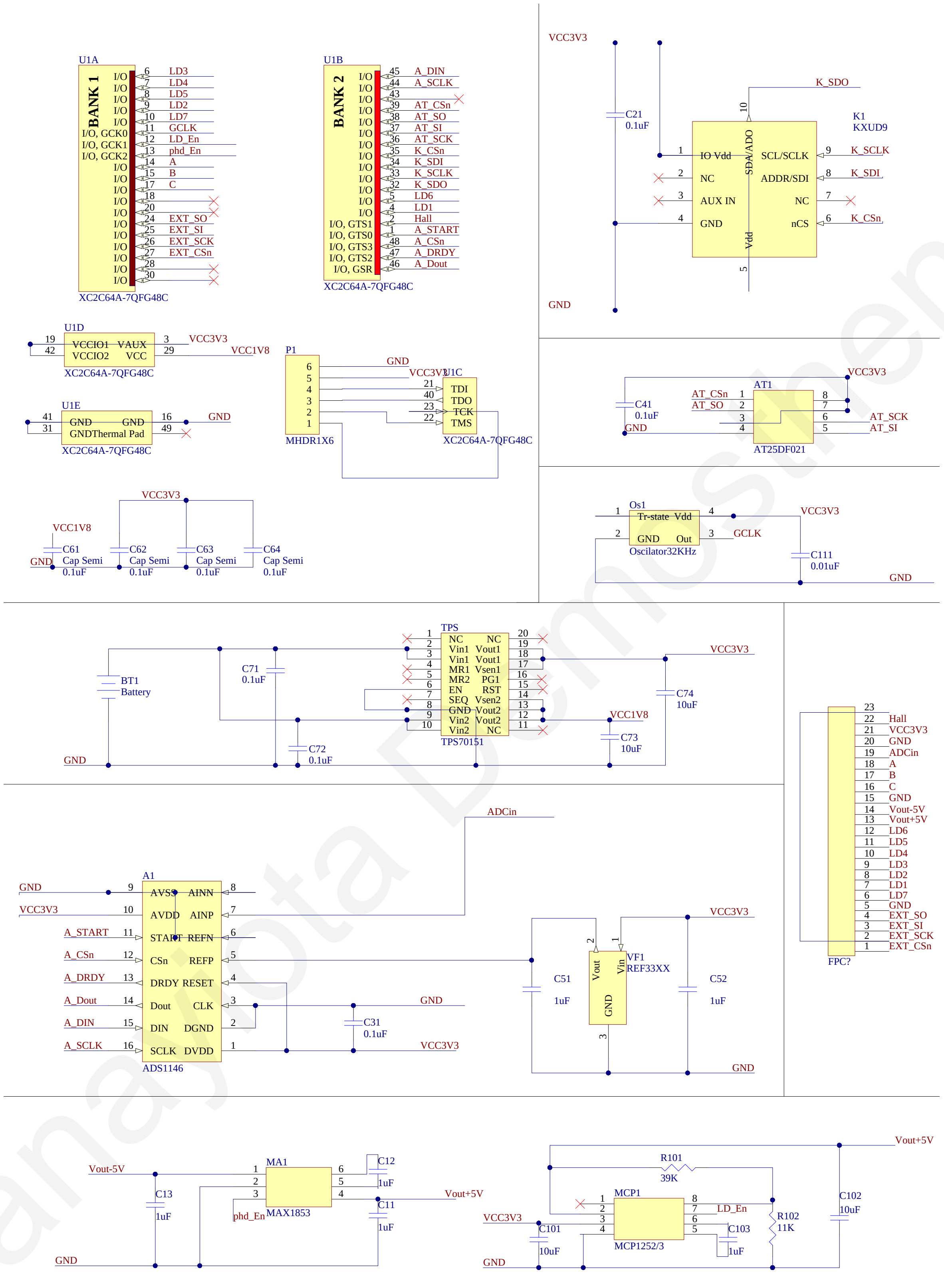

Figure A.1: Circuit Schematic of the first generation capsule Rigid PCB part.

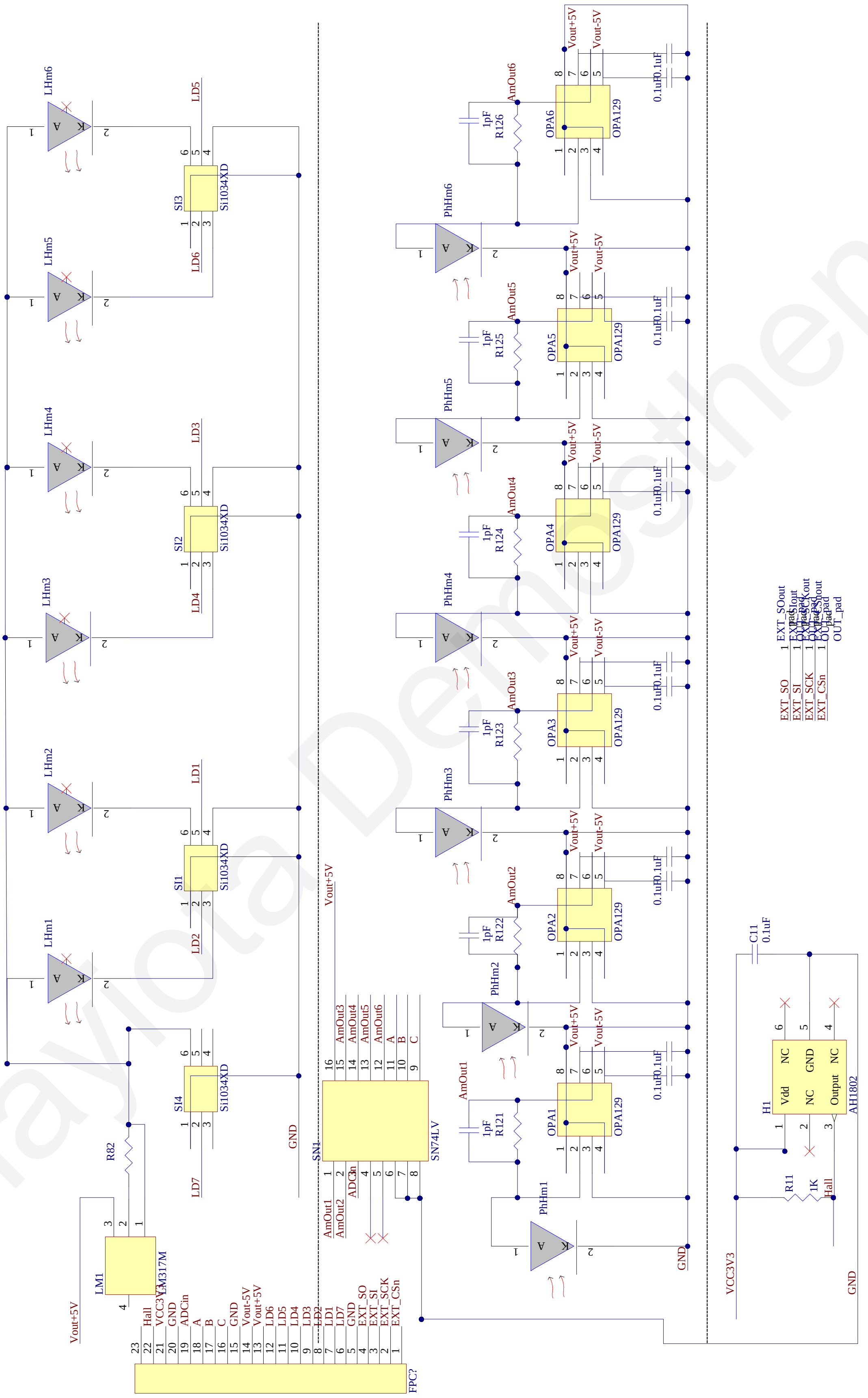

Figure A.2: Circuit Schematic of the first generation capsule flexible PCB part.

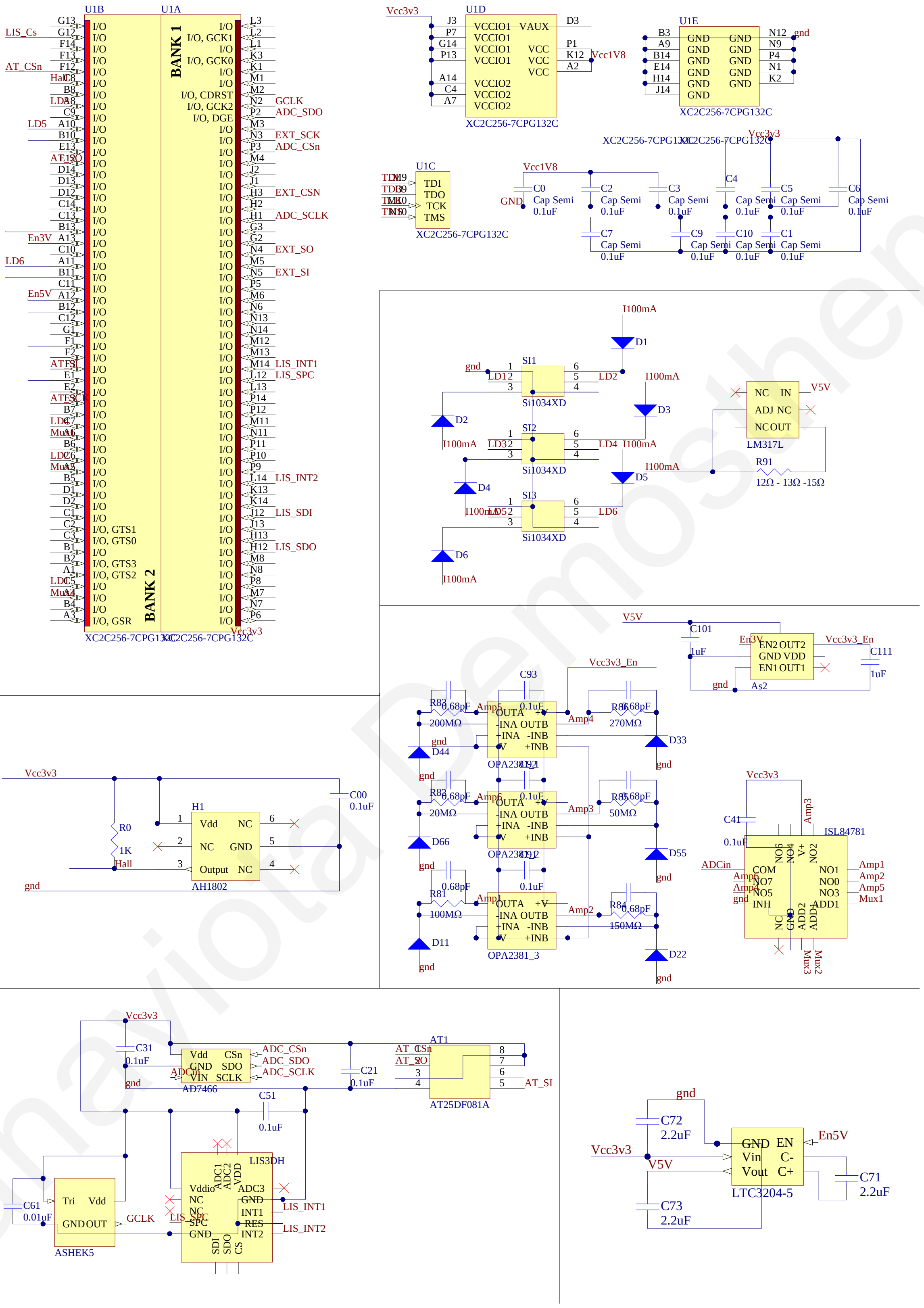

Figure A.3: Circuit Schematic of the second generation capsule.

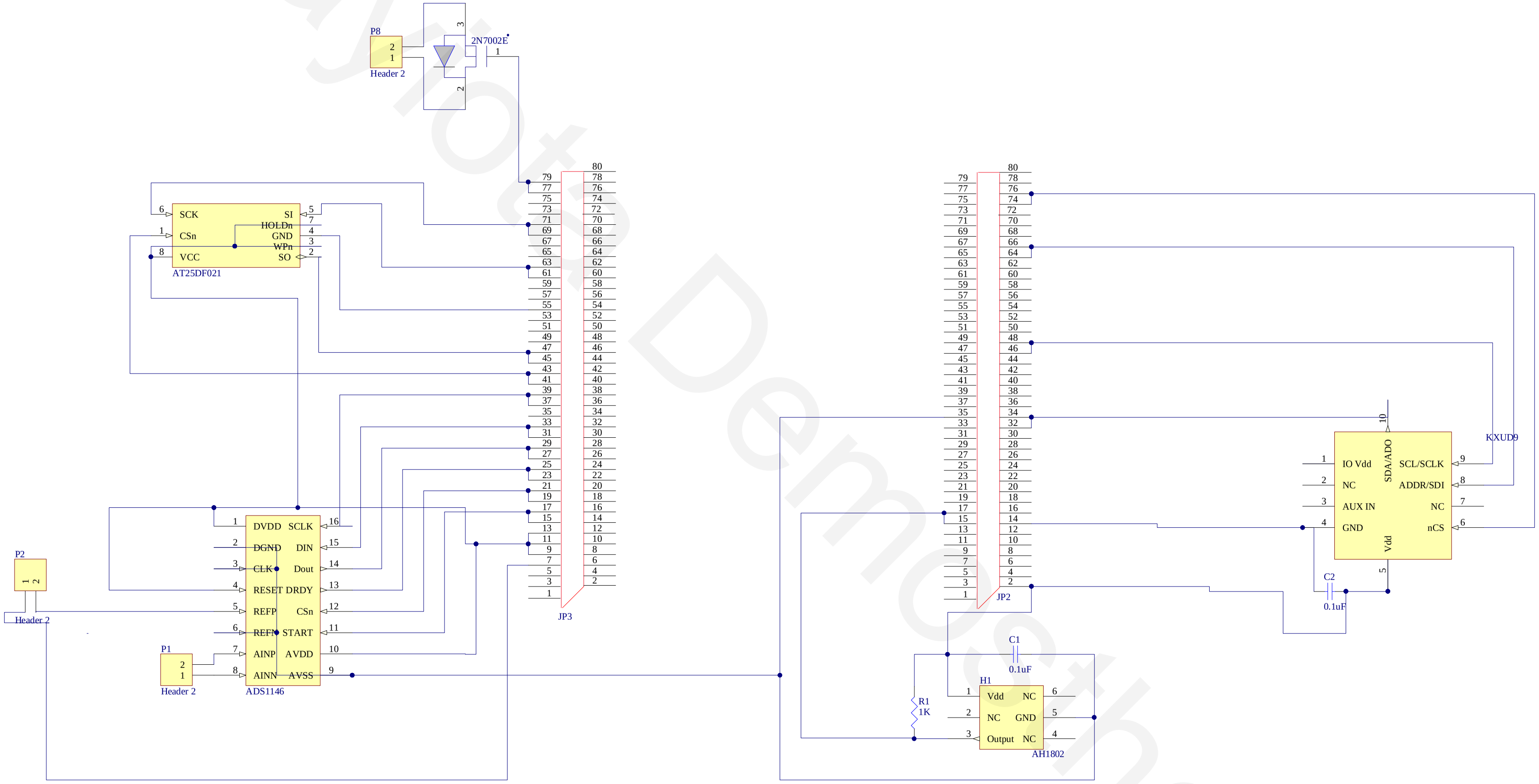

Figure A.4: Circuit Schematic of the hardware platform that tests the variable sampling rate methodology.

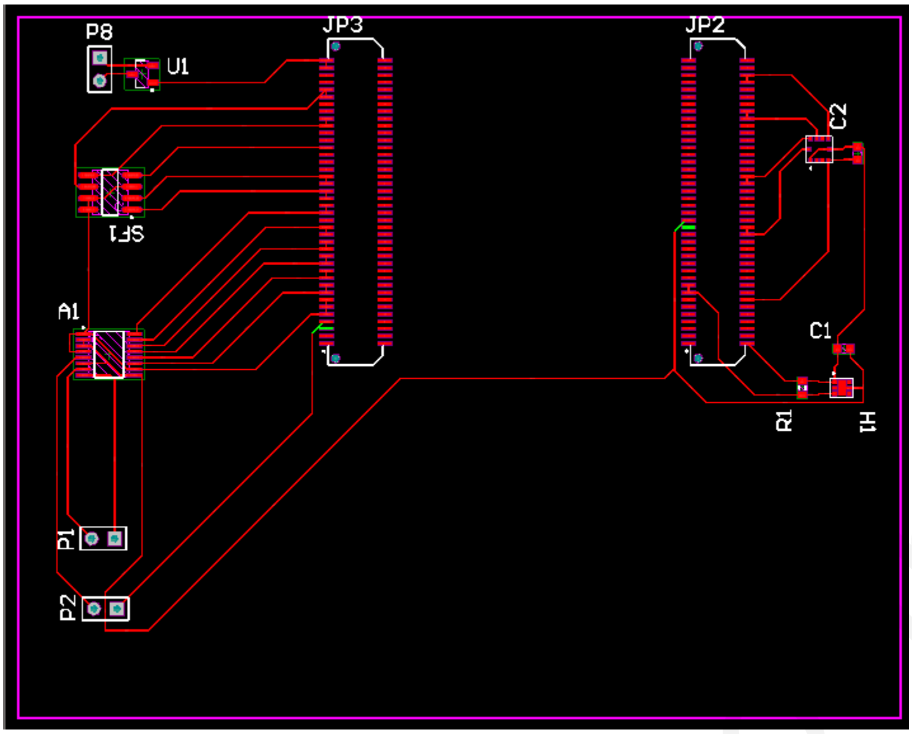

Figure A.5: PCB of the hardware platform that tests the variable sampling rate methodology.

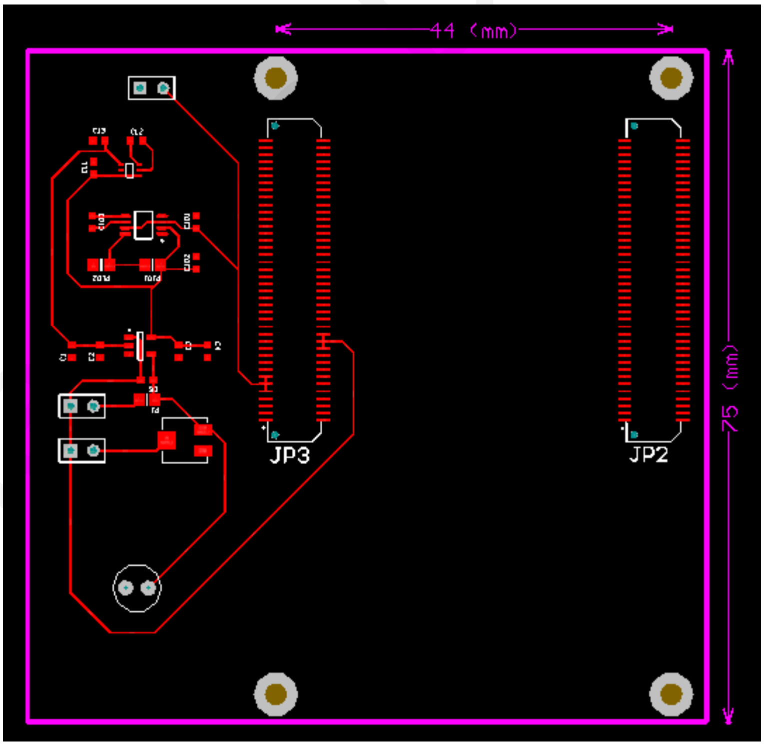

Figure A.6: PCB of the contactless data recovery system.

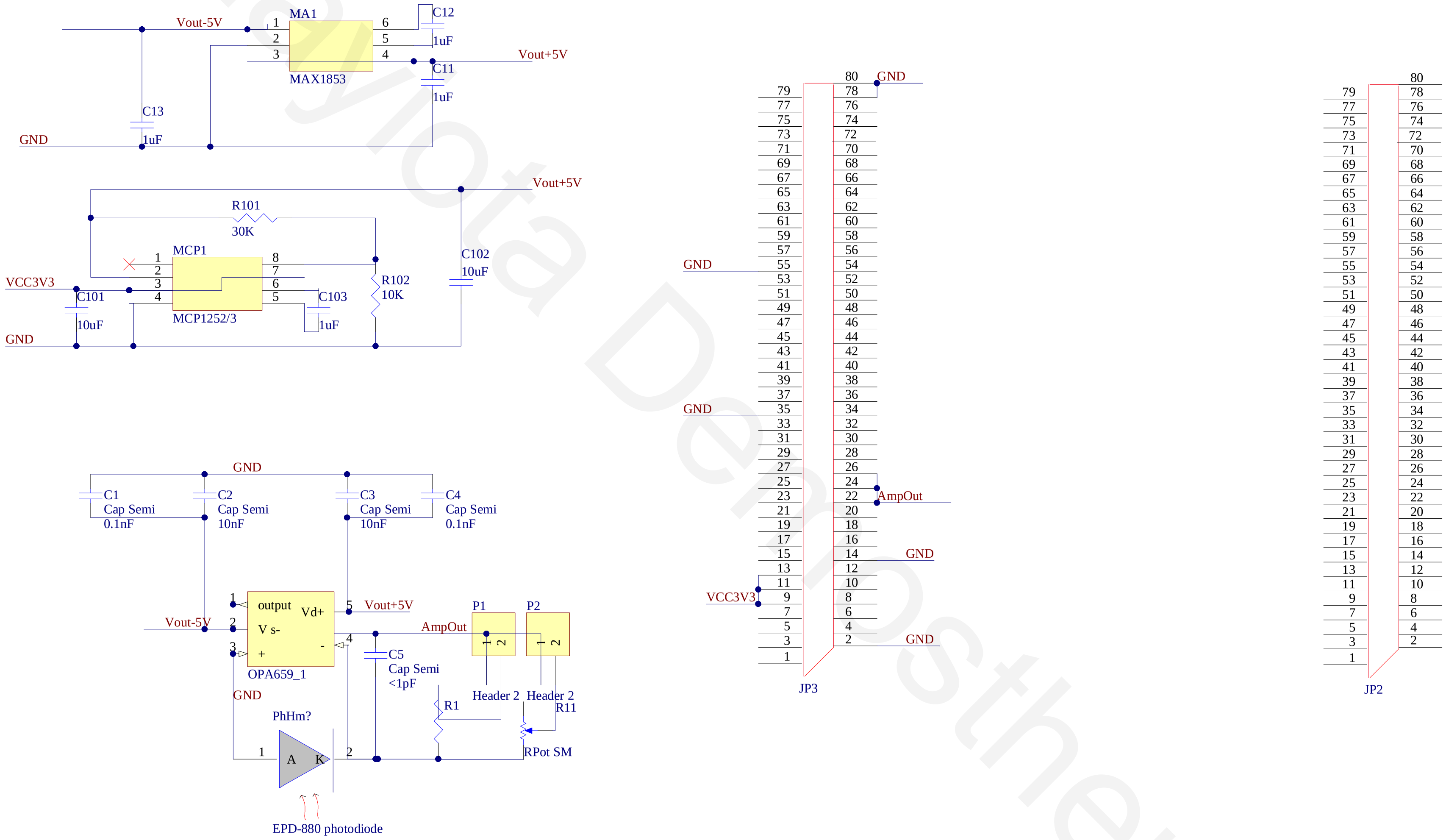

Figure A.7: Circuit Schematic of the contactless data recovery system.

Appendix B

Coding: VHDL, Matlab and Opal Kelly Front Panel Codes

B.1 SPI master VHDL code for external controlling of the capsule internal flash memory through 4-wire SPI signals

```
library IEEE;
use IEEE.STD_LOGIC_1164.ALL;
use IEEE.numeric_std.all;
use ieee.std_logic_arith.all ;
use IEEE.std_logic_unsigned.all;
use work.FRONTPANEL.all;

entity DataExtractor is
port (hi_in     : in    STD_LOGIC_VECTOR(7 downto 0);
        hi_out    : out   STD_LOGIC_VECTOR(1 downto 0);
        hi_inout  : inout STD_LOGIC_VECTOR(15 downto 0);
        hi_aa     : inout STD_LOGIC;
        hi_muxsel,i2c_sda,i2c_scl: out STD_LOGIC;
        CSN_EXT,SCK_EXT,SI_EXT:out STD_LOGIC;
      SO_EXT:in STD_LOGIC;
      clk1:in STD_LOGIC);
end DataExtractor;
```

```
architecture Behavioral of DataExtractor is

signal ti_clk    : STD_LOGIC;
signal ok1    : STD_LOGIC_VECTOR(30 downto 0);
signal ok2    : STD_LOGIC_VECTOR(16 downto 0);
signal ok2s   : STD_LOGIC_VECTOR(3*17-1 downto 0);

Component FMSystem_Entity is
port (clk1,ti_clk,MRST,Unprotect,Erase,sampleCLK,
 Readingin,SO,btpipeO_read0:in std_logic;
 LEDs:inout std_logic_vector (15 downto 0);
 ReadAddr: in std_logic_vector(23 downto 0);
 Data,Data2:in std_logic_vector (15 downto 0);
 btpipeO_data0:out std_logic_vector (15 downto 0);
 Mode:in std_logic_vector (1 downto 0);
 AddressOut:inout std_logic_vector(23 downto 0));
end Component;

signal RST,btpipeO_data0,btpipeO_data1,Unprotect,LEDs,Erase,Readingin,
       Writing,ModeFM,ReadAddr1,ReadAddr2,AddrOut1,Paralout,
       Paralout1:std_logic_vector(15 downto 0);

signal btpipeO_read0,btpipeO_read1,bs_out,SO,SO15,BSY1,
       full1,empty1:std_logic;

signal AddressOut1,ReadAddress:std_logic_vector(23 downto 0);

signal clk2,Div2,Div4,Div8,Div16,Div32,Div64,Div128,Div256,Div512,
       Div1024,Div2048:std_logic;

begin

i2c_sda    <= 'Z';
i2c_scl    <= 'Z';
hi_muxsel  <= '0';
```

```
-- Implement the logic
g1:FMSystem_Entity PORT MAP(clk1 => clk2,ti_clk => ti_clk,
   MRST => RST(0),Unprotect => Unprotect(0),Erase => Erase(0),
   sampleCLK =>Writing(0),Readingin => Readingin(0),
   SO => SO,btpipeO_read0 => btpipeO_read0,LEDs => LEDs,
   ReadAddr => ReadAddress,Data => x"44AA",Data2 => x"3377",
   btpipeO_data0 => btpipeO_data0,Mode => ModeFM(1 downto 0),
   AddressOut =>AddressOut1);
ReadAddress<=ReadAddr2(7 downto 0)& ReadAddr1;
AddrOut1<="0000"  & AddressOut1(11 downto 0);

SO<=SO_EXT;
CSN_EXT<=LEDs(5);
SCK_EXT<=LEDs(6);
SI_EXT<=LEDs(7);

---clocks dividers
process (clk1,RST(0),Div2,Div4,Div8,Div16,Div32,Div64,Div128,
         Div256,Div512,Div1024,Div2048)
begin

if (RST(0) = '1') then
Div2 <= '0';
elsif rising_edge(clk1) then--T=0.03ms
Div2 <= not Div2;--0.06ms
end if;

if (RST(0) = '1') then
Div4 <= '0';
elsif rising_edge (Div2) then
Div4 <= not Div4;--0.12ms
end if;

if (RST(0) = '1') then
Div8 <= '0';
elsif rising_edge (Div4) then
```

```
Div8 <= not Div8;--0.24ms
end if;

if (RST(0) = '1') then
Div16 <= '0';
elsif rising_edge (Div8) then
Div16 <= not Div16;--0.5ms
end if;

if (RST(0) = '1') then
Div32 <= '0';
elsif rising_edge (Div16) then
Div32 <= not Div32;--1ms
end if;

if (RST(0) = '1') then
Div64 <= '0';
elsif rising_edge (Div32) then
Div64 <= not Div64;--2ms
end if;

if (RST(0) = '1') then
Div128 <= '0';
elsif rising_edge (Div64) then
Div128 <= not Div128;--4ms
end if;

if (RST(0) = '1') then
Div256 <= '0';
elsif rising_edge (Div128) then
Div256 <= not Div256;--8ms
end if;

if (RST(0) = '1') then
Div512 <= '0';
elsif rising_edge (Div256) then
```

```
Div512 <= not Div512;--16ms
end if;

if (RST(0) = '1') then
Div1024 <= '0';
elsif rising_edge (Div512) then
Div1024 <= not Div1024;--32ms
end if;

if (RST(0) = '1') then
Div2048 <= '0';
elsif rising_edge (Div1024) then
Div2048 <= not Div2048;--64ms
end if;

-- resynchronize back to clock
if (RST(0) = '1') then
clk2 <= '0';
elsif rising_edge(clk1) then
clk2 <= Div2048;
end if;
end process;

--Instantiate the okHost and connect endpoints
okHI : okHost port map (hi_in=>hi_in, hi_out=>hi_out,
                        hi_inout=>hi_inout,hi_aa=>hi_aa,
                        ti_clk=>ti_clk,ok1=>ok1, ok2=>ok2);
okWO : okWireOR   generic map (N=>3) port map (ok2=>ok2, ok2s=>ok2s);

ep1: okWireIn port map (ok1=>ok1,ep_addr=>x"00", ep_dataout=>RST);
ep2: okWireIn port map (ok1=>ok1,ep_addr=>x"06", ep_dataout=>Writing);
ep3: okWireIn port map (ok1=>ok1,ep_addr=>x"07", ep_dataout=>Readingin);
ep4: okWireIn port map (ok1=>ok1,ep_addr=>x"08", ep_dataout=>Unprotect);
ep5: okWireIn port map (ok1=>ok1,ep_addr=>x"09", ep_dataout=>Erase);
ep6: okWireIn port map (ok1=>ok1,ep_addr=>x"0C", ep_dataout=>ModeFM);
ep7: okWireIn port map (ok1=>ok1,ep_addr=>x"0D", ep_dataout=>ReadAddr1);
```

```
ep8: okWireIn port map (ok1=>ok1,ep_addr=>x"0E", ep_dataout=>ReadAddr2);
ep9: okWireOut port map (ok1=>ok1, ok2=>ok2s( 1*17-1 downto 0*17 ),
                         ep_addr=>x"20", ep_datain=>LEDs);
ep10: okWireOut port map (ok1=>ok1, ok2=>ok2s( 2*17-1 downto 1*17 ),
                          ep_addr=>x"22", ep_datain=>AddrOut1);
ep11: okBTPipeOut port map (ok1=>ok1, ok2=>ok2s(3*17-1 downto 2*17 ),
       ep_addr=>x"A0", ep_read=>btpipeO_read0,ep_blockstrobe=>bs_out,
       ep_datain=>btpipeO_data0(15 downto 0), ep_ready=>'1');

end Behavioral;
```

```
library IEEE;
use IEEE.STD_LOGIC_1164.ALL;
use IEEE.NUMERIC_STD.ALL;

entity FMSystem_Entity is
port (clk1,ti_clk,MRST,Unprotect,Erase,sampleCLK,Readingin,SO,
      btpipeO_read0:in std_logic;
      LEDs:inout std_logic_vector (15 downto 0);
      ReadAddr: in std_logic_vector(23 downto 0);
      Data,Data2:in std_logic_vector (15 downto 0);
      btpipeO_data0:out std_logic_vector (15 downto 0);
      Mode:in std_logic_vector (1 downto 0);
      AddressOut:inout std_logic_vector(23 downto 0));
end FMSystem_Entity;

architecture Behavioral of FMSystem_Entity is

component Write_Entity
port (clk1,MRST,sampleCLK,SO:in std_logic;
      Data,Data2:in STD_LOGIC_VECTOR (15 downto 0);
      CSn_2,SCK_2,SI_2,WrEnd:out std_logic;
      AddressOut:inout std_logic_vector(23 downto 0));
end component;
```

```
component Unprotect_Entity
port (clk1,MRST,Unprotect,SO:in std_logic;
      CSn_0,SCK_0,SI_0:out std_logic;
      Unpr,SPRL:out std_logic);
end component;

component Erase_Entity
port (clk1,MRST,Erase,SO:in std_logic;
      CSn_1,SCK_1,SI_1:out std_logic;
      Move_1,EPE:out std_logic);
end component;

component Read_Entity
port (clk1,MRST,Readingin,SO:in std_logic;
      Addr: in std_logic_vector(23 downto 0);
      CSn_3,SCK_3,SI_3,BSY_3,Move_3:out std_logic;
      Paralout1:out std_logic_vector(15 downto 0));
end component;

component MUX_S
 Port (sel: in  STD_LOGIC_VECTOR (1 downto 0);
           input4,input3,input2,input1: in  STD_LOGIC;
       output : out STD_LOGIC);
end component;

component Decoder1
port (input:in std_logic_vector(2 downto 0);
      output:out std_logic_vector(7 downto 0));
end component;

component clkdivision2
port( clk, rst:in std_logic;
     clkout:inout std_logic_vector(2 downto 0));
end component;

component fifo2
```

```
        port (
        rst: in std_logic;
        wr_clk: in std_logic;
        rd_clk: in std_logic;
        din: in std_logic_vector(15 downto 0);
        wr_en: in std_logic;
        rd_en: in std_logic;
        dout: out std_logic_vector(15 downto 0);
        full: out std_logic;
        empty: out std_logic);
end component;

signal Paralout1:std_logic_vector(15 downto 0);
signal CSn_0,SCK_0,SI_0,CSn_1,SCK_1,SI_1,CSn_2,SCK_2,SI_2,
       BSY,CSn_3,SCK_3,SI_3,full1,empty1:std_logic;

begin

g1:Unprotect_Entity port map (clk1,notUnprotect,Unprotect,SO,
                              CSn_0,SCK_0,SI_0,LEDs(0),LEDs(1));
g2:Erase_Entity port map (clk1,not Erase,Erase,SO,CSn_1,
                          SCK_1,SI_1,LEDs(2),LEDs(3));
g3:Write_Entity port map (clk1,MRST,sampleCLK,SO,Data,Data2,
                          CSn_2,SCK_2,SI_2,LEDs(9),AddressOut);
g4:Read_Entity port map (clk1,MRST,Readingin,SO,ReadAddr,CSn_3,
                        SCK_3,SI_3,BSY,LEDs(4),Paralout1);
g5:MUX_S port map(Mode(1 downto 0),CSn_3,CSn_2,CSn_1,CSn_0,LEDs(5));
g6:MUX_S port map(Mode(1 downto 0),SCK_3,SCK_2,SCK_1,SCK_0,LEDs(6));
g7:MUX_S port map(Mode(1 downto 0),SI_3,SI_2,SI_1,SI_0,LEDs(7));
g8:fifo2 port map (rst =>MRST,wr_clk => BSY,rd_clk => ti_clk,
    din => Paralout1,wr_en => Readingin,rd_en => btpipeO_read0,
    dout => btpipeO_data0,full => full1,empty => empty1);

end Behavioral;
```

B.2 Front Panel interface code for external controlling of the capsule internal flash memory

```
<object class="okPanel" name="panel1">
        <title>First FrontPanel Example</title>
        <size>500,550</size>

       <object class="okStaticBox">
                <position>10,290</position>
                <size>100,20</size>
                <label>Flash Memory Control</label>
        </object>

        <object class="okToggleButton">
                <label>RST</label>
                <position>10,250</position>
                <size>70,25</size>
                <endpoint>0x00</endpoint>
                <bit>0</bit>
        </object>

       <object class="okDigitEntry">
                <position>10,320</position>
                <size>70,25</size>
                <tooltip>Mode</tooltip>
                <radix>16</radix>
                <minvalue>0</minvalue>
                <maxvalue>3</maxvalue>
                <endpoint>0x0C</endpoint>
                <bit>0</bit>
                <value>0003</value>
        </object>

        <object class="okStaticBox">
                <position>100,320</position>
```

```
         <size>300,25</size>
         <label>00:Unprotect,01:Erase,10:Write,11:Read</label>
 </object>

<object class="okToggleButton">
         <label>Writing</label>
         <position>300,350</position>
         <size>70,25</size>
         <endpoint>0x06</endpoint>
         <bit>0</bit>
 </object>

<object class="okToggleButton">
         <label>Unprotect</label>
         <position>10,350</position>
         <size>70,25</size>
         <endpoint>0x08</endpoint>
         <bit>0</bit>
 </object>

 <object class="okToggleButton">
         <label>Erase</label>
         <position>10,380</position>
         <size>70,25</size>
         <endpoint>0x09</endpoint>
         <bit>0</bit>
 </object>

 <object class="okToggleButton">
         <label>Read Data</label>
         <position>10,410</position>
         <size>70,25</size>
         <endpoint>0x07</endpoint>
         <bit>0</bit>
 </object>
```

```
       <object class="okStaticBox">
                <position>90,400</position>
                <size>71,45</size>
                <label>Read Address</label>
        </object>

        <object class="okDigitEntry">
                <position>90,410</position>
                <size>70,25</size>
                <tooltip>Read Address2</tooltip>
                <radix>16</radix>
                <minvalue>0</minvalue>
                <maxvalue>255</maxvalue>
                <endpoint>0x0E</endpoint>
                <bit>0</bit>
                <value>0000</value>
        </object>

        <object class="okDigitEntry">
                <position>200,410</position>
                <size>70,25</size>
                <tooltip>Read Address1</tooltip>
                <radix>16</radix>
                <minvalue>0</minvalue>
                <maxvalue>65535</maxvalue>
                <endpoint>0x0D</endpoint>
                <bit>0</bit>
                <value>0000</value>
        </object>

<-- LEDs -->
        <object class="okLED">
                <position>100,350</position>
                <size>25,25</size>
                <label align="bottom">Yes</label>
                <style>SQUARE</style>
```

```
                <color>#00ff00</color>
                <endpoint>0x20</endpoint>
                <bit>0</bit>
        </object>
        <object class="okLED">
                <position>120,350</position>
                <size>25,25</size>
                <label align="bottom">Yes</label>
                <style>SQUARE</style>
                <color>#00ff00</color>
                <endpoint>0x20</endpoint>
                <bit>1</bit>
        </object>
        <object class="okLED">
                <position>100,380</position>
                <size>25,25</size>
                <label align="bottom">Yes</label>
                <style>SQUARE</style>
                <color>#00ff00</color>
                <endpoint>0x20</endpoint>
                <bit>2</bit>
        </object>
        <object class="okLED">
                <position>120,380</position>
                <size>25,25</size>
                <label align="bottom">No</label>
                <style>SQUARE</style>
                <color>#00ff00</color>
                <endpoint>0x20</endpoint>
                <bit>3</bit>
        </object>
        <object class="okLED">
                <position>10,440</position>
                <size>25,25</size>
                <label align="bottom">CSn</label>
                <style>SQUARE</style>
```

```
        <color>#00ff00</color>
        <endpoint>0x20</endpoint>
        <bit>5</bit>
</object>
<object class="okLED">
        <position>30,440</position>
        <size>25,25</size>
        <label align="bottom">SCK</label>
        <style>SQUARE</style>
        <color>#00ff00</color>
        <endpoint>0x20</endpoint>
        <bit>6</bit>
</object>
<object class="okLED">
        <position>50,440</position>
        <size>25,25</size>
        <label align="bottom">SI</label>
        <style>SQUARE</style>
        <color>#00ff00</color>
        <endpoint>0x20</endpoint>
        <bit>7</bit>
</object>
<object class="okLED">
        <position>400,350</position>
        <size>25,25</size>
        <label align="bottom">WrEnd</label>
        <style>SQUARE</style>
        <color>#00ff00</color>
        <endpoint>0x20</endpoint>
        <bit>9</bit>
</object>

<object class="okDigitDisplay">
        <position>10,490</position>
        <size>70,25</size>
        <tooltip>AddressOut</tooltip>
```

```
                <radix>16</radix>
                <minvalue>0</minvalue>
                <maxvalue>65535</maxvalue>
                <endpoint>0x22</endpoint>
                <bit>0</bit>
        </object>

       <object class="okFilePipe">
                <position>90,490</position>
                <size>70,25</size>
                <label>BTpipe out0</label>
                <endpoint>0xA0</endpoint>
                <tooltip>read a file from pipe </tooltip>
                <length>131072</length>
                <append/>
        </object>

</object>
</resource>
```

B.3 Import of a .bin file in Matlab and further processing of the data for the calculation of the fluorescence signals values

```
fid=fopen('x5.bin','r');
data=fread(fid);
LSBindex=5:2:length(data);
MSBindex=6:2:length(data);
LSB=data(LSBindex);
MSB=data(MSBindex);
DataBin=MSB*256+LSB;
plot(data,'rx-');
```

Bibliography

[1] *http://omlc.org/spectra/icg/.*

[2] "Cancer prevention & early detection facts & figures 2013," *Atlanta, GA: American Cancer Society*, 2013.

[3] *http://en.wikipedia.org/wiki/Small-intestine*, 2013.

[4] *http://www.light-catcher.com.cn/ProductFiles/ADL-78901SX.pdf*, 2013.

[5] *http://en.wikipedia.org/wiki/Human-body-temperature*, 2014.

[6] M. A. Al-Rawhani, D. Chitnis, J. Beeley, S. Collins, and D. R. Cumming, "Design and implementation of a wireless capsule suitable for autofluorescence intensity detection in biological tissues," *Biomedical Engineering, IEEE Transactions on*, vol. 60, no. 1, pp. 55–62, 2013.

[7] J. T. Alander, I. Kaartinen, A. Laakso, T. Pätilä, T. Spillmann, V. V. Tuchin, M. Venermo, and P. Välisuo, "A review of indocyanine green fluorescent imaging in surgery," *Journal of Biomedical Imaging*, vol. 2012, p. 7, 2012.

[8] M. Appleyard, A. Glukhovsky, and P. Swain, "Wireless-capsule diagnostic endoscopy for recurrent small-bowel bleeding," *New England Journal of Medicine*, vol. 344, no. 3, pp. 232–233, 2001.

[9] T. Bando, N. Muguruma, S. Ito, Y. Musashi, K. Inayama, Y. Kusaka, M. Tadatsu, K. Ii, T. Irimura, S. Shibamura, and K. Takesako, "Basic studies on a labeled anti-mucin antibody detectable by infrared-fluorescence endoscopy," *J. Gastroenterol*, vol. 37, no. 4, pp. 260–9, 2002.

[10] F. Barbier and G. De Weerdt, "Chromatography and IR spectrography of indocyanine green," *Clinica Chimica Acta*, vol. 10, no. 6, pp. 549–554, 1964.

[11] R. Benson and H. Kues, "Fluorescence properties of indocyanine green as related to angiography," *Physics in medicine and biology*, vol. 23, no. 1, p. 159, 1978.

[12] T. Bhuket, M. Takami, and L. Fisher, "The use of wireless capsule endoscopy in clinical diagnostic gastroenterology," 2005.

[13] S. Brown and J. Rose, "Architecture of FPGAs and CPLDs: A tutorial," *IEEE Design and Test of Computers*, vol. 13, no. 2, pp. 42–57, 1996.

[14] K. Chaiyasate, A. Jain, L. Cheung, M. Jacobs, and V. Mittal, "Prognostic factors in primary adenocarcinoma of the small intestine: 13-year single institution experience," *World Journal of Surgical Oncology*, vol. 6, no. 1, p. 12, 2008. [Online]. Available: http://www.wjso.com/content/6/1/12

[15] G. M. Cobrin, R. H. Pittman, and B. S. Lewis, “Increased diagnostic yield of small bowel tumors with capsule endoscopy,” *Cancer*, vol. 107, no. 1, pp. 22–27, 2006.

[16] J. Collins, “Change in the infra-red absorption spectrum of water with temperature,” *Physical Review*, vol. 26, no. 6, p. 771, 1925.

[17] J. A. Curcio and C. C. Petty, “The near infrared absorption spectrum of liquid water,” *JOSA*, vol. 41, no. 5, pp. 302–302, 1951.

[18] G. E. Davis, “Scattering of light by an air bubble in water,” *JOSA*, vol. 45, no. 7, pp. 572–572, 1955.

[19] R. De Levie, *Advanced Excel for Scientific Data Analysis*. Oxford: Oxford University Press, 2004.

[20] M. de Mascarenhas-Saraiva and L. da Silva Araujo, “Small-bowel tumors diagnosed by wireless capsule endoscopy: report of five cases,” *Endoscopy*, vol. 35, no. 10, pp. 865–868, 2003.

[21] P. Demosthenous and J. Georgiou, “Acceleration-dependent sampling for ingestible endoscopic imaging capsule,” in *Biomedical Circuits and Systems Conference (BioCAS), 2012 IEEE*, Nov 2012, pp. 1–4.

[22] P. Demosthenous, N. Nicolaou, and J. Georgiou, “A hardware-efficient low-pass filter design for biomedical applications,” in *Biomedical Circuits and Systems Conference (BioCAS), 2010 IEEE*, Nov 2010, pp. 130–133.

[23] T. Desmettre, J. Devoisselle, and S. Mordon, “Fluorescence properties and metabolic features of indocyanine green (ICG) as related to angiography,” *Survey of ophthalmology*, vol. 45, no. 1, pp. 15–27, 2000.

[24] R. Dias, J. Correia, and G. Minas, “On-chip integrated optical sensors for fluorescence detection of cancer tissue: Application to capsule endoscopy,” in *Electronics, Circuits and Systems, 2007. ICECS 2007. 14th IEEE International Conference on*. IEEE, 2007, pp. 423–426.

[25] S. Donati, *Photodetectors: devices, circuits, and applications*. Prentice Hall PTR, 1999.

[26] L.-R. Dung and Y.-Y. Wu, “A wireless narrowband imaging chip for capsule endoscope,” *Biomedical Circuits and Systems, IEEE Transactions on*, vol. 4, no. 6, pp. 462–468, 2010.

[27] J. O. Escobedo, O. Rusin, S. Lim, and R. M. Strongin, “NIR dyes for bioimaging applications,” *Current opinion in chemical biology*, vol. 14, no. 1, pp. 64–70, 2010.

[28] R. Forster, “Manchester encoding: opposing definitions resolved,” *Engineering Science & Education Journal*, vol. 9, no. 6, pp. 278–280, 2000.

[29] J. Gathje, R. R. Steuer, and K. Nicholes, “Stability studies on indocyanine green dye,” *J. appl. Physiol*, vol. 29, no. 2, pp. 181–185, 1970.

[30] A. Gerega, D. Milej, M. Kacprzak, P. Sawosz, N. Zolek, W. Weigl, E. Mayzner-Zawadzka, R. Maniewski, and A. Liebert, “Multi-wavelength time-resolved detection of fluorescence of indocyanine green circulating in the human head,” in *Biomedical Optics and 3-D Imaging*. Optical Society of America, 2010, p. JMA56.

[31] K. Gono, “Novel multifunctional endoscopic imaging system for support of early cancer diagnosis,” in *Lasers and Electro-Optics Society, 2007. LEOS 2007. The 20th Annual Meeting of the IEEE*. IEEE, 2007, pp. 69–70.

[32] M. Hambek, C. Solbach, H.-G. Schnuerch, M. Roller, M. Stegmueller, A. Sterner-Kock, J. Kiefer, and R. Knecht, “Tumor necrosis factor α sensitizes low epidermal growth factor receptor (EGFR)-expressing carcinomas for anti-EGFR therapy,” *Cancer research*, vol. 61, no. 3, pp. 1045–1049, 2001.

[33] J. H. Han and S. W. Park, “Effect of temperature and injection current on characteristics of TO-CAN packaged fabry–perot laser diode,” *Current Applied Physics*, vol. 7, no. 1, pp. 6–9, 2007.

[34] J. Haringsma, G. N. Tytgat, H. Yano, H. Iishi, M. Tatsuta, T. Ogihara, H. Watanabe, N. Sato, N. Marcon, B. C. Wilson *et al.*, “Autofluorescence endoscopy: feasibility of detection of GI neoplasms unapparent to white light endoscopy with an evolving technology,” *Gastrointestinal endoscopy*, vol. 53, no. 6, pp. 642–650, 2001.

[35] C. Haritoglou, W. Freyer, S. G. Priglinger, and A. Kampik, “Light absorbing properties of indocyanine green (ICG) in solution and after adsorption to the retinal surface—an ex-vivo approach,” *Graefe's Archive for Clinical and Experimental Ophthalmology*, vol. 244, no. 9, pp. 1196–1202, 2006.

[36] C. Haritoglou, A. Gandorfer, M. Schaumberger, R. Tadayoni, A. Gandorfer, and A. Kampik, “Light-absorbing properties and osmolarity of indocyanine-green depending on concentration and solvent medium,” *Investigative ophthalmology & visual science*, vol. 44, no. 6, pp. 2722–2729, 2003.

[37] M. Harvey J. Dworken, “Human digestive system.” *Encyclopedia Britannica Online http://www.britannica.com*, 2009.

[38] A. Hayim, M. Knieser, M. Rizkalla *et al.*, “DSPs/FPGAs comparative study for power consumption, noise cancellation, and real time high speed applications,” *Journal of Software Engineering and Applications*, vol. 3, no. 04, p. 391, 2010.

[39] T. Hirata, H. Kogiso, K. Morimoto, S. Miyamoto, H. Taue, S. Sano, N. Muguruma, S. Ito, and Y. Nagao, “Synthesis and reactivities of 3-indocyanine-green-acyl-1, 3-thiazolidine-2-thione (ICG-ATT) as a new near-infrared fluorescent-labeling reagent,” *Bioorganic & medicinal chemistry*, vol. 6, no. 11, pp. 2179–2184, 1998.

[40] W. Holzer, M. Mauerer, A. Penzkofer, R.-M. Szeimies, C. Abels, M. Landthaler, and W. Bäumler, “Photostability and thermal stability of indocyanine green,” *Journal of Photochemistry and Photobiology B: Biology*, vol. 47, no. 2, pp. 155–164, 1998.

[41] B. L. Horecker, “The absorption spectra of hemoglobin and its derivatives in the visible and near infra-red regions,” *Journal of biological chemistry*, vol. 148, no. 1, pp. 173–183, 1943.

[42] G. Iddan, G. Meron, A. Glukhovsky, and P. Swain, “Wireless capsule endoscopy,” *Nature*, vol. 405, p. 417, 2000.

[43] K. Inayama, S. Ito, N. Muguruma, Y. Kusaka, T. Bando, Y. Tadatsu, M. Tadatsu, K. Ii, S. Shibamura, and K. Takesako, “Basic study of an agent for reinforcement of near-infrared fluorescence on tumor tissue,” *Digestive and liver disease*, vol. 35, no. 2, pp. 88–93, 2003.

[44] Y. Inoue, K. Izawa, S. Kiryu, A. Tojo, and K. Ohtomo, “Diet and abdominal autofluorescence detected by in vivo fluorescence imaging of living mice,” *Molecular imaging*, vol. 7, no. 1, pp. 21–27, 2008.

[45] S. Ito, N. Muguruma, Y. Kusaka, M. Tadatsu, K. Inayama, Y. Musashi, M. Yano, T. Bando, H. Honda, I. Shimizu *et al.*, “Detection of human gastric cancer in resected specimens using a novel infrared fluorescent anti-human carcinoembryonic antigen antibody with an infrared fluorescence endoscope in vitro,” *Endoscopy*, vol. 33, no. 10, pp. 849–853, 2001.

[46] S. Ito, N. Muguruma, S. Hayashi, S. Taoka, T. Bando, K. Inayama, M. Sogabe, T. Okahisa, S. Okamura, H. Shibata *et al.*, “Development of agents for reinforcement of fluorescence on near-infrared ray excitation for immunohistological staining,” *Bioorganic & medicinal chemistry*, vol. 6, no. 5, pp. 613–618, 1998.

[47] S. Ito, N. Muguruma, T. Kimura, H. Yano, Y. Imoto, K. Okamoto, M. Kaji, S. Sano, and Y. Nagao, “Principle and clinical usefulness of the infrared fluorescence endoscopy,” *J Med Invest*, vol. 53, no. 1-2, pp. 1–8, 2006.

[48] M. Kfouri, O. Marinov, P. Quevedo, N. Faramarzpour, S. Shirani, L.-C. Liu, Q. Fang, and M. J. Deen, “Toward a miniaturized wireless fluorescence-based diagnostic imaging system,” *Selected Topics in Quantum Electronics, IEEE Journal of*, vol. 14, no. 1, pp. 226–234, 2008.

[49] T. M. Kimura, N. Ito, S. Yano, H. Imoto, Y. Okamoto, K. Kaji, and S. M Okamura, “A novel diagnostic endoscopy for gastrointestinal lesions using infrared fluorescence and indocyanine-green.” Biophotonics, 2004. APBP 2004. The Second Asian and Pacific Rim Symposium on, 2004.

[50] T. Kimura, N. Muguruma, S. Ito, S. Okamura, Y. Imoto, H. Miyamoto, M. Kaji, and E. Kudo, “Infrared fluorescence endoscopy for the diagnosis of superficial gastric tumors,” *Gastrointestinal endoscopy*, vol. 66, no. 1, pp. 37–43, 2007.

[51] S. K. Knapp, “Using programmable logic to accelerate DSP functions,” *Xilinx, Inc*, pp. 1–8, 1995.

[52] M. Koleva, *CAE DS – Injection Moulding Materials: Poly(methyl methacrylate) (PMMA)*. Technical University of Gabrovo.

[53] K. S. Kumar, “Spectroscopy of indocyanine green photodegradation,” Ph.D. dissertation, Wichita State University, 1996.

[54] Y. Kusaka, S. Ito, N. Muguruma, M. Tadatsu, T. Bando, K. Ii, T. Irimura, and S. Shibamura, “Vital immunostaining of human gastric and colorectal cancers grafted into nude mice: a preclinical assessment of a potential adjunct to videoendoscopy,” *Journal of gastroenterology*, vol. 35, no. 10, pp. 748–752, 2000.

[55] M. Landsman, G. Kwant, G. Mook, and W. Zijlstra, “Light-absorbing properties, stability, and spectral stabilization of indocyanine green,” *J. Appl. Physiol*, vol. 40, no. 4, pp. 575–583, 1976.

[56] Y. Laperche, M.-C. Oudea, and D. Lostanlen, “Toxic effects of indocyanine green on rat liver mitochondria,” *Toxicology and applied pharmacology*, vol. 41, no. 2, pp. 377–387, 1977.

[57] S. Luo, E. Zhang, Y. Su, T. Cheng, and C. Shi, “A review of NIR dyes in cancer targeting and imaging,” *Biomaterials*, vol. 32, no. 29, pp. 7127–7138, 2011.

[58] K. Malzahn, T. Dreyer, H. Glanz, and C. Arens, “Autofluorescence endoscopy in the diagnosis of early laryngeal cancer and its precursor lesions,” *The Laryngoscope*, vol. 112, no. 3, pp. 488–493, 2002.

[59] M. V. Marshall, J. C. Rasmussen, I.-C. Tan, M. B. Aldrich, K. E. Adams, X. Wang, C. E. Fife, E. A. Maus, L. A. Smith, and E. M. Sevick-Muraca, “Near-infrared fluorescence imaging in humans with indocyanine green: a review and update,” *Open surgical oncology journal (Online)*, vol. 2, no. 2, p. 12, 2010.

[60] S. Matcher, M. Cope, and D. Delpy, “Use of the water absorption spectrum to quantify tissue chromophore concentration changes in near-infrared spectroscopy,” *Physics in medicine and biology*, vol. 39, no. 1, p. 177, 1994.

[61] B. Mayinger, P. Horner, M. Jordan, C. Gerlach, T. Horbach, W. Hohenberger, and E. G. Hahn, “Light-induced autofluorescence spectroscopy for the endoscopic detection of esophageal cancer,” *Gastrointestinal endoscopy*, vol. 54, no. 2, pp. 195–201, 2001.

[62] B. Mayinger, M. Jordan, P. Horner, C. Gerlach, S. Muehldorfer, B. R. Bittorf, K. E. Matzel, W. Hohenberger, E. G. Hahn, and K. Guenther, “Endoscopic light-induced autofluorescence spectroscopy for the diagnosis of colorectal cancer and adenoma,” *Journal of Photochemistry and Photobiology B: Biology*, vol. 70, no. 1, pp. 13–20, 2003.

[63] A. Moglia, A. Menciassi, and P. Dario, “Recent patents on wireless capsule endoscopy,” *Recent Patents on Biomedical Engineering*, vol. 1, no. 1, pp. 24–33, 2008.

[64] A. Moglia, A. Menciassi, M. O. Schurr, and P. Dario, “Wireless capsule endoscopy: from diagnostic devices to multipurpose robotic systems,” *Biomedical Microdevices*, vol. 9, no. 2, pp. 235–243, 2007.

[65] M. Monici, “Cell and tissue autofluorescence research and diagnostic applications,” *Biotechnology annual review*, vol. 11, pp. 227–256, 2005.

[66] F. Moradi, D. Wisland, T.-V. Cao, A. Peiravi, and H. Mahmoodi, “1-bit sub threshold full adders in 65nm CMOS technology,” in *Microelectronics, 2008. ICM 2008. International Conference on*, Dec 2008, pp. 268–271.

[67] N. Muguruma and S. Ito, “Labeled anti-mucin antibody detectable by infrared-fluorescence endoscopy,” *Cancer Biomarkers*, vol. 4, no. 6, pp. 321–328, 2008.

[68] N. Muguruma, S. Ito, T. Bando, S. Taoka, Y. Kusaka, S. Hayashi, S. Ichikawa, Y. Matsunaga, Y. Tada, S. Okamura *et al.*, “Labeled carcinoembryonic antigen antibodies excitable by infrared rays: A novel diagnostic method for micro cancers in the digestive tract,” *Internal medicine*, vol. 38, no. 7, pp. 537–542, 1999.

[69] R. Nicholson, J. Gee, and M. . Harper, “EGFR and cancer prognosis,” *European Journal of Cancer*, vol. 37, pp. 9–15, 2001.

[70] N. Normanno, A. De Luca, C. Bianco, L. Strizzi, M. Mancino, M. R. Maiello, A. Carotenuto, G. De Feo, F. Caponigro, and D. S. Salomon, “Epidermal growth factor receptor (EGFR) signaling in cancer,” *Gene*, vol. 366, no. 1, pp. 2–16, 2006.

[71] *Laser Safety Handbook*, Northwestern University - Office for Research Safety, 2011.

[72] K. Odonnell and X. Chen, “Temperature dependence of semiconductor band gaps,” *Applied physics letters*, vol. 58, no. 25, pp. 2924–2926, 1991.

[73] M. Ogawa, N. Kosaka, P. L. Choyke, and H. Kobayashi, “In vivo molecular imaging of cancer with a quenching near-infrared fluorescent probe using conjugates of monoclonal antibodies and indocyanine green,” *The Journal of Cancer Research*, vol. 69, no. 4, pp. 1268–72, 2009.

[74] S. Ozawa, M. Ueda, N. Ando, O. Abe, and N. Shimizu, “High incidence of EGF receptor hyperproduction in esophageal squamous-cell carcinomas,” *International journal of cancer*, vol. 39, no. 3, pp. 333–337, 1987.

[75] ——, “Epidermal growth factor receptors in cancer tissues of esophagus, lung, pancreas, colorectum, breast and stomach,” *Cancer Science*, vol. 79, no. 11, pp. 1201–1207, 1988.

[76] B. Palcic, S. Lam, J. Hung, and C. MacAulay, “Detection and localization of early lung cancer by imaging techniques.” *CHEST Journal*, vol. 99, no. 3, pp. 742–743, 1991.

[77] M. Parker, “FPGAs for high-performance DSP applications,” 2005.

[78] ——, “FPGA vs. DSP design reliability and maintenance,” 2007.

[79] R. Philip, A. Penzkofer, W. Bäumler, R. Szeimies, and C. Abels, “Absorption and fluorescence spectroscopic investigation of indocyanine green,” *Journal of Photochemistry and Photobiology A: Chemistry*, vol. 96, no. 1, pp. 137–148, 1996.

[80] S. Prahl, “Optical absorption of hemoglobin,” *Oregon Medical Laser Center, http://omlc. ogi. edu/spectra/hemoglobin/index. html*, vol. 15, 1999.

[81] F. Rotermund, R. Weigand, W. Holzer, M. Wittmann, and A. Penzkofer, “Fluorescence spectroscopic analysis of indocyanine green j aggregates in water,” *Journal of Photochemistry and Photobiology A: Chemistry*, vol. 110, no. 1, pp. 75–78, 1997.

[82] F. Rotermund, R. Weigand, and A. Penzkofer, "J-aggregation and disaggregation of indocyanine green in water," *Chemical physics*, vol. 220, no. 3, pp. 385–392, 1997.

[83] E. M. Sevick-Muraca, J. P. Houston, and M. Gurfinkel, "Fluorescence-enhanced, near infrared diagnostic imaging with contrast agents," *Current opinion in chemical biology*, vol. 6, no. 5, pp. 642–650, 2002.

[84] W. J. Smith, *Modern Optical Engineering*. McGraw-Hill, 2000, ch. Image Formation, pp. 30–42.

[85] I. Stateikina, "Optoelectronic semiconductor devices - principals and characteristics," Master's thesis, Department of Electrical Engineering Concordia University, 2002.

[86] W. F. Sutterer, S. E. Hardin, R. W. Benson, L. Jerome Krovetz, and G. L. Schiebler, "Optical behavior of indocyanine green dye in blood and in aqueous solution," *American heart journal*, vol. 72, no. 3, pp. 345–350, 1966.

[87] P. Swain, "The future of wireless capsule endoscopy," *World journal of gastroenterology: WJG*, vol. 14, no. 26, p. 4142, 2008.

[88] M. Tadatsu, S. Ito, N. Muguruma, Y. Kusaka, K. Inayama, T. Bando, Y. Tadatsu, K. Okamoto, K. Ii, Y. Nagao *et al.*, "A new infrared fluorescent-labeling agent and labeled antibody for diagnosing microcancers," *Bioorganic & medicinal chemistry*, vol. 11, no. 15, pp. 3289–3294, 2003.

[89] Y. Tadatsu, N. Muguruma, S. Ito, M. Tadatsu, Y. Kusaka, K. Okamoto, Y. Imoto, H. Taue, S. Sano, and Y. Nagao, "Optimal labeling condition of antibodies available for immunofluorescence endoscopy," *J Med Invest*, vol. 53, no. 1-2, pp. 52–60, 2006.

[90] S. Takehana, M. Kaneko, and H. Mizuno, "Endoscopic diagnostic system using autofluorescence," *Diagnostic and therapeutic endoscopy*, vol. 5, no. 2, pp. 59–63, 1999.

[91] S. University, "Comparing FPGAs and DSPs for embedded signal processing," 2002.

[92] K. Urbanska, B. Romanowska-Dixon, Z. Matuszak, J. Oszajca, P. Nowak-Sliwinska, and G. Stochel, "Indocyanine green as a prospective sensitizer for photodynamic therapy of melanomas." *Acta Biochimica Polonica*, vol. 49, no. 2, pp. 387–391, 2001.

[93] B. Valeur and M. N. Berberan-Santos, "A brief history of fluorescence and phosphorescence before the emergence of quantum theory," *Journal of Chemical Education*, vol. 88, no. 6, pp. 731–738, 2011.

[94] ——, *Molecular fluorescence: principles and applications*. John Wiley & Sons, 2012.

[95] T. Vo-Dinh and B. Cullum, "Fluorescence spectroscopy for biomedical diagnostics," *Biomedical photonics handbook*, pp. 1–50, 2003.

[96] G. A. Wagnieres, W. M. Star, and B. C. Wilson, "In vivo fluorescence spectroscopy and imaging for oncological applications," *Photochemistry and photobiology*, vol. 68, no. 5, pp. 603–632, 1998.

[97] K. P. Withrow, J. P. Gleysteen, A. Safavy, J. Skipper, R. A. Desmond, K. Zinn, and E. L. Rosenthal, "Assessment of indocyanine green–labeled cetuximab to detect xenografted head and neck cancer cell lines," *Otolaryngology–Head and Neck Surgery*, vol. 137, no. 5, pp. 729–734, 2007.

[98] W. Yasui, H. Sumiyoshi, J. Hata, T. Kameda, A. Ochiai, H. Ito, and E. Tahara, "Expression of epidermal growth factor receptor in human gastric and colonic carcinomas," *Cancer research*, vol. 48, no. 1, pp. 137–141, 1988.

[99] B. Yuan, N. Chen, and Q. Zhu, "Emission and absorption properties of indocyanine green in intralipid solution," *Journal of biomedical optics*, vol. 9, no. 3, pp. 497–503, 2004.

[100] Y. Yuanlong, Y. Yanming, L. Fuming, L. Yufen, and M. Paozhong, "Characteristic autofluorescence for cancer diagnosis and its origin," *Lasers in surgery and medicine*, vol. 7, no. 6, pp. 528–532, 1987.

[101] B. Zeidman, "Introduction to CPLD and FPGA design," *The Chalkboard Network*, 2001.

[102] M. Zellweger, "Fluorescence spectroscopy of exogenous, exogenously-induced and endogenous fluorophores for the photodetection and photodynamic therapy of cancer." Ph.D. dissertation, Ecole Polytechnique Fédérale de Lausanne, 2000.

[103] H. Zeng, A. Weiss, R. Cline, and C. E. MacAulay, "Real-time endoscopic fluorescence imaging for early cancer detection in the gastrointestinal tract," *Bioimaging*, vol. 6, no. 4, pp. 151–165, 1998.

[104] H. Zhang, D. Morgan, G. Cecil, A. Burkholder, N. Ramocki, B. Scull, and P. K. Lund, "Biochromoendoscopy: molecular imaging with capsule endoscopy for detection of adenomas of the GI tract," *Gastrointestinal endoscopy*, vol. 68, no. 3, pp. 520–527, 2008.

[105] H. Zhang, R. R. Uselman, and D. Yee, "Exogenous near-infrared fluorophores and their applications in cancer diagnosis: biological and clinical perspectives," *Expert opinion on medical diagnostics*, vol. 5, no. 3, pp. 241–251, 2011.

[106] C. Zhao, Y. Liu, Y. Zhao, N. Fang, and T. J. Huang, "A reconfigurable plasmofluidic lens," *Nature communications*, vol. 4, 2013.

[107] J. F. Zhou, M. P. Chin, and S. A. Schafer, "Aggregation and degradation of indocyanine green," in *OE/LASE'94*. International Society for Optics and Photonics, 1994, pp. 495–505.

[108] W. Zijlstra and A. Buursma, "Spectrophotometry of hemoglobin: absorption spectra of bovine oxyhemoglobin, deoxyhemoglobin, carboxyhemoglobin, and methemoglobin," *Comparative Biochemistry and Physiology Part B: Biochemistry and Molecular Biology*, vol. 118, no. 4, pp. 743–749, 1997.

[109] Z. Zilic, G. Lemieux, K. Loveless, S. Brown, and Z. Vranesic, “Designing for high speed-performance in CPLDs and FPGAs,” in *The 3rd Canadian Workshop on Field-Programmable Devices (FPD’95)*, 1995, pp. 108–113.